Crossed Andreev reflection and electron transport in ferromagnetic hybrid structures

Saverio Russo

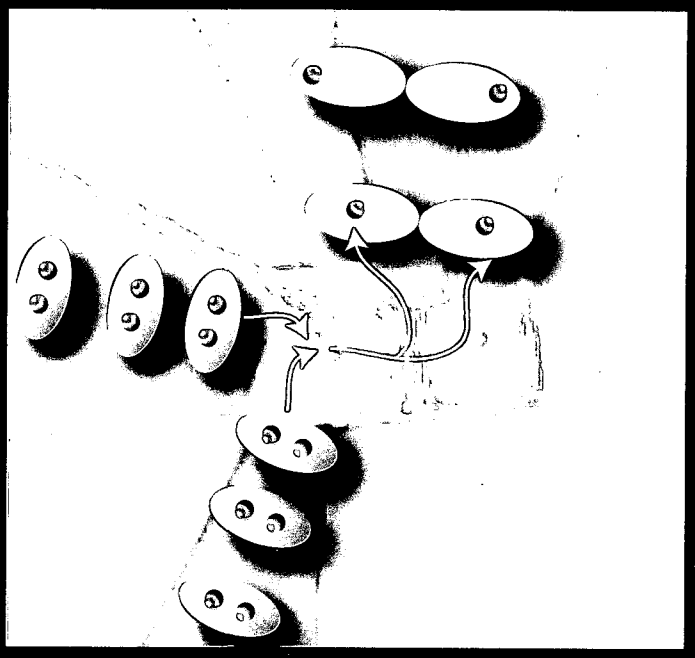

STELLINGEN

Behorende bij het proefschrift

Crossed Andreev reflection and electron transport in ferromagnetic hybrid structures

door Saverio Russo

1- Claims van de directe waarneming van gekruiste Andreev reflectie zijn alleen gerechtvaardigd als het juiste teken wordt waargenomen in de drie-terminal differentiële weerstand van supergeleider-gebaseerde hybride structuren. (Hoofdstuk 5)

2- De hoge contactweerstand aan het grensvlak tussen metaalelectroden en een organische halfgeleider is een ernstige hindernis voor toepassingen die gebaseerd zijn op organische veld-effect transistoren. (Hoofdstuk 7)

3- Het met de Josephson frequentie pompen van lading in een normale geleider die twee supergeleider/normal metal/supergeleider schakelingen verbindt, heeft twee voordelen: een grote gepompte stroom, en verwaarloosbare gelijkrichtende effecten. (Hoofdstuk 6)

4- De zwakke spin-baan koppeling en de afwezigheid van "hyperfine" interactie in grafeen maken dit materiaal uitstekend geschikt voor spin quantumbits.

5- Een creatieve geest gaat verder dan de strakke grenzen van wetenschappelijke gebieden, die ongelukkigerwijs nauwgezet bewaakt worden door minder creatieve bewoners.

6- Het ingewikkelde net van sterke familiegevoelens in Zuid-Italië vormt de rijkdom en de sterkte van de morele waarden in deze regio, terwijl het misbruik van deze gevoelens haar grootste zwakheid is.

7- Een seculiere maatschappij wordt gemakkelijk geplaagd door de ergste monotheïstische godsdienst: elk individu gelooft in zichzelf en alleen in zichzelf.

8- Goed klassiek onderwijs in de basisschool en het voortgezet onderwijs is een degelijk fundament voor een creatieve geest.

9- Het proces van het verkrijgen van kennis is niets anders dan een convolutie van de realiteit met de menselijke perceptie; de waarheid zelf blijft onbereikbaar en daardoor fascinerend.

10- Het menselijk leven is een gift en niemand heeft haar in eigendom. Daarom moet men leven in overeenstemming met de hoogten en diepten van het leven.

Deze stellingen worden verdedigbaar geacht en zijn als zodanig goedgekeurd door de promotores Prof. dr. ir. T. M. Klapwijk.

PROPOSITIONS

accompanying the Ph.D. Thesis

Crossed Andreev reflection and electron transport in ferromagnetic hybrid structures

by Saverio Russo

1- Claims of direct observation of crossed Andreev reflection are only justified if the proper sign is observed in the three terminal differential resistance of superconductor based hybrid structures. (Chapter 5)

2- The high contact resistance at the interface between metal electrodes and an organic semiconductor is a serious obstacle for applications based on organic field-effect transistors. (Chapter 7)

3- Charge pumping at the Josephson frequency in a normal conductor connecting two Superconductor/Normal metal/Superconductor junctions has two advantages: large pumped current and negligible rectification effects. (Chapter 6)

4- The weak spin-orbit coupling and the absence of hyperfine interaction in graphene make it an excellent material for spin qubits.

5- A creative mind goes beyond the rigid boundaries of scientific territories which are unfortunately carefully guarded by less creative occupants.

6- The intricate net of strong family feelings in Southern Italy constitutes the richness and the strength of the moral values of this region, while the misuse of these feelings is its major weakness.

7- A secular society is easily plagued by the worst monotheistic religion: each individual believes in himself and only in himself.

8- A good classical education in the primary and high schools is a solid foundation for a creative mind.

9- The process of acquiring knowledge is nothing else than a convolution of reality with the human perceptions; the truth in itself remains unreachable and for this reason fascinating.

10- Human life is a gift and no individual owns it. Hence one has to live up to life's highs and lows.

These propositions are considered opposable and defendable and as such have been approved by the supervisor Prof. dr. ir. T. M. Klapwijk.

Crossed Andreev reflection and electron transport in ferromagnetic hybrid structures

Crossed Andreev reflection and electron transport in ferromagnetic hybrid structures

Proefschrift

ter verkrijging van de graad van doctor
aan de Technische Universiteit Delft,
op gezag van de Rector Magnificus Prof. dr. ir. J. T. Fokkema,
voorzitter van het College voor Promoties,
in het openbaar te verdedigen op maandag 25 juni 2007 om 10.00 uur

door

Saverio Russo

Master of Science in Physics,
Universitá di Pisa, Pisa, Italy
geboren te Canosa di Puglia, Italië.

Dit proefschrift is goedgekeurd door de promotor:
Prof. Dr. Ir. T. M. Klapwijk

Toegevoegd promotor:
Dr. A. F. Morpurgo

Samenstelling promotiecommissie:

Rector Magnificus	voorzitter
Prof. Dr. Ir. T. M. Klapwijk	Technische Universiteit Delft, promotor
Dr. A. F. Morpurgo	Technische Universiteit Delft, toegevoegd promotor
Prof. Dr. Prof. Dr. P.W. Brouwer	Cornell University, New York
Prof. Dr. B. Koopmans	Eindhoven University of Technology, Eindhoven
Prof. Dr. Ir. B.J. van Wees	University of Groningen, Groningen
Prof. Dr. Y.V. Nazarov	Technische Universiteit Delft, Delft
Dr. Ir. W.G. van der Wiel	University of Twente, Twente
Prof. Dr. Ir. H.S.J. van der Zant	Technische Universiteit Delft, Delft, reservelid

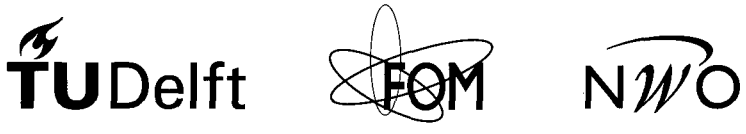

Cover design: S. Russo
Front: Schematic representation of Cooper pair splitting in the superconductor based hybrid structure studied in this Thesis.

Printed by: Ponsen & Looijen, Wageningen, The Netherlands

Casimir PhD Series, Delft-Leiden 2007

ISBN: 978-90-8593-030-3

Contents

Chapter 1

Introduction

1.1 Spintronics

In a Chinese book, dated from the 4th century BC, called Book of the Devil Valley Master we read: "The lodestone makes iron come or it attracts it" [1]. This is the earliest reference to magnetism. It took eight centuries to discover, also in ancient China, that this lodestone could be used for a compass useful for navigation. Another force at a distance which fascinated early humanity is static electricity obtained from rubbing amber against fur. The name itself, electricity, comes from the Greek $\eta\lambda\varepsilon\kappa\tau\rho o\nu$ which means amber. The further evolution of these phenomena has led to an enormous development of use in electrical motors, lighting, communication and in particular information processing. Nearly all information processing is done using electron current flow and magnetism. Our computers or MP3-players have thousands of small devices in which charge flows carrying information or storing information also controlled by magnetic components.

Current research in electronics tries predominantly to identify new ways to process, transmit, and store information by taking advantage of the quantum wave nature of carriers, their charge and magnetic moment. This new branch of modern electronics is known as *spintronics* [2, 3]. Conventional electronics is based on the number of charges and their energies, and device performance is limited in speed due to energy dissipation, whereas spintronics is based on the direction of spin and spin coupling, and is capable of higher speeds at low power consumption. Computer's hard drives are probably one of the best examples of conventional magneto-electronic devices which are exploiting magnetic ordering and thus the spin of the conduction particles for storing information [4]. In a hard drive the binary bit of information '0' or '1' is associated to the direction of the uniform magnetic ordering of small regions. Since ferromagnetic materials exhibit a spontaneous ordering of the magnetization pointing in a preferential directions which can be engineered [4, 5], these materials are certainly a natural choice for implementing magnetic memories. In this new class of magneto-electronic devices the magnetic moments are used, rather than an electric charge, to determine the on/off state of the memory bit cell.

The greatest impact of spintronic devices in consumer electronics is expected to come with magnetic random access memories (MRAM [4]). These new generation memories are based on the dependence of the electrical resistance of the cell on the relative alignment of the magnetization of two ferromagnetic plates (F) separate by a thin insulator (I). Respectively, a low resistance state is achieved for parallel magnetization and an high resistance state for antiparallel configuration to which a binary bit '1' and '0' can be associated. The working principle

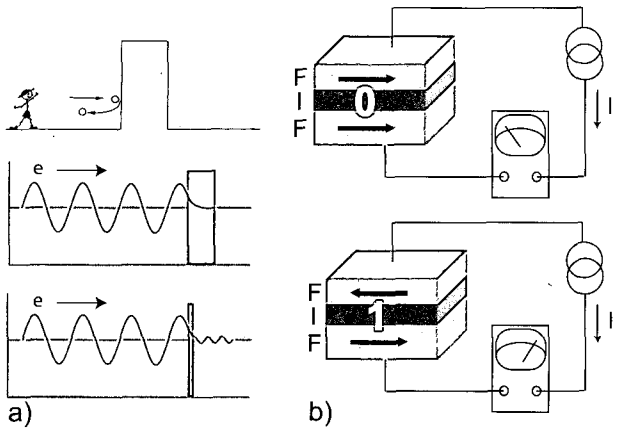

Figure 1.1: a) Top panel: classically particles with low energy required to get over the barrier are reflected on the barrier. Figure from Ref. [6]. Middle and bottom panel: in quantum mechanics we account for the wave behavior of the particles. The wavefunction of the electron does not decay abruptly to zero but decays exponentially. If the barrier is thin enough there is a probability that the electron may be found on the other side of the barrier. This allows the electron to move (or tunnel) through the barrier. b) Scheme illustrating the working principle of an MRAM. Low resistance (binary bit 0) is measured for parallel orientation of the magnetization and high resistance (binary bit 1) for antiparallel orientation.

governing the functionalities of MRAMs is based on the wave nature and spin of the charge carriers. The electron transport through the FIF hybrid structure is regulated by the quantum mechanical concept of electron tunneling through the very thin insulator layer [7]. Classical mechanics predicts no current for an impinging electron with energy much smaller than the barrier height, indeed when playing tennis against a wall the ball is always reflected back by the wall. However, quantum mechanics gives the counter intuitive answer that this electron has a finite probability to tunnel through the oxide barrier (see Fig. 1.1a). In the case of MRAM the electrons are tunneling from one ferromagnetic plate to the other, and they carry the information on the direction of the magnetization of the ferromagnet in their spin direction. In a ferromagnet, transport of electrons with opposite spin direction to the one allowed is depressed [5], hence high resistance state is achieved in the MRAM for antiparallel magnetization configuration. Consequently, a low resistance state characterizes the parallel magnetization configuration [4] (see Fig. 1.1b).
As for tunneling many transport processes rely on the quantum mechanical na-

ture of the hybrid devices and it is a central task for this thesis to pinpoint the mechanisms of injection at interfaces with different materials (heterointerfaces).

1.2 Superconductor based heterointerfaces

When a superconductor (S) is in electrical contact with a normal metal (N), a heterointerface is formed between the two material systems. In the vicinity of this boundary, the properties of each material are not any more the properties of the bulk. Using a pictorial language, we can say that the superconducting properties "leak" into N (proximity effect [8]) and it is also true that the normal metal properties "leak" into S (inverse proximity effect [8]). An example is offered by the density of states in the vicinity of the boundary which is different from the density of states of both bulk materials [9]. The understanding of these proximity effects is strictly related to transport mechanisms in the superconductor itself, in the specific material N in contact with S and most of all to the transport processes through the interface.
Supercurrent in a BCS superconductor is carried by paired electrons (Cooper pairs [10]). In a Cooper pair the magnetic moments of the individual electrons are in a correlated state such that the total spin is 0, a singlet state. The spin part of the wave function for these electrons cannot be written as a product of single-particle wave functions, thus reads:

$$\phi^{\text{spin}}_{\sigma_1,\sigma_2} = \frac{1}{\sqrt{2}}(|\uparrow\downarrow> - |\downarrow\uparrow>). \tag{1.1}$$

These two electrons in the Cooper pair are then said to be mutually spin entangled. The entangled form of the wave function in Eq. 1.1 implies that if a measurement of the component $\overrightarrow{\sigma}_1 \cdot \overrightarrow{a}$, with any $\overrightarrow{a}$ unit vector, yields the value +1 then, according to quantum mechanics, measurements of $\overrightarrow{\sigma}_2 \cdot \overrightarrow{a}$ must yield the value -1 and *vice versa* [11]. As a result, suppose that we can separate spatially the two electrons, measurements performed on one of the particles seem to be instantaneously influencing the other particle entangled with it, no matter how far away it is: the "spooky action at a distance" [12], as Albert Einstein called it. It has been predicted that, if it would be possible to inject electrons in the state described by Eq. 1.1 into the two arm of a mesoscopic ring, this would result in specific current fluctuations which cannot be mimicked by any classical counterpart [13]. Such an experiment has not yet been successfully performed, however with status of the art technology might be soon within reach and it would allow for testing in solid state devices quantum correlations [14].

Many theoretical proposals have been stimulated by the spin-entangled nature of electrons in a Cooper pair. Different ways to split these entangled electrons by injection into an external nanocircuit -i.e. solid state entangler device- have been put forward [15-24]. However, as we will discuss in Section 2.5, the understanding of quantum mechanical transport at multiple superconductor based heterointerfaces is necessary for a realistic success of a superconductor entangler. Further functionalities to superconductor based heterointerfaces can be added when replacing a normal metal with a ferromagnetic material. The injection mechanism into a ferromagnet, as we already discussed in the context of MRAM, strongly depends on the relative orientation of the spin direction of the injecting particle and the allowed direction of spin in the ferromagnet. Thus a ferromagnet acts as a spin filter, as it allows electron transport with the "right" spin direction and reduces transport of particles with the "wrong" spin direction. Such a capability can be engineered in a superconductor based entangler to detect and/or control the spin direction of the split electrons from a Cooper pair. The success of these ventures depends on a deeper understanding of fundamental spin interactions in solid state materials as well as the roles of dimensionality, defects, and semiconductor band structure in modifying these dynamics.

1.3 Ferromagnetic semiconductors heterointerfaces

Large part of modern electronics uses the functionalities of charge modulation by an electrostatic gate or doping of semiconducting materials, in parallel with the spin-filter capability of ferromagnetic materials. The possibility to combine ferromagnetic and semiconducting properties in one material system was achieved with doping semiconducting materials with magnetic impurities [25-30]. Ferromagnetic semiconductors or diluted magnetic semiconductors (DMS) have unique material properties [31-38]. Respectively, since DMS are semiconductors, they are extraordinary sensitive to impurity atoms, defects, and charges on external gates. At the same time DMS are ferromagnets, thus they display an ordered magnetic state below a transition temperature. That is why DMS are a suitable candidate for information processing, as semiconductors, and for information storage and retrieval, as ferromagnet[34, 35]. Furthermore, the coexistence of magnetism and semiconducting properties offers the possibility to access new physical phenomena in transport experiments, and already come close to realizing the suite of tunable magnetic, transport and optical properties that is imagined in many spin

electronic device concepts.
One advantage represented by ferromagnetic semiconductors is the highly efficient spin injection through DMS-semiconductors heterointerfaces [39]. Schmidt *et al.* [40] demonstrated that the efficiency of spin injection depends on the ratio of the spin dependent conductivities of the ferromagnetic and non ferromagnetic electrode. In particular when the conductivity of the ferromagnet is larger then the conductivity of the non ferromagnetic electrode, which is the case for FM-semiconductor, only poor spin injection efficiency is possible[40]. A possible solution to the problem of the conductance mismatch is offered by tunnel barriers at the injecting interfaces between a metallic ferromagnet and the semiconducting channel [41-45]. However, an alternative solution to this mismatch of conductance problem is offered by the use of DMS as ferromagnetic injectors, in which case a simple ohmic contact between the non-ferromagnetic and the ferromagnetic should result in high spin injection [39].
The semiconducting nature of DMS allows for field effect experiments, which pointed out the relation between charge density and ferromagnetic properties, demonstrating the electrically tunable ferromagnetism at temperatures higher then liquid helium temperature [37]. Another concrete advantage offered by some DMS like GaMnAs is the high degree of spin polarization of the charge carriers[46], which makes magnetoresistive effects in GaMnAs much larger than in metallic ferromagnets [35]. However, at the present stage the highest Curie temperature archived in a GaMnAs film is still well below room temperature $\sim 170K$. Despite the effort invested by scientists to find a way to increase the ferromagnetic transition temperature, we cannot be certain that these III-V magnetic semiconductors will ever reach the high transition temperatures required for widespread applications.

1.4 Organic semiconductor based hybrid structures

Organic semiconductors are of great interest for electronics applications, as they have many advantages over their inorganic counterparts. Organic devices can be casted on bendable substrates, such as plastic substrates, and fabricated with the most conventional means such as screen and inkjet printing. Organic molecular materials, crystals or films of organic molecules held together by weak Van der Waals intermolecular interactions, do represent an interesting material system for modern electronics. Rollable displays, labels on consumer products display-

ing information on the product and yet more gadgets which now seem to belong to science fiction may very soon be part of our lives.

A typical way to measure the transport properties of organic single crystal is to use a transistor configuration [47]. This consists of two metal contacts which act as source-drain and an electrostatic gate for the modulation of the charge density in the organic semiconductors. The active channel is formed at the organic-insulator interface, thus the current between the source and drain is modulated by the gate. From the analysis of the characteristic curves of the transistor it is possible to extract information on the kind of charge carriers, mobility or also contact resistance which contains information on the heterointerface organic-normal metal[49, 50]. In particular, the high charge-carrier mobility demonstrated in rubrene single crystals showed that when down scaled, molecular electronic devices are limited by contact resistance [49]. The nature itself of organic-metal interface is currently being investigated and not yet understood. The simple Schottky barrier model [47, 51] where the different work functions of the materials at the interface generate a potential barrier might be an oversimplified model. Other more sophisticated models have been developed but yet the nature of the interface organic-metal remains an unsolved problem[50].

One attractive -and yet unexpected- feature of organic materials concerns the promise for a long spin coherence time, which makes organic materials a suitable candidate for spin electronic devices [52-55]. Scattering on magnetic impurities is certainly one of the main causes for a short spin lifetime, however in a pure semiconductor the major role for spin decoherence is spin-orbit interaction. An electron travelling in a crystal with velocity v and subject to an external electric field will see a magnetic field $B = (v/c) \times E$. Seemingly an electron in an atomic orbital feels the electric field of the nucleus. In the rest frame of the electron, the nucleus orbits around the electron which consequently feels a magnetic field. This spin-orbit coupling is larger for atoms with large Z, suggesting that materials with light atoms, like organic materials, have less spin-orbit interaction. Consequently, this intrinsic cause of spin decoherence is dramatically reduced in organic materials. Another cause of spin decoherence comes from hyperfine interaction, this originates from a direct magnetic coupling of the electron and the nucleus magnetic moment. However, in the case of π-conjugated organic materials the electrons are delocalized on π orbitals which reside in planes up and down with respect to the plane of the nucleus. Thus hyperfine interaction possibly does not play a role at least for the class of π-conjugated organic materials, which is the one of interest for this work of Thesis [48]. For these reasons, organic semiconductors and in particular single-crystals[49] which are defect free, hold the promise for an extremely long spin decoherence time possibly in excess to a few

milliseconds [52-55], which is much longer than for normal metals.

1.5 This thesis

In this Thesis, we report on the realization of different kinds of heterointerfaces involving ferromagnetic, superconducting and organic single crystals and we present the analysis of the transport phenomenon.

Chapter 2: *via* this Chapter the reader is introduced to the most relevant and fundamental theoretical concepts necessary to understand the transport mechanisms through the heterointerfaces studied in the forthcoming chapters. We will first present the ferromagnetic semiconductor GaMnAs and discuss the charge mediated ferromagnetism in this material. Then we will consider transport processes at superconductor based heterointerfaces, with particular emphasis on transport through multiple interfaces. Thus we proceed to investigate the use of hybrid ferromagnetic semiconductor-insulator-superconductor to address a modification in the density of states of GaMnAs due to electron-electron interaction. Further we introduce the fundamental concepts related to a different transport mechanism such as adiabatic charge pumping -*i.e.* a dc current flows in response to a cyclic modulation of some system's parameters without any dc bias applied on the device. We conclude this chapter with a discussion on organic single crystal hybrid structures.

Chapter 3: the understanding of transport and magnetic properties of GaMnAs is a necessary step for defining the relevance of this magnetic semiconductor for spin electronic devices. In this Chapter a systematic investigation of the longitudinal and transverse magnetoresistance of a single ferromagnetic domain in GaMnAs is presented. We show that a fully quantitative description of the experimental data can be obtained with a single domain model when taking into account the intrinsic dependence of the resistivity on the magnetic induction.

Chapter 4: a tunnel barrier at the interface between GaMnAs and superconducting NbTiN is a powerful tool to explore the density of states of GaMnAs and gain insight in the intrinsic physical properties of this ferromagnetic semiconductor. The tunnel differential conductance at low temperature displays a $\sqrt{V}$ dependence, consistent with the opening of a correlation gap in the density of states of GaMnAs. We show that low temperature annealing, by removing the interstitial Mn defects, acts on the electron-electron interaction thus it modifies the correlation gap.

Chapter 5: in this Chapter we present a clear evidence for the occurrence

of non-local Andreev reflection (process equivalent to Cooper pair splitting) and elastic cotunneling through superconducting layers of thickness comparable to the superconducting coherence length. We find that the probability of the two processes is energy dependent, with elastic cotunneling dominating at low energy and non-local Andreev reflection at higher energies. The energy scale of the crossover is found to be the Thouless energy of the superconductor, which indicates the phase coherence of the processes.

Chapter 6: in this chapter we study theoretically adiabatic quantum pumping in a normal metal conductor coupling the normal regions of two SNS Josephson junctions. The pumping parameters are the phases of the superconducting order parameter in the different superconducting contacts. Within a ballistic model and using scattering matrix approach, we demonstrate that a non zero pumped charge can flow through the device. Since the proposed adiabatic pump exploits the evolution of the superconducting phases due to the ac Josephson effect, this system can be operated at very high frequency resulting in a pumped current as large as a nanoAmperes per channel of conduction. Finally, we discuss the experimental relevance of our calculations.

Chapter 7: we present a systematic study of the contact resistance of rubrene single-crystal field-effect transistors (FETs) with Nickel electrodes by performing scaling experiments on devices with channel length ranging from 200 nm up to 300 μm. We find that the contact resistance can be as low as 100 Ωcm with narrowly spread fluctuations. These results indicate that nickel is a very promising electrode material for the reproducible fabrication of low resistance contacts in organic FETs.

Bibliography

[1] Li Shu-hua, Origine de la Boussole 11. Aimant et Boussole, Isis, Vol. 45, No. 2. (Jul. 1954), p.175.

[2] S.A. Wolf *et al.*, Science **294**, 1488 (2001).

[3] I. Žutić, J. Fabian and S. Das Sarma, Rev. Mod. Phys. **76**, 323 (2004).

[4] Magnetoelectronics, edited by M. Johnson. Amsterdam: Elsevier (2004).

[5] The allowed spin direction for electrons in a ferromagnet can be parallel or antiparallel to the local magnetization depending on the material system. See R. C. O'Handley, Modern Magnetic Materials principles and Applications, New York: John Wiley & Sons (2000).

[6] I. Giaever, Phys. Rev. Lett. **5**, 147 (1960);464 (1960).

[7] E. L. Wolf, Principles of electron tunneling spectroscopy, New York : Oxford University Press, 1985.

[8] P. G. de Gennes, Superconductivity of metals and alloys, Addison-Wesley, 1966.

[9] S. Guéron *et al.*, Phys. Rev. Lett. **77**, 3025 (1996).

[10] L. N. Cooper, Phys. Rev. **104**, 1189 (1956).

[11] J.S. Bell,Speakable and Unspeakable in Quantum Mechanics, Cambridge Press University (2004).

[12] This quantum correlation, which has no classical counterpart, can be proved experimentally with the violation of Bell inequality. See Ref. [11].

[13] G. Burkard, D. Loss and E.V. Sukhorukov, Phys. Rev. B **61**, R16303 (2000).

[14] M. A. Nielsen and I. L. Chang, Quantum computation and quantum information, Cambridge: Cambridge University Press (2000).

[15] G. Deutscher and D. Feinberg, Appl. Phys. Lett. **76**, 487 (2000).

[16] G. Falci, D. Feinberg and F. W. J. Hekking, Europhys. Lett. **54**, (2) 255 (2001).

[17] P. Recher, E. V. Sukhorukov and D. Loss, Phys. Rev. B **63**, 165314 (2001).

[18] N. M. Chtchelkatchev *et al.*, Phys. Rev. B **66**, 161320 (2002).

[19] C. Bena *et al.*, Phys. Rev. Lett. **89**, 037901 (2002).

[20] P. Samuelsson, E. V. Sukhorukov and M. Buttiker, Phys. Rev. Lett. **91**, 157002 (2003).

[21] P. Recher and D. Loss, Phys. Rev. Lett. **91**, 267003 (2003).

[22] E. Prada and F. Sols, Eur. Phys. J. B **40**, 379 (2004).

[23] G. Bignon *et al.*, Europhys. Lett. **67**, 110 (2004).

[24] F. Giazotto *et al.*, Phys. Rev. Lett. **97**, 087001 (2006).

[25] J. K. Furdyna and J. Kossut, Semiconductor and semimetals, Vol. 25. New York: Academic (1988).

[26] T. Dietl, (Diluted) Magnetic Semiconductors, in Handbook of Semiconductors, (ed. S. Mahajan) Vol. 3B. Amsterdam: North Hallnd (1994).

[27] T. Story *et al.*, Phys. Rev. Lett. **56**, 777 (1986).

[28] H. Ohno, Science **281**, 951 (1998).

[29] H. Ohno, J. Mag. Mag. Materials **200**, 110 (1999).

[30] H. Ohno, F. Matsukura and Y. Ohno, Solid State Commun. **117**, 179 (2001).

[31] H. Ohno *et al.*, Appl. Phys. Lett. **69**, 363 (1996).

[32] H. Munekata *et al.*, Phys. Rev. Lett. **63**, 1849 (1989).

[33] A. H. MacDonald, P. Schiffer and N. Samarth, Nature materials **4**, 195 (2005).

[34] Semiconductor Spintronics and Quantum Computation, Eds. D. D. Awschalom, D. Loss and N. Samarth. Berlin: Springer-Verlag (2002).

[35] T. Jungwirth *et al.*, Rev. Mod. Phys. **78**, 809 (2006).

[36] M. Yamanouchi *et al.*, Nature **428**, 539 (2004).

[37] H. Ohno *et al.*, Nature **408**, 944 (2000).

[38] Y. Ohno *et al.*, Nature **402**, 790 (1999).

[39] A. Khaetskii *et al.*, Phys. Rev. B **71**, 235327 (2005).

[40] G. Schmidt *et al.*, Phys. Rev. B **62**, R4790 (2000).

[41] H. C. Koo *et al.*, Appl. Phys. Lett. **90**, 022101 (2007).

[42] S. F. Alvarado and Ph. Renaud, Phys. Rev. Lett. **68**, 1387 (1992).

[43] V. LaBella *et al.*, Science **292**, 1518 (2001).

[44] E. I. Rashba, Phys. Rev. B **62**, R16267 (2000).

[45] L. C. Chen *et al.*, J. Vac. Sci. Tech. B **18**, 2057 (2000).

[46] J. G. Braden *et al.*, Phys. Rev. Lett. **91**, 056602 (2003).

[47] S. M. Sze, Physics of semiconductor devices. New York: Wiley (1981).

[48] Recent experiments have reported the observation of organic magnetoresistance (OMAR) effect in thin films of π-conjugated organic materials. Though at the moment there is no consensus on the origin of OMAR effect, a possible role of hyperfine interaction is currently been discussed. See Y. Sheng, T.D. Nguyen, G. Veeraraghavan *et al.*, Phys Rev. B **75**, 035202 (2007).

[49] M. E. Gershenson, V. Podzorov, and A. F. Morpurgo, Rev. Mod. Phys. **78**, 973 (2006).

[50] Organic Electronics: Materials, Manufacturing and Applications , Ed. H. Klauk. New York: John Wiley & Sons (2006).

[51] M. Abkowitz, J. S. Facci and J. Rehm, J. Appl. Phys. **83**, 2670 (1998).

[52] V. I. Krinichnyi, Synth. Met. **108**, 173 (2000).

[53] Z. H. Xiong *et al.*, Nature **427**, 821 (2004).

[54] V. Dediu *et al.*, Solid State Commun. **122**, 181 (2002).

[55] S. Pramanik *et al.*, Nature Nanotechnology, Published online: 18 March 2007.

Chapter 2

Theoretical concepts

2.1 Basics of ferromagnetism

Ferromagnetic materials show a long-range order of their atomic magnetic moments, even in the absence of an external magnetic field. We can define this order by the magnetization **M** as the magnetic moment per unit volume. This spontaneous, long range magnetization of a ferromagnet is observed to vanish above an ordering temperature called the Curie temperature (see inset in Fig. 2.1). The microscopic mechanisms responsible for this many body effect in a magnetic sample are several and of different nature, but the main spirit of the ferromagnetic transition can be grasped by a phenomenological theory such as the second order phase transitions theory developed by Landau [1].
Let's assume that all spins "feel" an identical average exchange field produced by all their neighbors, this is a mean field approximation. In the ferromagnetic transition the magnetization is the order parameter, $M = 0$ for $T > T_C$ and the system is in the paramagnetic phase. While for $T < T_C$ there is a non zero M, which characterizes the ferromagnetic phase. The continuity in the variation of the state in a second order phase transition can be expressed mathematically as the fact that near the transition point the order parameter assumes infinitesimally small values. This is why we can develop the free energy F in series of the order parameter:

$$F(M) = F_0 + a(T)M^2 + bM^4. \tag{2.1}$$

Because there is no energetic difference between up or down direction of the magnetization, this series cannot contain any odd power of M. We assume F_0 and b constants, with $b > 0$ and $a(T)$ temperature dependent. A correct description of the phase transition is obtained when assuming $a(T) = a_0(T - T_C)$. The ground state of the system is found by minimizing the free energy $\partial F/\partial M = 0$, which implies:

$$2M[a_0(T - T_C) + 2bM^2] = 0, \tag{2.2}$$

thus either M=0 ($T > T_C$ and the system is in the paramagnetic state) or $M = \pm\sqrt{[\frac{a_0(T-T_C)}{2b}]}$, only valid when $T < T_C$ and the system is in the ferromagnetic state.
At a microscopic level the single particle density of states (DOS) in a ferromagnet is distinguished in a *majority* spin band, the spin-down, and *minority* spin band, for the spin-up (see Fig. 2.3b). In the Stoner model [1], the major-

ity and minority spin bands are taken equal but shifted in energy. This shift in energy is known as the exchange energy. The difference in number of spin-down electrons from the number of spin-up electrons at the Fermi energy (E_F) is at the origin of the ferromagnetism in the material $N\uparrow(E_F) \neq N\downarrow(E_F)$. It is useful to define a quantity known as spin polarization, P, which is directly proportional to the asymmetry of the density of states at the Fermi level: $P = (N\uparrow(E_F) - N\downarrow(E_F))/(N\uparrow(E_F) + N\downarrow(E_F))$. This quantity assumes values between -1 and 1, 0 when the material does not have any spin polarization ($N\uparrow(E_F) = N\downarrow(E_F)$) and ± 1 when all the electrons are spin polarized.
The magnetization in a ferromagnet has a "preference" to lie in a particular direction, this property is called magnetic anisotropy. A description of this phenomenon can be given by a simple mean field approach considering the free energy of the ferromagnet. In a crystal an easy axis and a hard axis of magnetization are identified, respectively the easy axis as minima of the free energy while the hard axis as maxima of the free energy. Magnetic anisotropy has its origin in sample shape, crystal symmetry, stress and directed atomic pair ordering [1]. For this Thesis, we would like to mention briefly the physical origin of sample shape anisotropy. Dipole interactions arising from free magnetic moments at surfaces are responsible for shape anisotropy, and this can be represented in terms of fields external to the sample. The ability to manipulate the easy-axis orientation -i.e. by shape anisotropy- has many implications in spintronics devices.

2.2 III-V ferromagnetic semiconductors

2.2.1 Introduction to ferromagnetic semiconductors

For long time, it remained an open problem the possibility to combine the semiconducting properties and the magnetic properties together in a new functional material system. These ferromagnetic semiconductors would allow for a control of ferromagnetic properties by means of an electric gate. Starting from europium chalcogenides[2] many functional ferromagnets have been investigated. Given the richness in optical and electronic devices realized with III-V based semiconductor heterostructure, it was natural the question if also a III-V semiconductor can be made ferromagnetic. If so, this would open a path towards physics and application of previously not available combinations of quantum structures.

Making a non magnetic III-V semiconductor magnetic by doping with magnetic impurities has proven to be a difficult task. This is because of the low solubility limit of the magnetic impurities in the host III-V's [3, 4, 5]. A typical magnetic impurity is Mn, with magnetic moment S=5/2. Even if non-equilibrium

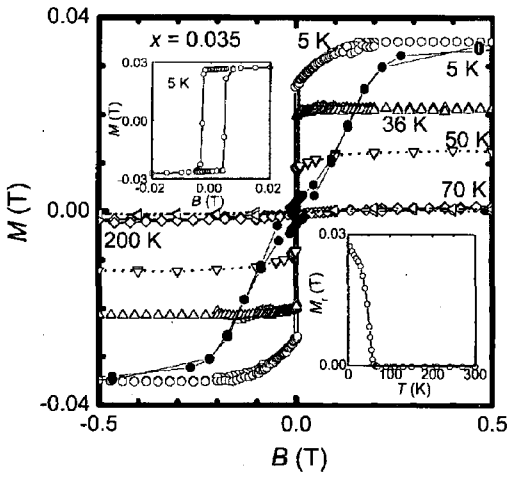

Figure 2.1: SQUID measurements of remanent magnetization vs. field for a 150nm thick GaMnAs film (Mn concentration x=0.035). All open symbols are taken with the field in plane and closed symbol with field perpendicular to the plane. The upper left inset shows a magnified view of the data at 5K with in plane field. The lower right inset shows the temperature dependence of the remanent magnetization, indicating that the transition temperature is 60K. Figure from Ref. [3]

Molecular Beam Epitaxial (MBE) growth allowed for doping in excess to the thermodynamic solubility limit, the segregation of impurities often turned out to be a major problem. For instance, a too large substrate temperature or Mn flux during growth result in a different, unwanted material (MnAs). A solution to these problems has come from the Low Temperature MBE (LT-MBE) growth. This technique, successfully demonstrated by Munekata et al. [6], has led to the first synthesis of a uniform alloy (In,Mn)As film on GaAs substrate, soon followed by the discovery of ferromagnetism in (Ga,Mn)As[8] with a relatively low transition temperature ($T_C \sim 60$K, the highest T_C so far obtained is ~ 173 K [7]). In Fig. 2.1 we show SQUID measurements of the spontaneous magnetization for a 150nm thick GaMnAs film (Mn composition x=0.035) *versus* external magnetic field (main graph) and temperature (bottom inset), at the Curie temperature the magnetization goes to zero.

However, the LT-MBE growth most probably introduces a high concentration of defects in the material structure. Thus the III-V ferromagnetic films contain considerable disorder, which causes the material to be close to a metal insulator transition (MIT) [3, 8]. It is experimentally established that GaMnAs samples

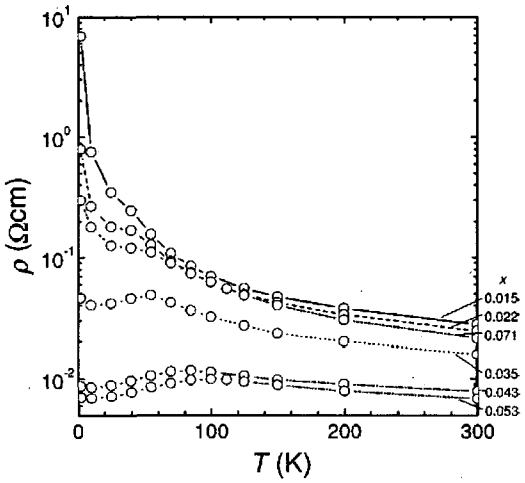

Figure 2.2: Temperature dependence of the sheet resistance of six 200nm thick GaMnAs films. The Mn concentration of the samples varies from x=0.035 to 0.053. Samples with intermediate composition (0.035-0.053) are metallic. Figure from Ref.[5]

with a Mn concentration $x < 0.03$ and $x > 0.06$ are on the insulating side of the MIT. In this case the sheet resistance increases upon cooling the film to temperatures $T < T_C$ (see Fig.2.2). Samples with Mn concentration $0.03 < x < 0.06$ are on the metal side, and the sheet resistance decreases with cooling to temperatures $T < T_C$ (see Fig.2.2). All the ρ versus temperature curves at the Curie temperature show a maximum, this is obscured by the rapid increase in resistance for the insulating samples. This behavior of ρ-T is typical of magnetic materials, and it is due to scattering of carriers by magnetic spin fluctuation via exchange interaction [9].

2.2.2 Origin of ferromagnetism in GaMnAs

GaAs is one of the most studied semiconductors. Its crystalline structure is zincblende, which consists of two interpenetrating fcc lattices. The two sublattices are occupied by the two different types of atoms. When doping with Mn atoms, it was demonstrated that the Mn is substitutionally incorporated into the Ga sublattice[10] (see Fig. 2.3a). Due to its valency, the Mn acts as an acceptor, leaving a hole in the valence band, but it also provides a large magnetic moment (S=5/2). However, Hall measurements[4] show that the hole concentration p in GaMnAs is somewhat smaller than the nominal Mn doping concentration, in

the alloy. Consistently, SQUID magnetometry measurements demonstrated that also the measured saturation magnetization M_S is smaller than expected from the nominal Mn doping level [4]. The measured value of M_S is consistent with the hole concentration p of the GaMnAs samples. These results pose the question of the relation between the hole density p and Mn concentration in connection with the origin of ferromagnetism in GaMnAs.

To separate the influence of carrier density from the density of Mn magnetic

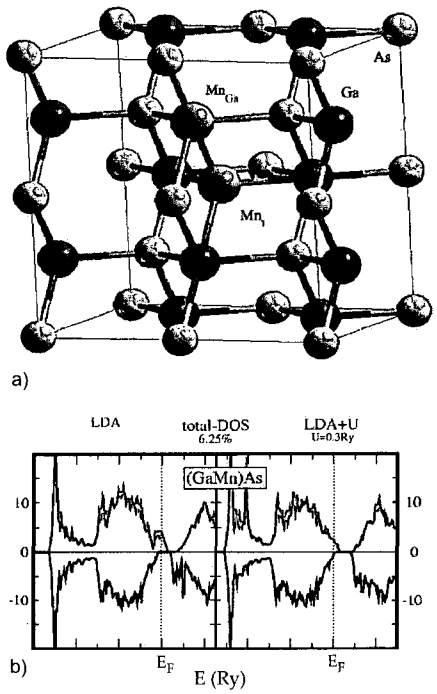

Figure 2.3: a) Scheme of the zincblende structure of GaMnAs showing substitutional Mn_{Ga} and interstitial Mn_I in GaAs. b) Graphs of the spin-resolved total DOS of GaMnAs for a Mn concentration of 6.25% calculated with two different techniques: left graph with LDA and right graph with LDA+U. The spin-up (spin-down) DOS is shown above (below) the abscissa axis. The total DOS is given per chemical unit cell of the semiconductor. Figure from Ref. [11]

moments, it is convenient to dope with Sn non-magnetic dopants. The incorporation of Sn, which acts as a donor in GaMnAs, compensating the free hole density, results in a decrease of the Curie temperature [12]. In semi-insulating carrier-compensated (Ga,Mn)As, the direct magnetic interaction between Mn dopants

was identified as being antiferromagnetic [12, 13]. These experimental findings clearly pointed out that the charge carriers have a primary role in inducing the ferromagnetism in GaMnAs. In particular the charge carriers could be responsible in mediating the interaction between Mn localized magnetic moments leading to magnetic ordering in the material.

A further prove of the role of the carriers in mediating ferromagnetism came from the field-effect. Thanks to the semiconducting nature of GaMnAs, another way to change the carrier concentration, beside the chemical doping with Sn, is the electrostatic doping by means of electrostatic gate. A first successful experiment was carried out on InMnAs [14]. It was found that a depletion of the hole concentration results in a reduction of the Curie temperature as well as in a reduction of the spontaneous magnetization. A similar experiment with similar results was later performed on GaMnAs [15]. Such electrostatically induced changes can be done reversibly and maintain thermodynamic equilibrium.

The experimental finding of an apparent large magnetization and hole density deficit in GaMnAs is, at least in large part, connected to a particular kind of defect in the lattice structure of the material. Channeling Rutherford backscattering and particle induced x-ray emission measurements demonstrated that Mn atoms can also occupy interstitial positions (Mn_I) in the GaMnAs lattice [4] (see Fig 2.3a). Mn_I acts as a double donor [4]. Each interstitial Mn therefore compensates two substitutional Mn acceptors, reducing the hole density with consequent degradation of the ferromagnetic properties. Experimentally it was found that this defect has a characteristic low energy barrier such that their density can be drastically reduced upon postgrowth annealing at temperatures close to the growth temperature, improving the magnetic properties of GaMnAs [4]. Another defect, which acts also as a double donor, is As-antisites[4]. However, in contrast to Mn_I, As-antisites are stable up to temperatures well above the growth temperature of GaMnAs, therefore they cannot be removed by a low temperature annealing.

The microscopic origin of this carrier mediated ferromagnetism was soon traced back to RKKY interaction[8]. The magnetic moment of the impurity weakly polarizes the holes in the valence band which then communicate the spin information to another impurity site. The electron gas effectively forms a Fourier series of oscillations (Friedel oscillations) in the spin density that sum to cancel the impurity magnetic moment. This is the valence-hole-mediated indirect exchange interaction. However, for III-V ferromagnetic semiconductors, the Friedel oscillations of the spin density in the valence holes around a single Mn impurity tend to average out [16]. The reason is that the typical distance between impurities is smaller than the distance between the carriers, at the typical GaMnAs

charge density $\sim 10^{14}$ cm^2 and Mn concentration $\sim 1\%$. Thus in GaMnAs the exchange interaction mediated by the carriers is ferromagnetic for most of the spin pairs.

The Zener model, which is equivalent to RKKY in the limit of low charge density and disregarding the Friedel oscillations, can successfully describe most aspects of ferromagnetism [17, 18]. In this model the exchange interaction results from carriers and localized spins and is parameterized by $N_0\beta$ (N_0 density of acceptor sites, β is the p-d exchange integral), or also known as p-d exchange where the p-orbital character comes from the valence band top while the d is from the Mn localized spin. A non zero magnetization in the GaMnAs ($M = xN_0g\mu_BS$, x magnetic impurity molefraction) produces a splitting of the valence band $\Delta E = xN_0\beta S$ which reduces the carrier energy. At the same time the magnetization M increases the energy of the localized Mn atoms. Thus the total free energy contains a contribution of the Mn magnetic impurities, ΔF_{Mn}, and the free energy of the holes, ΔF_c:

$$\Delta F_{Zener} = \Delta F_{Mn} + \Delta F_c. \tag{2.3}$$

At the Curie temperature, T_C, the two energies balance each other and ferromagnetic order is created. Dietl et al. [17] calculated within this mean field Zener theory the dependence of T_C on the density of acceptor sites:

$$T_C \sim \frac{xN_0S(S+1)\rho_S(E_F)\beta^2}{k_B}, \tag{2.4}$$

with $\rho_S(E_F)$ the spin dependent density of states at the Fermi level , which can be calculated from band structure model including the effect of exchange (see Fig. 2.3b), β can be inferred from photoemission spectroscopy measurements. The prediction for the T_C agrees quantitatively with the experimental value of 110K measured in GaMnAs with a concentration x=5% and p=0.35nm^{-3}. Another success of this mean field model is the ability to explain the magnetic anisotropy in GaMnAs. Within the same mean field model, Dietl et al.[18] successfully modelled how the easy axes reorient themselves as a function of sample parameters such as hole density or epitaxial growth lattice strains.

2.2.3 Electrical transport in a perpendicular field

Electrical transport measurements of ferromagnetic materials as function of temperature (T) and applied magnetic field (B) are a rich source of information. Consider a normal metal slab in the x-y plane (see inset Fig. 2.4), with current

flowing in the x-direction. When a magnetic field is applied along the z direction the ordinary Hall voltage [19] is generated in the transversal direction to the flow of the current. The Hall resistivity is proportional to the applied magnetic field B and is given by: $\rho_H = R_0 B$, where R_0 is the ordinary Hall coefficient ($\pm 1/nec$). The sign of R_0 depends on the nature of the charge carriers (electrons or holes) and n is the carrier density.

When the normal metal is replaced by a ferromagnetic material this picture of

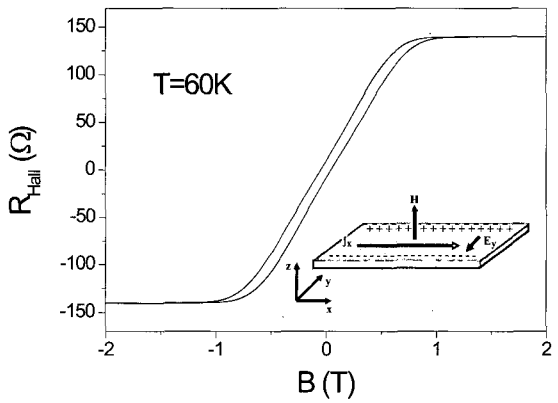

Figure 2.4: Magnetic field dependence of Hall resistance at T=60K of a GaMnAs film grown in IMEC (Mn composition is x= 0.04). The inset shows a schematic view of the Hall's experiment.

the ordinary Hall effect is complicated by the occurrence of the so-called Anomalous Hall effect [19] (AHE). Fig. 2.4 shows an up and down sweep of Hall voltage measured on a GaMnAs layer used for the work presented in Chapter 3 and grown in IMEC. Empirically the anomalous Hall effect is described by an additional term in the Hall resistivity, proportional to the magnetization M:

$$\rho_H = R_0 B + R_S(\rho) M; \tag{2.5}$$

the anomalous Hall coefficient R_S is experimentally found to depend on the resistivity, $R_S \propto \rho^\gamma$ (with $\gamma = 1$ or 2 depending on the microscopic origin of the AHE). From Eq. 2.5 it appears that at low magnetic field the ordinary Hall effect contributes less to the Hall resistivity than the AHE, thus we can write $R_H \sim R^\gamma_{Sheet} M$. Therefore the measured Hall resistance in a ferromagnetic material contains information on both the magnetism and the carrier concentration.

In practice, the extraction of n and M from the measurements is difficult due to the high charge density and to the field dependence of ρ and of $R_s(\rho)$.
A simple way to estimate the value of γ for a ferromagnet is from a linear fit of Arrott plots [20] based on the magnetotransport data (see Fig. 2.5a). The basis of an Arrott plot is a Landau description of the free energy for the ferromagnet expanded as function of the magnetization M (see Section 2.2). The free energy may be minimized with respect to M for any external magnetic field. The result of such a minimization reads:

$$M^2(B,T) = -\frac{\alpha}{\beta} + \frac{1}{\beta}\frac{B}{M} \tag{2.6}$$

with α and β opportune constant coefficients. A graph of isothermal values of M^2 *versus* B/M should result in a straight line. From Eq. 2.5 we find that $M \approx R_{Hall}/R^{\gamma}_{Sheet}$ which combined with Eq. 2.6 allow to obtain Arrott plot from magnetotransport measurements: $M^2 \approx (R_{Hall}/R^{\gamma}_{Sheet})^2$ versus $B/M \approx (B/(R_{Hall}/R^{\gamma}_{Sheet})$. The extrapolated intercept in this plot is proportional to M^2, which is zero at T_C. Thus from the temperature and field dependence of the transport quantities such as the Hall and sheet resistance, we can determine the ferromagnetic transition temperature T_C (see Fig. 2.5a). For a magnetic solid the relation between the external magnetic field, the magnetic induction and the spontaneous magnetization is linear: $\mathbf{B} = \mu_0(\mathbf{H} + \mathbf{M})$. For $B = 0$ we obtain a linear relation between the magnetic field and the magnetization $M = \chi H$, where χ is a dimensionless quantity called the magnetic susceptibility. If the anomalous hall effect dominates at low field, from Eq. 2.6 we expect $\chi \propto \{d(R_{Hall}/R_{Sheet})/dB\}_{B=0}$ which implies that from magnetotransport measurements information on the susceptibility can be extracted. In Fig. 2.5b we show a plot of $\chi^{-1} \propto \{d(R_{Hall}/R_{Sheet})/dB\}^{-1}$ versus temperature. The straight line clearly indicates that the susceptibility of GaMnAs can be described with Curie-Weiss law, $\chi \propto \frac{1}{T-T_C}$. The intersect of the linear part of $\chi^{-1}(T)$ with the T-axis occurs at the Curie temperature.
The microscopic origin of the AHE for this ferromagnetic semiconductor is of intrinsic nature, and in a semiclassical picture this is understood as a contribution to the AHE due to the change in wave packet group velocity that occurs when an electric field is applied to the ferromagnet, this gives $R_S \propto \rho^2$ [21]. Luttinger [22] was the first to demonstrate that the AHE has an intrinsic contribution, however, for long time physicist doubted about the relevance of intrinsic AHE. In general, it exists also an extrinsic contribution to the AHE, this is due to anisotropic scattering on impurity caused by spin-orbit interaction, this extrinsic

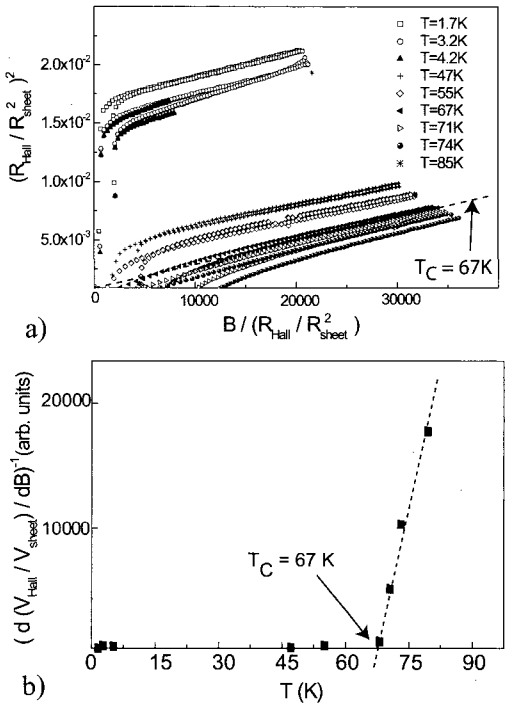

Figure 2.5: a) Arrott plots of M^2 *vs.* B/M, with $M \approx R_{Hall}/R^{\gamma}_{Sheet}$, at different temperatures from below $T_C = 67K$ to above T_C for a GaMnAs sample grown in IMEC (Mn content is x= 0.04). A value of $\gamma = 2$ is found from a linear fit of the curves. b) Plot of $\chi^{-1} \propto (d(V_{Hall}/V_{Sheet})/dB)^{-1}$ *vs.* temperature.

contribution gives $\gamma = 1$ or 2 depending on the dominant scattering mechanism, respectively skew scattering or side jump [19]. However, only recently MacDonald *et al.* [21] demonstrated that the magnitude of the AHE effect in GaMnAs is consistent with a dominance of intrinsic contribution over extrinsic.

2.3 Introduction to Superconductivity

2.3.1 Phenomenology of a BCS superconductor

In 1911 H. Kameringh Onnes in Leiden, a few years after he liquified helium, discovered that some metals display zero electrical resistance in the temperature range lower than a critical temperature T_C^S. 20 years later it was recognized that the same materials, when cooled down in this zero state resistance are also perfect diamagnets (Meissner effect). These two properties define the superconducting state.

Since the superconducting state and the normal metallic state are different thermodynamic phases of matter, a phenomenological understanding of the normal-superconductor transition can be grasped within the second order phase transition theory developed by Landau. The distinction between the normal and the superconducting phases is described by an order parameter which vanishes at the transition point. For the paramagnetic to ferromagnetic transition we discussed in Section 2.2 that the order parameter is the magnetization M. In the superconducting transition it is considered a complex order parameter $\psi(\mathbf{r})$, where $|\psi(\mathbf{r})|^2$ can be identified as the density of superconducting electrons. This is the Ginzburg-Landau order parameter [23].

This mean-field theory can describe the general features, such as what happens to the superconducting state at the interface with a normal metal and in an external magnetic field. However, this theory does not present an explanation for the microscopic origin of the superconducting state. The physical interpretation of the Ginzburg-Landau order parameter remained elusive until Bardeen Cooper and Schrieffer (BCS) proposed the microscopic theory of superconductivity [23].

2.3.2 The BCS energy gap and quasiparticles states

The key point of the microscopic interpretation of superconductivity is the occurrence of an effective attractive interaction among conduction electrons. Fröhlich[24] proposed as a possible mechanism of attraction the indirect electron-electron interaction via phonons: one electron interacts with the lattice and polarizes it, and another electron interacts with the polarized lattice. This coupling mechanism involves electrons lying near the Fermi energy E_{F} in an energy shell of the order of $\hbar\omega_D$, where ω_D is the Debye phonon frequency of the material.

A significant step towards a microscopic theory is due to Cooper[25] demonstrating that the normal Fermi sea is unstable if an arbitrary weak attractive interaction acts among the electrons. In particular pairs of electrons, undergoing

this attractive interaction, form a bound state: the Cooper pair. The ultimate understanding was reached within the BCS theory which considers a *cooperative condensation process* that minimizes the total energy of the system [23]. The result is that the energy spectrum with quasiparticles of energy $E_{\mathbf{k}}$ has an energy gap Δ. The probability of a Cooper pair in a state with momentum $\hbar\mathbf{k}$ is clearly different from zero only for an energy width Δ around the Fermi energy. This implies that the Cooper pair has a characteristic length which is the average distance in real space between the two electrons in the pair: the BCS coherence length $\xi_0 = \frac{\hbar v_F}{\pi\Delta}$. The single particle density of states for a superconductor reads:

$$D_S(E) = \begin{cases} N_0 \frac{|E-E_F|}{\sqrt{(E-E_F)^2-\Delta^2}} & \text{for } E - E_F \geq \Delta \\ \\ 0 & \text{for } E - E_F \leq \Delta \ , \end{cases} \tag{2.7}$$

where $N_0 = D(E_F)$ denotes the density of states of the superconductor in the normal state at the Fermi energy. From Eq. 2.7 we see that the density of states in the superconductor presents a singularity at the energy $E_F \pm \Delta$. The most direct proof of this density of states $D_S(E)$ came from electron tunneling experiments[26]. Consider a junction formed by a Normal metal-Insulator-Superconductor (NIS). In N all the states with $E < E_F$ are filled, while in the superconductor the quasiparticle energy has a gap Δ in energy. If a voltage bias $eV_{bias} < \Delta$ is applied across the NIS junction, there are no single particle states available in the superconductor and the conduction is blocked. When $eV_{bias} > \Delta$ there are single particle states available. The tunneling current reads:

$$I = A \int_{-\infty}^{+\infty} |T|^2 D_N(E) D_S(E + eV_{bias})[f(E) - f(E + eV_{bias})]dE, \tag{2.8}$$

where $f(E)$ is the Fermi distribution function, A is a numerical constant. As an example of tunnel differential conductance we present measurements on a tunnel junction consisting of $Nb/Al_2O_3/Al$, fabricated according to the procedure described in the Appendix. In Fig. 2.6 we report an I-V curve measured at $T = 1.6K$ with the Al in the normal state and Nb in the superconducting state. From the graph it is apparent that, at low bias the NIS exhibits high resistance (100 Ω) while at higher bias than $\simeq 1.4mV$ the resistance is much smaller (5 Ω). This is consistent with a gap $\Delta = 1.4mV$ in the density of states of the superconducting Nb. From a fit of the measured I-V curve based on Eq. 2.8 it is possible to evaluate the gap. A more accurate way to fit the superconducting gap and gain information on the quality of the NIS heterointerfaces consists in measuring the differential conductance dI/dV as function of bias V (see inset in Fig. 2.6).

The differential conductance reads:

$$G_{NS} = \frac{dI_{NS}}{dV} = G_{NN} \int_{-\infty}^{\infty} \frac{D_S(E)}{N_0} [-\frac{\partial f(E+eV)}{\partial(eV)}] dE. \tag{2.9}$$

Evidently a tunnel junction provides detailed information about the microscopics

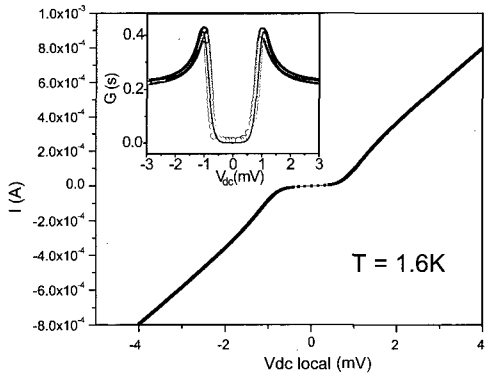

Figure 2.6: In the main graph I-V characteristic of a $Nb/Al_2O_3/Al$ tunnel junction at $T = 1.6K$. In the inset, red dots are the measured differential tunnel conductance for the same junction. The continuous black line is a fit based on Eq. 2.9, from which a superconducting gap of 1.4 mV is found.

of the superconducting state.

2.4 Transport at Normal metal/Superconductor multiterminal structures

In the previous Section we showed that the single particle density of states in a superconductor exhibits a gap, which inhibits the single particle transport for $eV_{bias} < \Delta$ trough a Normal metal-Superconductor (NS). However, this assumes only first order tunneling processes. In practice, one finds usually a higher than zero sub-gap conductance through a NS interface.

2.4.1 Andreev reflection

The understanding of the transport process regulating the conduction through a transmissive NS interface is due to Andreev[27]. Consider a clean NS interface. An electron in the normal metal is incoming to the NS interface with momentum

$\overrightarrow{k}$ and with an excitation energy ε from the Fermi energy E_F such that $\varepsilon < \Delta$ (see Fig. 2.7). Since in the superconductor the single particle density of states has a gap Δ, the incoming electron cannot propagate as a plane wave into the superconductor. In the limit $(\Delta, \varepsilon) << E_F$ (Andreev approximation) the only scattering process which can take place is Andreev reflection (AR): the incoming electron couples with a second electron in N with opposite momentum $-\overrightarrow{k}$ and energy $-\varepsilon$, they can form a Cooper pair in the superconductor. In this process 2e charge is transferred in S while a back-reflected hole is left in N. This microscopic mechanism regulates the conversion of dissipative electrical current in a normal metal into dissipationless supercurrent in the superconductor and it is the key mechanism for the superconducting proximity effect [28]. In an equivalent way we can explain the conversion of dissipationless supercurrent into dissipative normal current. In this case, an electron constituting a Cooper pair fills a hole in the N lead close by the NS interface and the other electron moves away in the normal region. Note that the conductance of a clean NS interface for $\varepsilon < \Delta$ is twice the conductance measured for $\varepsilon > \Delta$. This is simply because for low energy ($\varepsilon < \Delta$) every electron is reflected into a hole via AR, doubling the conductance compared to the case of $\varepsilon > \Delta$ where an electron can propagate directly into S.

A formal description of the Andreev reflection relies on the Bogoliubov-de-

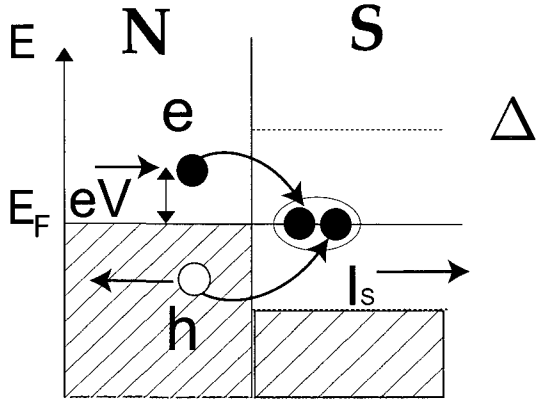

Figure 2.7: Schematic representation of the Andreev reflection process. An incoming electron in N to the N/S interface with energy $eV < \Delta$ couples with another electron at energy $-eV$ from N and they form a Cooper pair in the superconductor. In this way a dissipative current in N is converted into a dissipationless supercurrent I_S.

Gennes equations [28]. They describe the excitation spectrum of a superconductor in terms of a two component wave function (u, v), as a solution of the

equations:

$$\begin{pmatrix} H_0 & \Delta \\ -\Delta^* & -H_0^* \end{pmatrix} \begin{pmatrix} u \\ v \end{pmatrix} = \varepsilon \begin{pmatrix} u \\ v \end{pmatrix}; \tag{2.10}$$

where H_0 is the single electron Hamiltonian and Δ is the pairing potential. Given the fact that the qualitative features of Andreev reflection are independent of the precise pair potential profile, we can consider a step function for the pair potential, and uniform constant in N and in S. In particular we consider $\Delta(\overrightarrow{r})$ to be zero in N and $\Delta e^{i\phi}$ in S. One finds that there is only one kind of physically possible solution of Eq. 2.10 for a single particle propagating in the superconductor with energy below the superconductor gap: evanescent waves exponentially decaying on the scale of the superconductor coherence length ξ. In Section 2.5.2 we will show that this propagating single particle evanescent wave is the key to understand the transport processes through multiple N/S interfaces.

Phase coherence

The description of AR by means of the Bogoliubov-de-Gennes equations implies that Andreev reflection is a phase coherent process. Indeed, simply by matching the wave functions at the NS interface of the incoming and reflected particles, one finds that there is a well defined relation between the wave function of the particles involved in the scattering process. In particular, Andreev reflection is accompanied by a phase shift in particle's wave function consisting of $-\arccos(\varepsilon/\Delta)$ and $\pm\phi$ (+ for reflection from hole to electron, - for the reverse process), with ϕ the phase of the superconductor order parameter. So the AR amplitude for an electron reflected into a hole reads:

$$r_{he} = -e^{i(arccos(\varepsilon/\Delta)-\phi)}, \tag{2.11}$$

and the AR amplitude for a hole reflected into an electron reads:

$$r_{eh} = -e^{i(arccos(\varepsilon/\Delta)+\phi)}. \tag{2.12}$$

This phase shift has important implications in several different transport problems of multiterminal hybrid NS structures, such as the Andreev bound states in a Josephson junction [29], and it will be a fundamental ingredient for what we will discuss in Chapter 6.

Phase conjugation

It is interesting to note that the ingoing electron and the back-reflected hole have opposite charge, opposite momentum and opposite spin, in other words the electron and the hole are time reversed quantum states in charge, momentum and spin. A semiclassical pictures of this property suggests that the back-reflected hole will trace back all the path of the incoming electron. This fundamental property of AR is a direct consequence of the fact that the Cooper pairs in the BCS wave function are pairs of time reversed single particle states. In a quantum mechanic description, the time reversal symmetry of the electron and the hole, also implies that for an impinging electron at the Fermi energy the dynamical phase acquired by the electron ($\theta_e = \int_l \overrightarrow{k}_e d\overrightarrow{l}$) and by the hole ($\theta_h = \int_l \overrightarrow{k}_h d\overrightarrow{l}$) in a path l compensate each other. The total phase θ_{tot} acquired be electron and hole along a trajectory l reads:

$$\theta_{tot} = \int_l \overrightarrow{k}_e d\overrightarrow{l} + \theta_{AR} + \int_l \overrightarrow{k}_h d\overrightarrow{l} = \theta_{AR}, \tag{2.13}$$

where θ_{AR} is the phase shift acquired in the AR process, and $\overrightarrow{k}_{e,h}$ are the momentum of the electron and the hole respectively. If the incoming particle has a finite energy $\varepsilon \neq 0$ above the Fermi energy, the momentum of the electron and the hole are not any more equal and opposite. Consequently, the dynamical phase acquired by the hole does not cancel any more the dynamical phase acquired by the electron. In a diffusive metal in contact with a superconductor, the consequence of this breaking of phase conjugation is a decoherence of the electron and the hole involved in AR at a distance of the order of $\sqrt{\hbar D/\varepsilon}$, with D diffusion constant of the metal. These two properties of AR, phase conjugation and phase coherence, are at the origin of interference effects in transport through NS structures, investigated experimentally and theoretically by several groups [30-33].
Note that in general, for a real system the boundary between N and S is never perfectly clean. At least there exists a mismatch of the Fermi velocity in the two materials which results in scattering at the interface. Consequently, the transmissivity of a real NS interface is usually smaller than 1. However, also in the presence of a tunnel barrier at the interface the dominant mechanism of transport is Andreev reflection, although its amplitude scales with the square of the transmissivity of the interface [34].

Andreev bound states

In 1962 Josephson predicted that a supercurrent I_S flows in a Superconductor -Insulator- Superconductor (SIS) structure due to coherent tunneling of Cooper pairs: $I_S = I_c \sin(\delta\phi)$, with I_c is the maximum supercurrent that the junction can support and $\delta\phi$ is the difference of the phases of the order parameters between the superconducting leads. This was later extended also to a generic system of two superconductors connected via a weak-link, in which a supercurrent flows due to coherent transport of Cooper pairs.
Consider a normal metal of mesoscopic length L -*i.e.* the transport between the two superconductors is phase coherent. We assume zero applied bias to the SNS junction (see Fig. 2.8). The microscopic process of conduction, in a clean SNS structure must originate in the conduction at a clean single NS interface. In the Andreev reflection process the incoming electron from N to the NS interface at energy $\varepsilon << \Delta$ is back-reflected into a hole at energy $-\varepsilon$ below E_F. The hole travels in N to the other NS interface, where it will reflect back into an electron with energy ε above the E_F. In these two AR processes a Cooper pair has been transferred from one superconducting lead (*e.g.* S1) to the other (S2). Due to interference a standing wave will open in the normal metal at quantized energy: Andreev bound states [35]. The condition for the existence of a bound state, is that the total phase acquired by the electron in a period of the multiple reflections is an integer multiple of 2π:

$$-2arccos(\frac{\varepsilon}{\Delta}) \pm (\delta\phi) + k_F L \frac{\varepsilon}{E_F} = 2\pi n \tag{2.14}$$

and the sign $\pm$ is for the two directions of the multiple reflections of the electron. From Eq. 2.14 it is apparent that if there is no phase difference $\delta\phi = 0$ no net supercurrent flows in the junction. However, when $\delta\phi \neq 0$ a net supercurrent flows in the junction.

If the dynamical phase $k_F L \frac{\varepsilon}{E_F}$ is negligible, $L << \xi$, the junction is named "short" and there exist only one twofold degenerate Andreev bound state. Instead if the dynamical phase is the largest contribution, the junction is named "long". In this case for each integer value n there is a twofold degenerate bound state which transfers Cooper pairs from S1 to S2, and also its time reversal process which transfers Cooper pairs from S2 to S1. The relation between the Andreev bound state and supercurrent resides in the occupation probability.

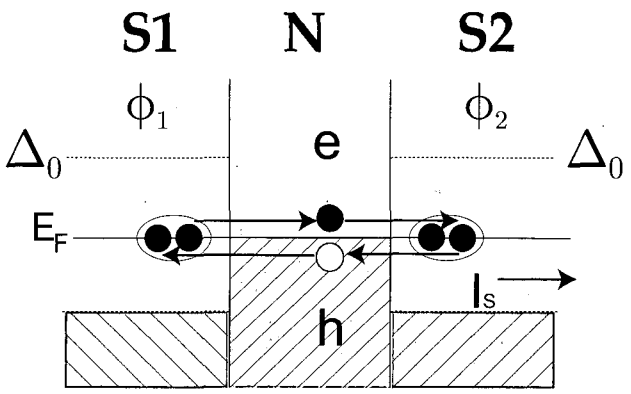

Figure 2.8: Scheme of an Andreev bound state. An incoming electron in N to the N/S2 interface, with energy $\varepsilon < \Delta$ and momentum $+k$ is back reflected via Andreev reflection into a hole with energy $-\varepsilon$ and momentum $-k$. This hole is incoming to the N/S1 interface, where is reflected into an electron. In this multiple phase coherent Andreev reflection processes 2e charge has been transferred from S1 to S2. Also the opposite process is possible, in which the electron travels to the left, resulting in a current with the opposite direction.

2.4.2 Crossed Andreev reflection and elastic cotunneling

In the previous Section we have described how Andreev reflection mediates the sub gap conduction through an NS interface. We have underlined that the solution of the Bogoliubov-de-Gennes equations for a single particle with sub gap energy in the superconductor is an evanescent wave which is suppressed on a length scale of the superconductor coherence length ξ. This characteristic length ξ describes the spatial extension of a Cooper pair and it varies from superconductor to superconductor (e.g. $\xi = 1\mu$m for Aluminum and $\xi = 40$nm for Niobium). Recent developments in nanotechnology made possible the fabrication of two NS interfaces at distances on the order of ξ, see Chapter 5. In such a superconductor based mesoscopic hybrid structure, the two electrons constituting a Cooper pair can "feel" both the NS interfaces. This opens the way to new microscopic mechanisms of conduction through the two heterointerfaces: cross conductance at multiple NS interfaces.

Consider two normal metal leads N1 and N2 contacting a common superconducting lead S on opposite sides via two tunnel barriers. Consider the thickness δr of S much smaller than ξ (see Fig.2.9). A single particle, electron or hole, from the normal lead N1 (N2) penetrates as evanescent wave through the super-

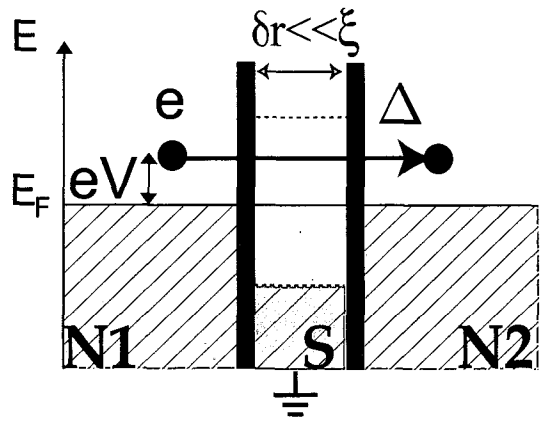

Figure 2.9: Scheme of the elastic cotunneling process in a NISIN structure. For $\delta r \ll \xi$ an incoming electron in N1 can tunnel coherently through the superconductor and appear in the spatially separated lead N2.

conductor, and the wave function has a finite amplitude at the location of the second spatially separated normal metal lead (N2). Thus, the sub gap single particle electron or hole has a finite probability to tunnel coherently from N1 (N2) through S and appear in the other normal metal lead N2 (N1). This transport process is known as Elastic cotunneling (EC): coherent tunneling of a single particle from N1 (N2) through the superconductor into N2 (N1) via a virtual state in the superconducting common electrode [36-45]. When the separation δr is much larger than ξ, the probability for electrons to tunnel coherently through the superconductor goes to zero, since the evanescent wave is suppressed according to $\sim e^{-\frac{\delta r}{\xi}}$. Thus also the Elastic cotunneling process is suppressed for $\delta r \gg \xi$.

EC is not the only microscopic transport process contributing to the cross conductance which involves the propagation of single particle evanescent waves through the superconductor, but there is a second process: crossed Andreev reflection (CAR) or non-local Andreev reflection [36-45] (see Fig. 2.10). To be able to picture this CAR process, we have to recall the mechanism of AR at one NS interface. An incoming electron in N1 is backreflected as hole in N1 and a Cooper pair is formed in S. However, in a multiterminal structure N1-I-S-I-N2 with $\delta r \ll \xi$ the incoming electron in N1 (N2) can "feel" an electron in the other spatially separated normal lead N2 (N1) (see Fig. 2.10). This implies that there is a finite probability for an electron in N1 (N2) to couple with an electron from the other spatially separated normal lead N2 (N1) and form a Cooper pair in S leaving a reflected hole in N2. What we call in a pictorial language "feeling" is

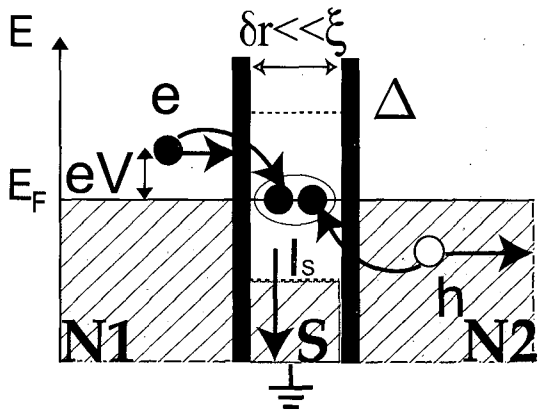

Figure 2.10: Scheme of the crossed Andreev reflection process in a NISIN structure. For $\delta r \ll \xi$ an incoming electron in N1 can couple with an electron from the spatially separated lead N2 to form a Cooper pair in S, a reflected hole is left in N2.

nothing else then the finite overlap between the two single particle evanescent waves propagating from the two normal leads N1 and N2 into the superconductor. The amplitude probability itself of both CAR and EC processes depend on this overlap of the evanescent wave functions, which is affected by the details of the geometry, as we will discuss in Section 2.5.3.
Thus in a hybrid N1-I-S-I-N2 device, with separation $\delta r \ll \xi$ between the NS contacts, we can distinguish 3 distinct processes of sub-gap conductance: elastic cotunneling (conductance G_{EC}), crossed Andreev reflection (conductance G_{CAR}) and direct Andreev reflection (conductance G_{AR}). The sub-gap current in the multiterminal NS structure can be summarized in matrix form as:

$$\begin{pmatrix} I_1 \\ \\ I_2 \end{pmatrix} = \begin{pmatrix} G_{AR,N1} + G_{CAR} + G_{EC} & G_{CAR} - G_{EC} \\ \\ G_{CAR} - G_{EC} & G_{AR,N2} + G_{CAR} + G_{EC} \end{pmatrix} \begin{pmatrix} V_1 \\ \\ V_2 \end{pmatrix}. \tag{2.15}$$

From Eq. 2.15 it is apparent that the current I_1 at probe N1 (N2) depends also on the voltage at probe N2 (N1). Furthermore, the cross conductance, the off diagonal terms in the matrix of conductance dI_1/dV_2 and dI_2/dV_1, contains the two contributions of EC and CAR which have opposite signs. Indeed, for EC an electron is injected into the lead N2 in contrast with CAR where an electron is extracted from the lead N2, resulting in opposite contributions to the cross

conductance.
A priori, in a NSN structure it is not clear which microscopic process will prevail in the cross conductance, as in fact theoretical models based on perturbation theory using an effective tunnel Hamiltonian predicted that, if charging effects are negligible the cross conductance in such a structure is zero $G_{CAR} - G_{EC} = 0$ [36-45]. In this model it was stated that a direct evidence for CAR could only be detected with noise measurements. However, as we will discuss in Chapter 5, our experimental findings are in contrast with the prediction made within a simple tunnel Hamiltonian model. Non-local transport measurements in a layered NISIN structure clearly demonstrate that the cancellation of G_{CAR} with G_{EC} does not take place. The reason why the cross conductance in our device's structure is not zero is currently field of discussion and it has motivated different theoretical models in which disorder, electron interactions, and weak localization are considered.

2.4.3 Theoretical proposals for Andreev entanglers

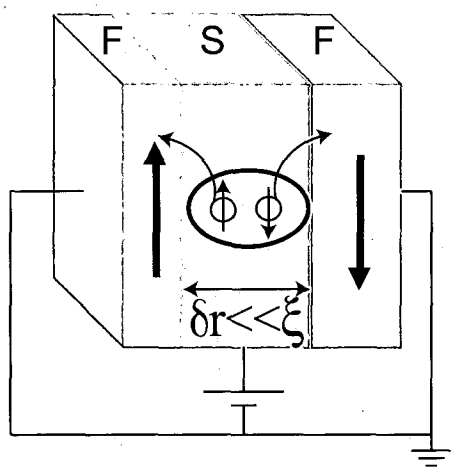

Figure 2.11: FSF multilayer with the thickness of the superconducting layer $\delta r \ll \xi$. We consider the antiparallel configuration for the magnetization of the two F leads. Electrons forming a Cooper pair are extracted into the two spatially separated magnetic electrodes, according to their spin orientation. The process of Elastic cotunneling is suppressed owing to the spin dependent density of states in a ferromagnet.

An equivalent process to non-local Andreev reflection is Cooper pair splitting.

This consists in the ejection of the two electrons constituting a Cooper pair into two spatially separated normal metal leads N1 and N2. Since the two electrons forming a Cooper pair are in a spin singlet entangled state, Cooper pair splitting opens the intriguing possibility to implement a solid state entangler -*i.e.* a device able to emit entangled electron pairs into spatially separated leads. The spin part of the wave function of the split electrons reads:

$$\Phi_{spin} = \frac{1}{\sqrt{2}}(\mid \uparrow_{N1}\downarrow_{N2}> - \mid \downarrow_{N1}\uparrow_{N2}>), \tag{2.16}$$

which, as long as the electrons remain correlated, cannot be simply written as a product of single particle wave functions. Besides the generation of entangled pairs of electrons, a crucial issue is the detection of entanglement. As we already introduced in Section 1.2, if electrons in the state described by Eq. 2.16 are injected in the arms of a mesoscopic ring, this leads to specific current fluctuations typical of the entangled nature of the electron pairs and which cannot be the consequence of any classical correlation [45]. Such a fundamental characteristic of Cooper pair splitting devices is at the origin of the strong interest in Andreev entanglers developed in modern condensed matter physics. A solid state entangler, apart from being the key ingredient for new schemes of quantum information and cryptography, it has a fundamental interest. It allows for testing in solid state devices quantum correlations which have no classical counterpart.

In order to obtain a suppression of EC in the cross conductance, thus select only the Cooper pair splitting process, different proposals were put forward using spin and energy filters [36-45]. We discuss briefly the spin filter proposal based on hybrid ferromagnet-superconductor structure [46, 47], for which the scenarios changes quite a bit compared to the case of NSN discussed previously. Two ferromagnetic leads F1 and F2 contact a common superconductor electrode (F1-S-F2) and are separated by a distance shorter than ξ (see Fig.2.11). The magnetization switching field for F1 and F2 can be engineered in such a way to have control of a distinct parallel and antiparallel magnetic configuration for the two leads F1 and F2. When the magnetizations in F1 and F2 are antiparallel an electron from F1 cannot tunnel coherently into F2 because the majority spin population in F2 has opposite spin direction than in F1. However, an electron from F1 can couple to an opposite spin electron from F2 to form a Cooper pair. Thus in the antiparallel configuration, EC is suppressed while CAR remains unchanged. In the parallel magnetization case, EC can take place since an electron from F1 can propagate in F2, however CAR is suppressed.

Another possibility to select Cooper pair splitting over tunneling of paired electrons is offered by energy filtering. Many different systems have been considered,

and the common denominator for these different proposals is charging. The electrons forming a Cooper pair have charge, and therefore the Coulomb repulsion between them can be used to prevent tunneling of paired electrons into the same lead. An example is offered by a superconductor weakly coupled to quantum dots which are then weakly coupled to normal metal leads [48]. The on site Coulomb repulsion on each dot can be used to prevent the paired electrons to tunnel into the same dot, but rather force them to tunnel via separate dots: Cooper pair splitting.

Note that the role of the charging effects in the coherent injection of the two spin-entangled electrons by Andreev process also allows a time separation of the individual Cooper pairs in the leads. The time delay between the two tunnel events of the two electrons forming a single Cooper pair is $\delta t \sim \hbar/\Delta_0$. Whereas the average time separation of subsequent Cooper pairs is given by $\Delta t = 2e/I_1$. In order to have a highly efficient Andreev entangler, it is important that $\delta t << \Delta t$. In this way correlation measurements only report correlations within the same spin-entangled pair[41]. However, it was also pointed out by Samuelsson *et al.*[49] that in the case $\delta t >> \Delta t$ it is still possible to measure the correlations within the same entangled pair of electrons if the detection time $t_{det} << \delta t,\ \Delta t$.

It was demonstrated [37, 48] that in a geometry consisting of two spatially separated leads contacting a three-dimensional superconductor via two point contacts, the current of entangled electrons is $\sim \frac{1}{(k_F \delta r)^2} exp(\frac{-2\delta r}{\pi \xi})$. The limitation imposed by the superconductor coherence length ξ on the separation between the contacts, as we discussed, is not a severe restriction. However, for smaller separation than ξ, the suppression of the entangled current is only polynomial in $1/(k_F \delta r)$, and k_F^{-1} for a superconductor is typically a few Angstroms. It was demonstrated that this power low suppression of the entangled current is very sensitive to the dimension and geometry of the device and it can be softened by a careful choice of device geometry. For example, a reduction of the dimensionality of the superconductor determines a suppression of the entangled current $\propto 1/\sqrt{k_F \delta r}$, which makes the realization of an Andreev entangler within reach of the present technology. For this reason a multilayer NSN structure is superior to a point contact geometry and in our experiment, discussed in Chapter 5, we will focus on such a multilayer structure.

2.4.4 Related experiments

Despite the large number of theoretical proposals, the experimental evidence for CAR and EC and their relation to the propagation of evanescent single parti-

cle wave functions through the superconductor common lead has proved to be difficult. An attempt to directly detect CAR in transport measurements was carried out by Beckman *et al* [50]. In this experiment two ferromagnetic leads were coupled via clean contacts to a common superconducting electrode (F1-S-F2). A scheme illustrating the measurements concept is drawn on the device SEM picture in Fig. 2.12a. The current is injected through the F1-S interface and a voltage is detected across the other interface F2-S, this is a non-local measurement. As we discussed in the previous Section, according to the relative orientation of the magnetizations in F1 and F2, EC or CAR is suppressed. In particular, for antiparallel configuration EC is suppressed, while for parallel configuration CAR is suppressed. The detected differential non-local resistance should exhibit a distinct sign according to the dominating microscopic process CAR or EC. However, in this experiment by Beckmann *et al.* [50] only the sign according to EC (see Fig. 2.12a) is measured in both the parallel and the antiparallel configuration, leaving non-local AR yet unrevealed. Furthermore, the choice of clean FS interface can have unwanted complications. Hot quasiparticles from the ferromagnet can freely go into the superconductor generating a voltage due to the non-equilibrium distribution, which hinders the signal of CAR.

An earlier experiment by Den Hartog *et al.* [51] presents non-local transport measurements in a phase coherent multiterminal Semiconductor-Superconductor (Sm-S) structure (see Fig. 2.12b). In this experiment direct Andreev reflection at one Sm-S interface is considered, which is conceptually different from the previously discussed Andreev entanglers. In the latter the focus is on the propagation of single particle evanescent waves through the superconductor between two different spatially separated interfaces, which is not the case in the Den Hartog *et al.* [51] experiment. In particular, in this Sm-S device the electron-hole transport in the semiconducting phase coherent region is dominated by sample specific interference effects, which are sensitive to an external magnetic field. It was found in some samples that as a function of applied magnetic field, for an incoming electron in lead 3 the interference in the transport was such that the reflected hole propagated in lead 1 (see Fig.2.12b). Such a sample specific process was directly detected as a negative non-local differential resistance as a function of external magnetic field.

In the same spirit of the previously discussed theoretical Andreev entanglers (Sections 2.5.2 and 2.5.3), we will show in Chapter 5 that with transport measurements in a multilayer NISIN structure, we probed successfully the tunneling of evanescent particles propagating from one N lead through S into the other spatially separated N lead. A direct observation of CAR and EC is reported and the effect is not sample specific but survives ensemble average, in fact it

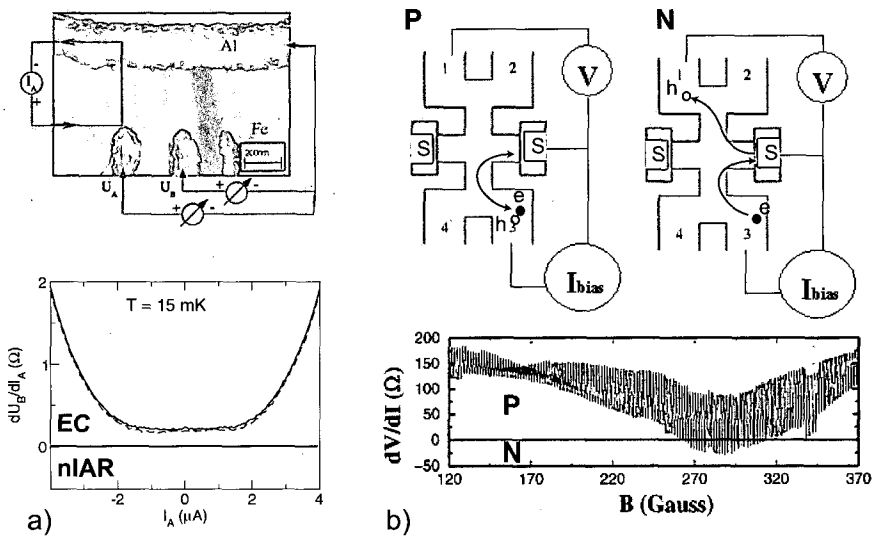

Figure 2.12: a) Top panel: SEM picture of a FSF planar device with the scheme illustrating the non-local measurements concept. Bottom panel: differential non local resistance for the parallel (solid line) and antiparallel (dashed line). A dominance of EC over CAR is clearly visible independent of the relative orientation of the magnetization direction in the two F leads. Figure from Ref. [49]. b)Top panel: scheme of the multiterminal Sem-S structure with non-local measurements circuit illustrating a positive (P) and negative (N) contribution of the electron/hole Andreev reflection to the non-local differential resistance. Bottom panel: measurement of non-local differential resistance as function of magnetic field. It is apparent a cross over from P to N. Figure from Ref. [50].

was observed systematically in all the measured devices (more than 10). We find experimentally that CAR can be selected over EC as function of a bias applied at the injecting junction. The choice of a multilayer structure with tunnel junctions at each NS interface might be crucial for the direct observation of CAR. Indeed, in a recent experiment by P. Cadden-Zimansky *et al.* [52]a clean NSN planar geometry was investigated and only a direct observation of EC was reported, demonstrating that in that particular geometry EC dominates over CAR independently from the bias applied at the injecting junction.

2.5 Electron-electron correlation effects

In Section 1.4.2 we introduced the concept of tunnel conductance of a NIS junction as a tool to access the density of states of the superconductor. In this Chapter we will discuss the modifications on the density of states of a dirty material system due to electron-electron interaction, and its appearance in the tunnel conductance. In a 3D crystal the non interacting Bloch electrons have a Density of States (DOS) dependent on energy $D(E) \propto \sqrt{|E|}$. However in a disordered metal system, such as GaMnAs, the existence of interaction between electrons (holes) on a short time scale compared to the inverse of the elastic mean free-path leads to different physics. The role of the electron-electron interaction is particularly relevant in the understanding of the metal-insulator transition (MIT) in a disordered system. This can be accessed experimentally with a great deal of accuracy in doped semiconducting systems. For doping concentrations close to the critical density n_c, the Coulomb correlations are equally relevant as localization induced by disorder, and both aspects should be taken into account by any theoretical treatment aiming to describe the MIT. The central importance for strong electron-electron interaction has been encountered in a variety of experiments. We will focus our attention on the role of Coulomb interaction in the density of states and, in particular its appearance in tunneling conductance experiments.

On the insulating side of the MIT, when all the charge carriers are localized, Efros and Shklovskii demonstrated that the role of long-range Coulomb interaction is a vanishing of the single particle density of states at the Fermi energy with the opening of a soft gap [52-55]. It was demonstrated that the Hartree part of the Coulomb interaction in a hopping conductor gives the opening of a parabolic gap at T=0K. This is the so-called Efros-Shklovskii gap or also Coulomb gap Δ_C [53]. This soft gap gives a peculiar dependence of the resistance on temperature: $\ln R = T^{-1/2}$.

On the opposite side of the MIT there is the dirty metal regime which is of most interest for the GaMnAs samples measured in this Thesis. In this case, the Coulomb interaction among electrons (holes) results in a depletion in the single particle density of state $N(E)$ near the Fermi energy [57, 58]. In this regime explicit calculations were carried out by Altshuler and Aronov [57], and they showed that in a three dimensional dirty metal $N(E) = N_0[1 + \sqrt{|E/\Delta_C|}]$, with a correlation gap Δ_C in the density of states and $N_0 = D(E_F)$ is the non interacting density of states.

An excellent method to directly access the single particle density of states is via tunneling transport experiments. We consider a system formed by a Dirty metal-Insulator-Normal metal (DIN) sample where the insulator is a potential barrier

high enough to prevent classical current flow, but at the same time thin enough to allow quantum tunneling of particles. The tunneling conductance $G(V,T)$ measured across the structure is a convolution of the density of states in the interacting material at temperature T with the Fermi-Dirac distribution function. Taking the energy scale from the Fermi energy, we can write:

$$G(V,T) \simeq \int \frac{N(E,T)}{N_0}[-\frac{\partial f(E-eV,T)}{\partial(eV)}]dE, \tag{2.17}$$

where f is the Fermi function: $f(E) = \frac{1}{1+e^{\frac{E-eV}{k_BT}}}$. From Eq.2.17, follows that for a 3D dirty metal with $N(E) = N_0[1+\sqrt{|E/\Delta_C|}]$, the electron-electron interaction causes an anomaly at zero bias in the measured tunnel conductance with the form of a cusp. At present, a clear understanding of how the Coulomb gap evolves across the MIT is missing. For this reason research is carried out on material systems in which by means of an external parameter (e.g. magnetic field or annealing temperature) it is possible to drive the material across the MIT while monitoring its density of states and the evolution of a soft gap in it. We will report on such a study on GaMnAs.

2.6 Charge pumping

2.6.1 Classical *versus* quantum electron pumping

In the previous Sections we discussed different transport mechanisms in which current flows in response to a voltage difference. In this Section we will focus on a different mechanism, known as charge pumping: a dc current flows in the device without applying a dc bias, but in response to periodic changes of the parameters of the system.

One of the most well known electron pumps are turnstile pumps. Turnstile electron pumps have been realized experimentally in metallic islands confined by tunnel barriers [59] and quantum dot (QD) system [60], small semiconductor island confined by gate electrodes and connected to the outside world via point contacts. Consider a QD with the transport in the Coulomb blockade regime. In response to AC oscillating gate voltages, which change the barrier height, an integer number of electrons is pumped during each cycle, in perfect analogy with a classical peristaltic pump. The fact that electron phase coherence and interference effects do not play a role on the pumping mechanism in a turnstile device appears clearly from the pumping cycle. In Fig. 2.13 we show a pumping cycle for QD turnstile. The pumping direction is controlled by a small dc voltage directly

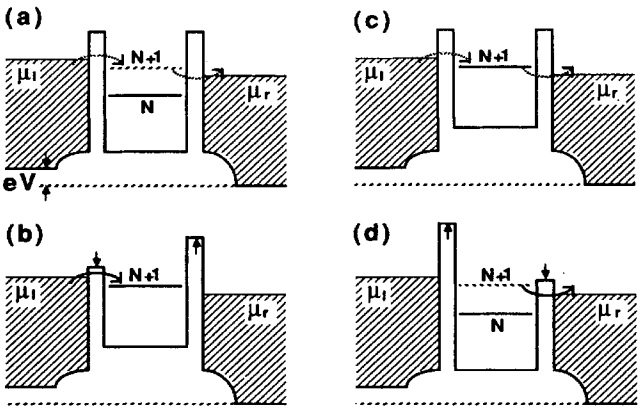

Figure 2.13: Scheme of the potential landscape through a QD turnstile device, illustrating the pumping cycle. Figure from Ref[59].

applied to the device. The left tunnel barrier of the dot is lowered while the height of the right tunnel barrier is increased. An electron from the left reservoir can tunnel in the QD, where it can loose the phase coherence by inelastic scattering events. Subsequently, the height of the left barrier is increased while the right barrier lowered and an electron can tunnel out from the QD in the right lead. In this cycle a net charge has been pumped from the left to the right reservoir, closely resembling a peristaltic pump.

In general, it was demonstrated [61, 62] that a dc pumped current is produced if two fundamental conditions are satisfied: (i) at least two independent oscillating parameters $X_1(t)$ and $X_2(t)$ act on the system; (ii) the trajectory representing the system in the parameter space (X_1, X_2) must enclose a finite area. In the case of the turnstile device, the two pumping parameters are the oscillating barriers heights. A finite phase difference between these two oscillating parameters is indeed necessary to have a finite pumped charged, this makes non zero the area enclosed by the trajectory representing the system in the parameter space (X_1, X_2).

Thouless [63], was the first to propose a new class of electron pumps, the adiabatic quantum electron pumps. He considers a mesoscopic system in which quantum coherence is maintained over the full length of the conductor. A slow periodic modulation of the particles' wave functions of the mesoscopic system is responsible for a dc pumped charge. The adiabatic approximation determines how slow the periodic modulation should be: the time scale for the cyclic variations has to be larger than all the relevant relaxation times and slower than the transport

time of the electrons in the mesoscopic device. For simplicity, we discuss the case of a travelling potential at velocity v, described by $U(x,t) = U(x-vt)$, in a ballistic conductor with one channel. The potential is periodic in time (period T) and space (wave length λ), and this is a slow periodic fluctuation which adiabatically modulates the wave functions of the electrons. A necessary condition to have pumping in the Thouless proposal is that the potential wave is travelling through the system. A standing potential wave cannot contribute to charge pumping. This can be simply justified by decomposing the travelling potential wave $U(x-vt)$ as follows:

$$U(x-vt) = X_1(t)\sin(\tfrac{2\pi x}{\lambda}) + X_2(t)\cos(\tfrac{2\pi x}{\lambda}),$$
$$X_{1,2}(t) \sim \cos(\tfrac{2\pi vt}{T} + \phi_{1,2}). \tag{2.18}$$

Evidently, if we represent the evolution of the system in the (X_1, X_2) plane, the Thouless pumping parameters trace a trajectory which include a finite area depending on the phases $\phi_{1,2}$, and a dc pumped current flows through the device.

2.6.2 Parametric pumping: a derivation based on scattering matrix

If transport in the sample under consideration is phase coherent, scattering matrix theory is a powerful formalism to describe the adiabatic pumping mechanism. We consider a generic open mesoscopic system consisting of P leads and N quantum channels in each lead. We assume that the period of these oscillations is much longer than the dwell time of the particles in the mesoscopic system, so that we are in the adiabatic approximation. The total scattering matrix describing the mesoscopic system is a function of X_1 and X_2. The demonstration of the relation between the S-matrix and the adiabatic pumped current is due to Brouwer [61], who finds that the pumped current depends on the total scattering matrix and its derivatives with respect to the oscillating pumping parameters, $\partial S/\partial X_{1,2}$. The total charge emitted through contact m in one period $\tau = 2\pi/\omega$ of the oscillating parameters is:

$$Q(m,\tau) = e\int_0^\tau dt(\frac{dn(m)}{dX_1}\frac{dX_1}{dt} + \frac{dn(m)}{dX_2}\frac{dX_2}{dt}) \tag{2.19}$$

$$\frac{dn(m)}{dX} = \frac{1}{2\pi}\sum_\beta\sum_{\alpha\epsilon m}\mathrm{Im}\frac{\partial S_{\alpha\beta}}{\partial X}S^*_{\alpha\beta}; \tag{2.20}$$

with α summed over the N channels in the contact. The quantity $dn(m)/dX$ is the emissivity into contact m. Eq. 2.19 and 2.20 show that when two or more parameters oscillate cyclically with one component out of phase, a dc pumped charge can flow in the mesoscopic device. Furthermore, we notice that a pumped current does not have a definite symmetry with respect to magnetic field reversal, unless the system itself possesses some specific discrete symmetries with respect to magnetic field.

A direct experimental observation of phase coherent adiabatic charge pumping

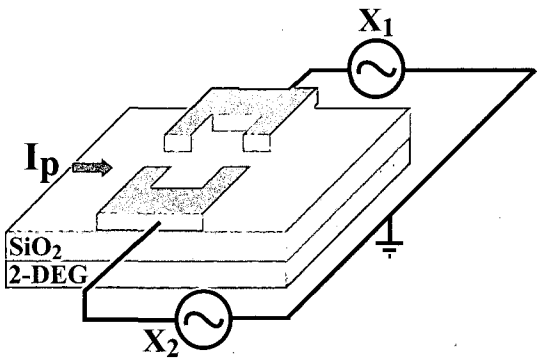

Figure 2.14: Scheme of a pumped current generated in a quantum dot system in response to two oscillating AC voltages applied to the confining gate electrodes.

has turned out to be a very challenging quest. The extreme control in the fabrication and measurement techniques achieved in mesoscopic devices fabricated with GaAs, suggested that a quantum dot system would be the simplest device to measure the occurrence of phase coherent adiabatic pumping (see Fig.2.14). In an open quantum dot system, a pumped current might occur in response to a cyclic oscillation of the QD shape.

Such an experiment was performed by Switkes [64] and the pumping parameters were two independent electrostatic gates. It was found, as expected, that a dc current flows through the quantum dot in response to the oscillating gates. The measured dc current is non zero when the two gates are oscillating with a finite phase difference, consistently with the properties of the pumped current. However, it was later demonstrated that the measured current exhibited a definite symmetry with respect to magnetic field, in contrast with what is expected for an adiabatic pumping signal. This implies that although there might have been a pumped current flowing through the QD, it was masked by current due to rectification[65]. The gate voltages in a real QD system are coupled to the elec-

tron reservoir via parasitic capacitances, which causes the QD system to act as a rectifier, making difficult the detection of a true pumped current. A distinction between rectified and pumped signal can be made on the base of symmetry upon magnetic field reversal. Since the rectified current is a function of the conductance and its derivatives, it is symmetric with respect to magnetic field reversal via the Onsager's symmetry, in contrast to the pumped current which does not have a specific dependence on field reversal.
The search for the best mesoscopic system to measure the occurrence of phase coherent adiabatic pumping is still open. In Chapter 6 we propose a device which can be operated at high frequency, as high as the Josephson frequency, and in which there is no rectified current masking the dc pumped current.

2.7 Towards spin-injection in organic semiconductors

A recently emerged material class are the organic semiconductors. They are interesting candidates to be used for spin dependent transport because the coherence time is expected to be long. Organic semiconductors are available as polymers. Here we focus on well ordered structures, organic single crystals (OSC), based on oligomers such as rubrene [66]. Organic molecular crystals are formed by regular arrangement into a crystalline lattice of organic molecules held together by van der Waals intermolecular interaction forces.
In a molecule, atomic orbitals or hybrid atomic orbitals overlap to form molecular orbitals. These can be "classified" according to the electron filling in Highest Occupied Molecular Orbital (HOMO) and the Lowest Unoccupied Molecular Orbital (LUMO). When embedded into a crystal, the combination of HOMO levels of each individual molecule contribute to the formation of what is the comparable to the valence band in inorganic semiconductors, while the LUMO's form the conduction band. In a pristine undoped sample the Fermi level lies between the HOMO and LUMO levels, and the organic crystal has a completely filled valence band and an empty conduction band.
However, by means of the field-effect [67] charge can be accumulated electrostatically at the surface of an organic semiconductor. Field-effect is a powerful tool to study the charge transport and charge injection at metal-organic interface [68, 69]. For an intrinsic OSC implemented in a metal-insulator-semiconductor structure, the majority of free carriers is supplied by the source and drain contacts. Thus the work function of the contact and the relative alignment with respect to the energy levels of the OSC, is expected to play a major role. Typically an organic

single crystal FET relies on the following fabrication steps: pre-patterning of the substrate with metallic source and drain contacts on top of an oxide layer (gate dielectric) which separates the back gate from the contacts; and lamination of the OSC on this pre-patterned substrate (see Fig. 2.15a and Fig. 2.15b). The charge carriers are injected from the source contact into the OSC and through the conduction channel reach the drain contact. When a voltage is applied between the back gate electrode and the source, an electric field is created in the channel of conduction which modulates charge density induced at the OSC-dielectric interface.

The principle of charge accumulation can be simply understood when looking at the energy level band diagram for the region Gate-Insulator-Semiconductor (see Fig. 2.15c). When the gate voltage compensates for the difference in the Fermi levels of both gate and semiconductor, the energy bands in the semiconductor will be flat. This gate voltage is referred to as the flat-band voltage V_{FB}. We consider a p-type semiconductor, a gate voltage lower than V_{FB} bends the band in the semiconductor in such a way that positive charge is accumulated at the interface gate dielectric-semiconductor. *Vice versa*, when $V_G > V_{FB}$ free holes in the semiconductor are expelled from the interface region creating a depletion zone at the interface with the gate.

A typical FET characteristic exhibits a *linear regime* and a *saturation regime*. In the linear regime the total source-drain current (I_{SD}) in the FET depends linearly on the source-drain voltage (V_{SD}) and on the gate voltage:

$$I_{SD} = \frac{W}{L}\mu C_i(V_G - V_T)V_{SD}; \tag{2.21}$$

with L and W channel length and width, C_i capacitance of the gate dielectric, μ charge mobility and V_T threshold voltage. The linear regime is valid for low V_{SD} compared to $V_G - V_T$. When the source-drain voltage is increased, the electric field applied by the gate in the region surrounding the drain contact becomes zero, and there is no longer charge induced at the oxide-organic interface (pinch-off). If V_{SD} further increases, the I_{SD} is independent of the source-drain voltage but it depends quadratically on V_G (saturation regime):

$$I_{SD} = \frac{W}{2L}\mu C_i(V_G - V_T)^2. \tag{2.22}$$

Eqs. 2.21 and 2.22 are used to characterize charge mobility in an organic FET and, in Chapter 7 we will elaborate more on how to extract information on the contact resistance from the FET characteristic.

Furthermore, OSC are a very promising material system for spintronics devices since they hold expectations for a long spin coherence time [69,72]. There are

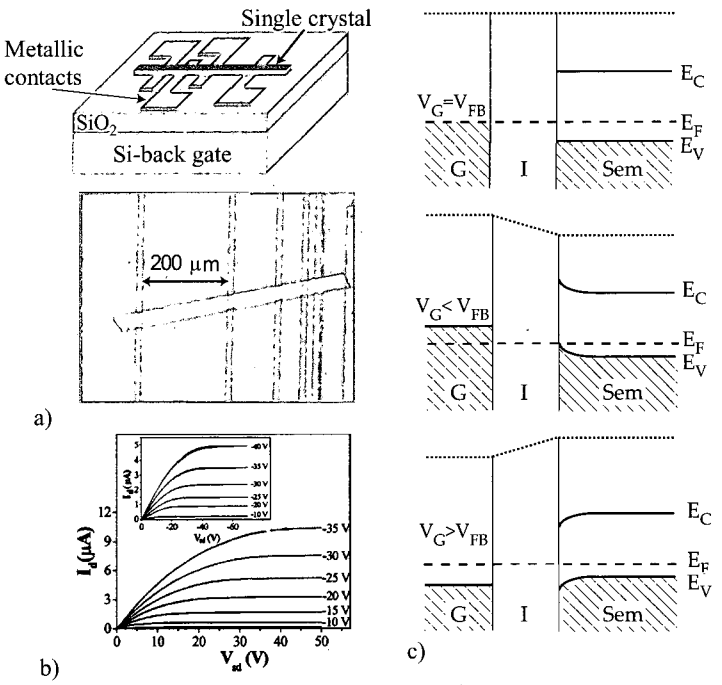

Figure 2.15: a) Top panel: scheme of a FET with OSC obtained by lamination of the organic crystal on a prepatterned substrate with electrodes. Bottom: Micrograph of a FET device with OSC. b) In the main figure sourcedrain current vs sourcedrain voltage measured at different gate voltages for a device fabricated on SiO2, with an L=1.2 mm channel length and W=200 mm channel width. The linear regime and saturation regime can be distinguished. In the inset plot of similar measurements for a device fabricated with a different gate dielectric material. Figure from Ref.[Ruth thesis 65]. c) Energy level band diagram of a metal-insulator-p-type semiconductor, from top to bottom: flat band condition, accumulation and depletion.

two main reasons supporting the idea of a long spin coherence time in organic semiconductors: small spin-orbit interaction and negligible hyperfine interaction. Spin-orbit interaction is the consequence of the effective magnetic field felt by the electrons moving in an atomic orbital due to the electric field of the nucleus. However, organic materials consist mainly of light atoms (small atomic number Z) and the smaller Z the smaller the electric field due to the nucleus. Consequently, organic semiconductors are expected to have a very small spin-orbit interaction. Another cause of spin decoherence is the hyperfine interaction. A

non vanishing wave function of the conduction carriers at the nucleus leads to a direct magnetic coupling between the magnetic moment of the nucleus and of the carriers. However, for π-conjugated molecules such as rubrene, the π-electrons are delocalized on parallel planes above and below the plane of the nucleus, thus hyperfine interaction is probably negligible [74].
In the experiment reported in Chapter 7 we have been able to make a first step towards integrating these organic semiconductors with a ferromagnetic contact. This experiment demonstrate that Ni is a very suitable contact material for organic FETs. However, for an efficient spin injection, tunnel barriers at the ferro-organic interfaces are necessary (see Section 1.3) and this constitutes the focus of our present research.

Bibliography

[1] S. Chikazumi, Physics of Ferromagnetism, Oxford: Clarendon Press, 1997.

[2] T. Kasuya and A. Yanase, Rev. Mod. Physics **40**, 684 (1968).

[3] H. Ohno and F. Matsukura, Solid State Commun. **117**, 179 (2001).

[4] See T. Jungwirth *et al.*, Rev. Mod. Phys. **78**, 809 (2006) and references there in.

[5] H. Ohno, J. Mag. Mag. Mater. **200**, 110 (1999).

[6] H. Munekata *et al.*, Phys. Rev. Lett. **63**, 1849 (1989).

[7] K. Y. Wang *et al.*, Proceedings of the 27th International Conference on the Physics of Semiconductors, edited by J. Menendez and C. G. Van de Walle, AIP Conf. Proc. No. 772 (AIP, Melville, NY), p. 333 (2005).

[8] Semiconductor Spintronics and Quantum Computation, Eds. D. D. Awschalom, D. Loss and N. Samarth. Berlin: Springer-Verlag (2002).

[9] F. Matsukura *et al.*, Phys. Rev. B **57**, R2037 (1998).

[10] R. Shioda *et al.*, Phys. Rev. B **58**, 1100 (1998).

[11] L. M. Sandratskii, P. Bruno and J. Kudrnovský, Phys. Rev. B **69**, 195203 (2004).

[12] Y. Satoh *et al.*, Physica E **10**, 196 (2001).

[13] S. von Molnar *et al.*, J. Magn. Magn. Mater. **93**, 356 (1991).

[14] H. Ohno *et al.*, Nature **408**, 944 (2000).

[15] D. Chiba, F. Matsukura and H. Ohno, Appl. Phys. Lett. **89**, 162505 (2006).

[16] T. Ditel, A. Haury and Y. Merle d'Aubigne, Phys. Rev. B **55**, R3347 (1997).

[17] T. Dietl *et al.*, Science **287**, 1019 (2000).

[18] T. Dietl, H. Ohno and F. Matsukura, Phys. Rev. B **63**, 195205 (2001).

[19] The Hall effect and its applications, Edited by C. L. Chien and C. R. Westgate. New York: Plenum press (1980).

[20] A. Arrott, Phys. Rev. Lett. **108**, 1394 (1957)

[21] T. Jungwirth, Q. Niu and A. H. MacDonald, Phys. Rev. Lett. **88**, 207208 (2002).

[22] J. M. Luttinger, Phys. Rev. **112**, 739 (1958).

[23] M. Tinkham, Introduction to Superconductivity, New York: McGraw-Hill 2nd. edition (1996).

[24] H. Fröhlich, Phys. Rev. **79**, 845 (1950).

[25] L. N. Cooper, Phys. Rev. **104**, 1189 (1956).

[26] I. Giaever, Phys. Rev. Lett. **5**, 147 (1960); 464 (1960).

[27] A. F. Andreev, Sov. Phys. JETP **19**, 1228 (1964).

[28] P. G. de Gennes, Superconductivity of metals and alloys, Addison-Wesley, 1966.

[29] A. F. Morpurgo, Andreev bound states and spin-orbit Berry's phase in high quality InAs/AlSb heterostructures, PhD thesis (1998).

[30] B.J. van Wees *et al.*, Phys. Rev. Lett. **69**, 510 (1992).

[31] K.-M.H. Lenssen, M.R. Leys and J.H. Wolter, Phys. Rev. B **58**, 4888 (1998).

[32] C.W.J. Beenakker, Phys. Rev. B **46**, R12841 (1992).

[33] Y.V. Nazarov, Phys. Rev. Lett. **73**, 1420 (1994).

[34] G. E. Blonder, M. Tinkham and T. M. Klapwijk, Phys. Rev. B **25**, 4515 (1982).

[35] I.O. Kulik, Zh. Eksp. Teor. Fiz. **57**, 1745 (1969), [Sov. Phys. JETP **30**, 944 (1970)].

[36] G. Deutscher and D. Feinberg, Appl. Phys. Lett., **76**, 487 (2000).

[37] G. Falci, D. Feinberg, and F. W. J. Hekking, Europhys. Lett. **54**, 255 (2001).

[38] P. Recher, E. V. Sukhorukov and D. Loss, Phys. Rev. B **63**, 165314 (2001).

[39] N. M. Chtchelkatchev *et al.*, Phys. Rev. B **66**, 161320 (2002).

[40] C. Bena *et al.*, Phys. Rev. Lett. **89**, 037901 (2002).

[41] P. Samuelsson, E. V. Sukhorukov and M. Büttiker, Phys. Rev. Lett. **91**, 157002 (2003).

[42] P. Recher and D. Loss, Phys. Rev. Lett. **91**, 267003 (2003).

[43] E. Prada and F. Sols, Eur. Phys. J. B **40**, 379 (2004).

[44] G. Bignon *et al.*, Europhys. Lett. **67**, 110 (2004).

[45] G. Burkard, D. Loss and E.V. Sukhorukov, Phys. Rev. B **61**, R16303 (2000).

[46] D. Feinberg and G. Deutscher, Physica E **15**, 88 (2002).

[47] F. Giazotto *et al.*, Phys. Rev. Lett. **97**, 087001 (2006).

[48] P. Recher, Correlated spin transport in nanostructures: entanglement creation and spin filtering, PhD thesis (2003).

[49] P. Samuelsson, E.V. Sukhorukov and M. Büttiker, Phys. Rev. Lett. **92**, 026805 (2004).

[50] D. Beckmann, H. B. Weber, and H. v. Löhneysen, Phys. Rev. Lett. **93**, 197003 (2004).

[51] S. G. den Hartog *et al.*, Phys. Rev. Lett. **77**, 4954 (1996).

[52] P. Cadden-Zimansky and V. Chandrasekhar, Phys. Rev. Lett. **97**, 237003 (2006).

[53] A.L. Efros and B.I.Shklovskii, J. Phys. C **8**, L49 (1975).

[54] J.G. Massey and M. Lee, Phys. Rev. Lett. **50**, 4266 (1995).

[55] H.B. Chan *et al.*, Phys. Rev. Lett. **79**, 2867 (1997).

[56] E. Bielejec, J. Ruan and W. Wu, Phys. Rev. Lett. **87**, 036801 (2001).

[57] B.L. Altshuler and A.G. Aronov, Solid State Commun. **30**, 115 (1979).

[58] W.L. McMillan, Phys. Rev. Lett. **24**, 2739 (1981).

[59] H. Pothier *et al.*, Europhys. Lett. **17**, 249 (1992).

[60] L. P. Kouwenhoven *et al.*, Phys. Rev. Lett. *67*, 1626 (1991).

[61] P. W. Brouwer, Phys. Rev. B **58**, R10135 (1998).

[62] F. Zhou, B. Spivak and B.L. Altshuler, Phys. Rev. Lett. **82**, 608 (1999).

[63] D.J. Thouless, Phys. Rev. B **27**, 6083 (1983).

[64] M. Switkes *et al.*, Science **283**, 1905 (1999).

[65] P. W. Brouwer, Phys. Rev. B **63**, 121303 (2001).

[66] R. W. I. de Boer, Organic single-crystal field-effect transistors, PhD thesis (2005).

[67] S. M. Sze, Physics of semiconductor devices. Wiley: New York (1981).

[68] M. E. Gershenson, V. Podzorov, and A. F. Morpurgo, Rev. Mod. Phys. **78**, 973 (2006).

[69] Organic Electronics: Materials, Manufacturing and Applications , Ed. H. Klauk, John Wiley & Sons, New York (2006).

[70] V. I. Krinichnyi, Synth. Met. **108**, 173 (2000).

[71] Z. H. Xiong *et al.*, Nature **427**, 821 (2004).

[72] V. Dediu *et al.*, Solid State Commun. **122**, 181 (2002).

[73] S. Pramanik *et al.*, Nature Nanotechnology, Published online: 18 March 2007.

[74] A possible role of hyperfine interaction in organic magnetoresistance effects measured in thin films is currently been discussed. However, at the present there is no similar experimental evidence for π-conjugated organic single crystals. See Y. Sheng, T.D. Nguyen, G. Veeraraghavan *et al.*, Phys Rev. B **75**, 035202 (2007).

Chapter 3

Magnetotransport in GaMnAs

The results presented in this Chapter have been published as S.T.B. Goennenwein, S. Russo, A.F. Morpurgo, T.M. Klapwijk, W. van Roy and J. de Boeck, *Phys. Rev. B* **71**, 193306 (2005) and S. Russo, S. T. B. Goennenwein, A. F. Morpurgo, T. M. Klapwijk, W. Van Roy, and J. De Boeck AIP Conf. Proc. **850**, 1275 (2006).

3.1 Introduction

We have performed a systematic investigation of the longitudinal and transverse magnetoresistance of a single ferromagnetic domain in $Ga_{1-x}Mn_xAs$. We find that, by taking into account the intrinsic dependence of the resistivity on the magnetic induction, an excellent agreement between experimental results and theoretical expectations is obtained. Our findings provide a detailed and fully quantitative validation of the theoretical description of magnetotransport through a single ferromagnetic domain. Our analysis furthermore indicates the relevance of magneto-impurity scattering as a mechanism for magnetoresistance in $Ga_{1-x}Mn_xAs$.

3.2 Anisotropic magnetoresistance and single domain model

The resistance of ferromagnetic materials is a function of the relative orientation between the magnetization $\mathbf{M}$ and the current density $\mathbf{j}$. In general, the orientation of $\mathbf{M}$ depends on the externally applied magnetic field, which results in an anisotropic magnetoresistance (AMR) characteristic of ferromagnets[1, 2]. Although a vast amount of work has been devoted to the study of this magnetization-induced AMR in the past, a complete quantitative analysis of the magnetoresistive behavior of a single ferromagnetic domain has not been performed yet.

It was found theoretically long ago from simple symmetry considerations that, for isotropic materials, the AMR of a single ferromagnetic domain can be described by the two equations[1, 2]

$$E_{\text{long}} = j\rho_{\text{long}} = j\rho_{\perp} + j\left(\rho_{\parallel} - \rho_{\perp}\right)\cos^2\phi_M, \tag{3.1}$$

$$E_{\text{trans}} = j\rho_{\text{trans}} = j\left(\rho_{\parallel} - \rho_{\perp}\right)\sin\phi_M\cos\phi_M. \tag{3.2}$$

Here, E_{long} and E_{trans} are the components of the electric field along and perpendicular to $\mathbf{j}$, $\rho_{\parallel}$ and $\rho_{\perp}$ are the value of resistivity measured when $\mathbf{j}||\mathbf{M}$ and $\mathbf{j} \perp \mathbf{M}$, and ϕ_M is the angle between $\mathbf{M}$ and $\mathbf{j}$. These equations – to which we will refer to as the single domain magnetoresistance (SDM) model – are expected to account for the behavior of the longitudinal *and* the transverse voltage drop generated by a current flowing through a ferromagnet. Given that the relative orientation between $\mathbf{j}$ and $\mathbf{M}$ is known, the only quantities that are needed to describe the (in general) complex AMR behavior observed experimentally are $\rho_{\parallel}$ and $\rho_{\perp}$.

In conventional metallic ferromagnets such as Ni or Co, a full quantitative validation of the SDM model is difficult. Extensive investigations of the longitudinal magnetoresistance have been performed, but the relatively small magnitude of the transverse (Hall-like) signal prevents a precise quantitative comparison of experimental data to Eq. 3.2. In the ferromagnetic semiconductor $Ga_{1-x}Mn_xAs$, the situation is different. A very large transverse electric field ("giant" planar Hall effect) has been recently reported[3] and its dependence on the magnetization orientation found to be in excellent quantitative agreement with the predictions of Eq. 3.2. However, the very rich behavior of the longitudinal electric field has not been quantitatively analyzed so far.

3.3 Experiment

In this Chapter, we investigate magnetotransport through a single domain of GaMnAs to perform a detailed and complete test of Eq. 3.1 and (3.2) of the SDM model. Our work is based on measurements of the longitudinal and transverse magnetoresistance for many different orientations of the applied in-plane magnetic field. Specifically, we first analyze a selected set of these measurements to determine the parameters of the SDM model, including a linear dependence of $\rho_\parallel$ and $\rho_\perp$ on the magnetic induction $\mathbf{B}$ (i.e., $\rho_\perp, \rho_\parallel \propto -\mu_0|\mathbf{H}+\mathbf{M}|$). We then use the values of the parameters so determined to perform a fully quantitative comparison between the predictions of the SDM model and magnetotransport measurements in arbitrary orientations of the in-plane magnetic field. We find an excellent agreement between theory and experiments in all cases, for *both* the longitudinal and the transverse magnetoresistance. The results presented here conclusively demonstrate the full quantitative validity of the SDM model, and confirm that the low-field AMR in $Ga_{1-x}Mn_xAs$ is determined by one single domain reversing its orientation via abrupt switches of approximately 90° [4, 3, 5]. In addition, our findings also indicate the relevance of magneto-impurity scattering as a source of intrinsic magnetoresistance in $Ga_{1-x}Mn_xAs$.

The $Ga_{1-x}Mn_xAs$ thin films studied were grown by molecular beam epitaxy on (100)-oriented, semi-insulating GaAs wafers. Here, we will focus on a sample with Mn content $x = 0.07$, thickness $d = 57$ nm, and Curie temperature $T_C \approx 80$ K. The thin film was patterned into 200×50 μm^2 Hall bar mesas using photolithography and wet chemical etching, with the long axes of the Hall bars aligned along the crystallographic [110] direction to within experimental accuracy. For the magnetotransport experiments, the samples were mounted on a

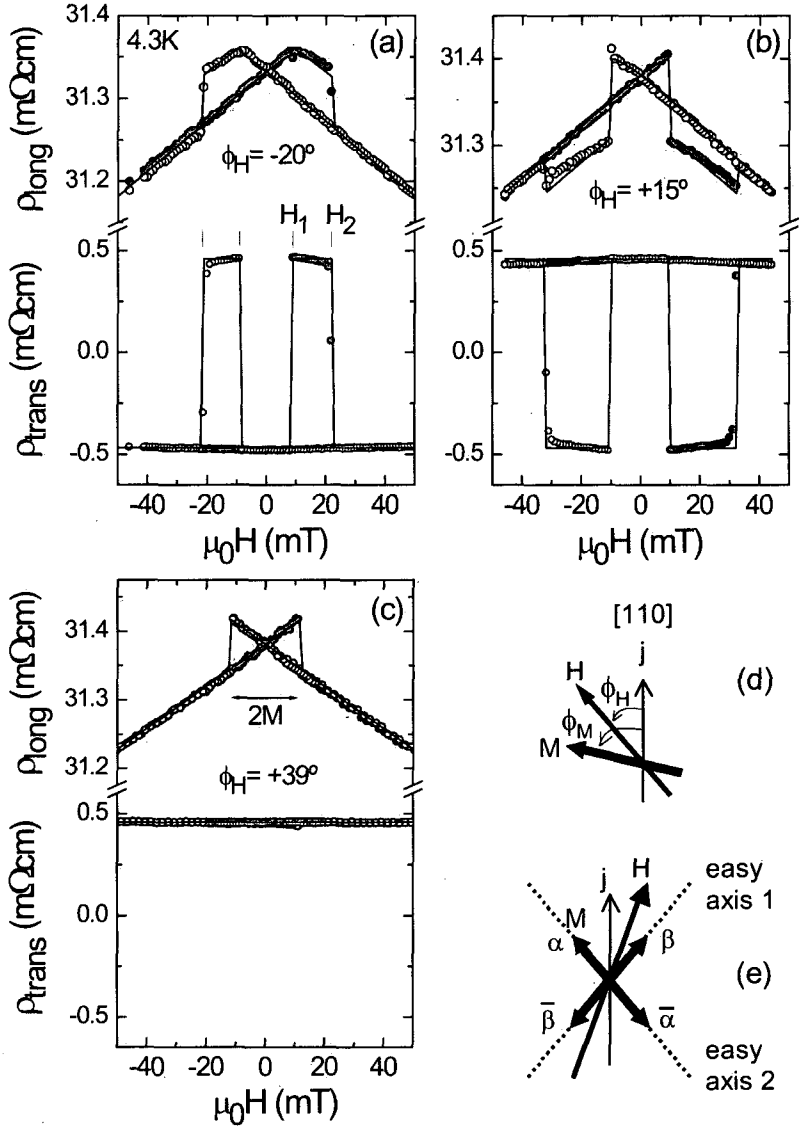

Figure 3.1: Panels (a–c) show the longitudinal and transverse magnetoresistance of a single $Ga_{1-x}Mn_xAs$ ferromagnetic domain, measured for three different orientations of the in-plane magnetic field ($\phi_H = -20°, +15°$, and $+39°$, respectively). In all panels, full symbols represent the data measured for an increasing magnetic field H (up-sweep) and the open symbols those measured with a decreasing field (down-sweep). The full lines represent the resistances calculated from Eqs. 3.1 and 3.2, as discussed in the text. Panel (d) defines the angles ϕ_H and ϕ_M between the field **H**, the magnetization **M**, and the current density **j**. Panel (e) illustrates the orientation of the two easy axes in $Ga_{1-x}Mn_xAs$ with respect to the direction of the current flow. When the field H is swept, magnetization reversal occurs by subsequent, $\approx 90°$-switches, e.g. $\beta \rightarrow \overline{\alpha} \rightarrow \overline{\beta}$.

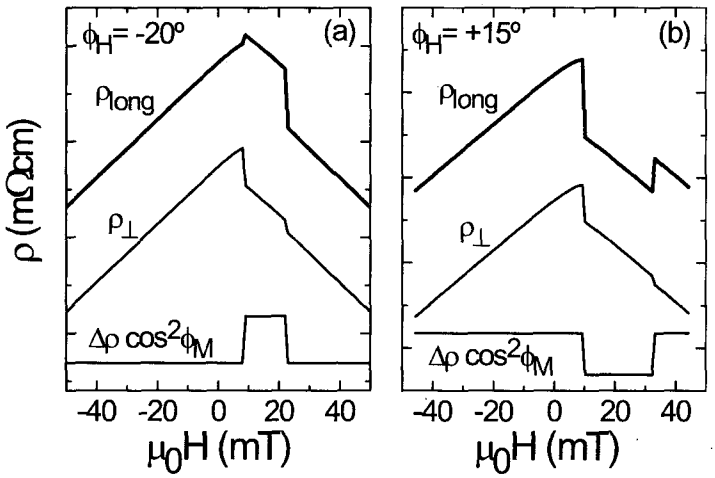

Figure 3.2: Panel (a) and (b) illustrate the behavior of the different contributions to the longitudinal magnetoresistance (thin lines) as well as their sum (i.e., the total longitudinal resistance; thick line), as calculated from Eq. 3.1 for two different orientations of the in-plane field ($\phi_H = -20°$ and $+15°$). All the traces are offset for clarity. The first term, $\rho_\perp$, is proportional to the magnitude of the magnetic induction vector. The second term, $(\rho_\parallel - \rho_\perp)\cos^2(\phi_M) = \Delta\rho\cos^2(\phi_M)$, reflects the abrupt switches of ϕ_M. A comparison between calculations and experimental data is shown in Fig. 3.1(a,b) and in Fig. 3.3.

rotatable sample holder and inserted into the He cryostat of a superconducting magnet. $\rho_{\rm long}$ and $\rho_{\rm trans}$ were simultaneously recorded in ac current-bias 4-probe measurements, using a lock-in technique. In all experiments discussed here, the external magnetic field **H** was applied in the plane of the thin film. The rotatable holder enabled us to choose the angle ϕ_H between **j** and **H** (see Fig. 3.1(d)) with an accuracy of about 1°.

The rich features in the low-field, anisotropic magnetoresistance of $Ga_{1-x}Mn_xAs$ are illustrated in Figure 3.1, which shows the magnetoresistance measured for three different orientations of the in-plane magnetic field. It is apparent that the shape of the observed magnetoresistance, which is in general hysteretic as expected for a ferromagnet, strongly depends on the field direction. Whereas $\rho_{\rm trans}$ only switches between two different and approximately constant levels (of $\simeq \pm 0.45$ mΩcm), $\rho_{\rm long}$ exhibits a more complex behavior. Note, in particular, that even for those field orientations in which $\rho_{\rm trans}$ does not show any dependence on H ($\phi_H = +39°$, Fig. 3.1(c)), a strong field dependence as well as hysteresis

are still present in ρ_{long}. While similar observations have already been reported, no full quantitative analysis has been performed: the complexity of the behavior of the longitudinal magnetoresistance demonstrates that for the validation of the SDM model, a careful test of both Eq. 3.1 and 3.2 is needed.

3.4 Comparison to the single domain model

The analysis of the transverse magnetoresistance signal and the comparison to Eq. 3.2 is identical to what has been discussed by Tang *et al.* in Ref. [[3]], to which we refer the reader for details. Here, we simply summarize the results which are needed in the analysis of the longitudinal magnetoresistance.[4, 3, 5, 6, 7] In particular, the transverse in-plane magnetoresistance and its dependence on the orientation of the external magnetic field can be completely understood in terms of abrupt changes of the magnetization orientation in the $Ga_{1-x}Mn_xAs$ layer. At low temperature and in the magnetic field range used in our experiments, the magnetization is always parallel or anti-parallel to one of the two easy magnetic axes. These axes point approximately along the [100] and [010] directions (Fig. 3.1(e)) due to the dominant cubic magnetic anisotropy, onto which a small uniaxial in-plane anisotropy is superimposed. When the magnetic field is swept, magnetization reorientation occurs via the nucleation and rapid expansion of a 90° domain.[4] On the time scale of magnetotransport experiments, this process appears as an abrupt switch of the direction of **M**. It takes place when the energy gained by the magnetization reorientation becomes larger than a fixed domain wall pinning energy. From the analysis of the transverse magnetoresistance in our samples, we find that the orientations of the two easy axes correspond to $\phi_H = +39°$ (direction α in Fig. 3.1(d)) and $\phi_H = -42°$ (direction β). The fields H_1 and H_2, at which the magnetization switches, are quantitatively consistent with the above magnetization reorientation picture for all field orientations ϕ_H. Finally, from the analysis of ρ_{trans} we obtain that $\rho_{\parallel} - \rho_{\perp} = 0.96$ mΩcm, independent of H. All these results fully agree with the findings of Ref. [[3]] and validate Eq. 3.2.

We now proceed to the analysis of ρ_{long}. We start by considering the simplest case, in which the applied magnetic field is oriented along one of the easy axes (e.g., $\phi_H = +39°$; see Fig. 3.1(c)). In this case, upon sweeping the external magnetic field, the magnetization simply reverts its direction ($H_1 = H_2$, and ϕ_M switches from +39° to $(39 + 180)°$). As a consequence, the $\cos^2(\phi_M)$ term in Eq. 3.1, as well as the $\sin(\phi_M)\cos(\phi_M)$ term in Eq. 3.2, are constant upon magneti-

zation reversal. This is indeed observed experimentally in the behavior of ρ_{trans}, which is exactly constant for this particular orientation of the external field (see Fig. 3.1(c)). Nevertheless, it is apparent from Fig. 3.1(c) that a linear magnetoresistance, as well as resistance jumps at the magnetic field values for which $\mathbf{M}$ reverses, still are present in ρ_{long}. Since the second term on the right-hand side of Eq. 3.1 does not vary with H, we conclude that the linear magnetoresistance and the jumps observed experimentally in ρ_{long} originate from a magnetic field dependence of $\rho_\perp$, i.e., the first term on the right-hand side of Eq. 3.1.

The observed behavior can be understood if $\rho_\perp$ is a function of $B = |\mu_0(\mathbf{H} + \mathbf{M})|$, since then the reversal of $\mathbf{M}$ results in an abrupt change of B and, consequently, of $\rho_\perp$. To reproduce the experimental data, we take $\rho_\perp(B) = a + b \times B$ with $a = 30.85$ mΩcm and $b = -3.06$ mΩcm/T. The continuous line superimposed on top of the ρ_{long} data in Fig. 3.1(c) illustrates the precision with which the chosen $\rho_\perp(B)$ reproduces the experimental data for $\phi_H = +39°$. In what follows, we will use this dependence of $\rho_\perp$ on B to analyze the longitudinal magnetoresistance for all the other field orientations, with *one and the same value of the parameters a and b given above.* The microscopic origin of the B-dependence of $\rho_\perp$ will be discussed at the end.

We also note that the linear dependence of $\rho_\perp$ on B allows us to extract the magnitude of $\mathbf{M}$ in our samples. In particular, it follows from the linear dependence of $\rho_\perp$ on B that the difference in H between the two jumps in ρ_{long} corresponds to $2M$ (Fig. 3.1(c)). The magnetization thus obtained is $\mu_0 M = 12$ mT, which is somewhat smaller than the saturation magnetization that one would expect from the nominal Mn content $x = 0.07$ assuming that all the spins are aligned. Such a magnetization deficit is often observed in $Ga_{1-x}Mn_xAs$ [8-10].

The analysis of $\rho_\perp$ for $\phi_H = +39°$ and of ρ_{trans} completely determines all quantities entering Eq. 3.1 and 3.2. We thus can now check if the SDM model reproduces the magnetoresistance behavior observed experimentally for arbitrary orientations of the applied in-plane magnetic field. We emphasize that at this point, there are no adjustable parameters: we just use the SDM model to calculate the magnetoresistance and see if the theoretical curves match the experimental ones. To illustrate how the theoretical curves are calculated, we have plotted the different terms on the right-hand side of Eq. 3.1 separately in Fig. 3.2 for two specific orientations ϕ_H of the external magnetic field.

The behavior of the $\cos^2\phi_M$-term is completely analogous to the $\sin\phi_M\cos\phi_M$-term in Eq. 3.2. It reflects the abrupt changes in the magnetization orientation ϕ_M as the field is swept. When the magnetization switches from one easy axis to the other at the fields H_1 and H_2, the magnitude of $(\rho_\parallel - \rho_\perp)\cos^2\phi_M$ abruptly changes, resulting in square-like steps. The behavior of the first term, $\rho_\perp(B)$, is

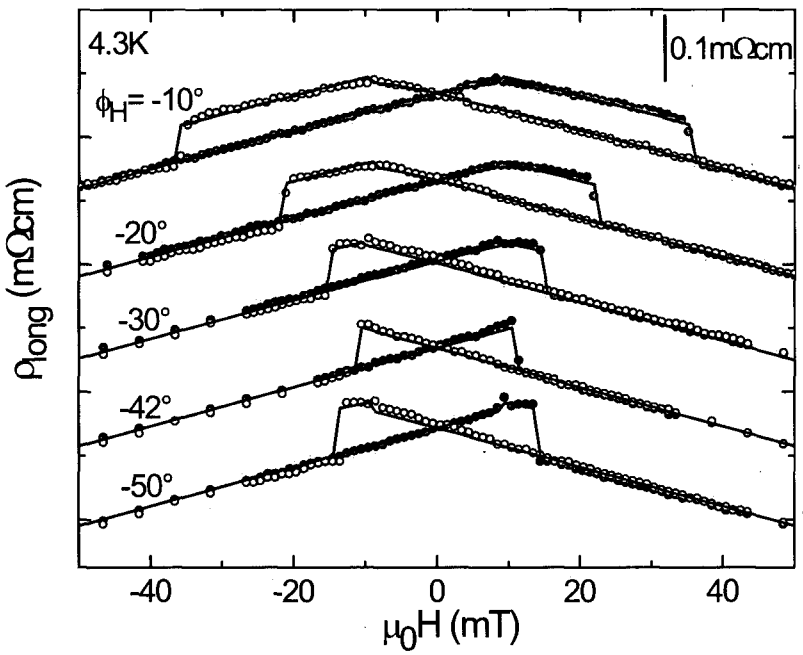

Figure 3.3: Comparison between the longitudinal magnetoresistance measured for different orientations ϕ_H of the magnetic field (symbols) and the predictions by Eq. 3.1 of the SDM model (full lines) in which all parameters have been fixed by our analysis. The magnetoresistance traces have been offset for clarity. Full symbols represent the experimental data measured for magnetic field up-sweeps, open symbols correspond to the data measured for magnetic field down-sweeps.

different. Because $\rho_\perp(B) \propto |\mathbf{H} + \mathbf{M}|$, this term retraces the magnitude of the magnetic induction vector. The abrupt reorientations of $\mathbf{M}$ also lead to abrupt steps in $|\mathbf{H} + \mathbf{M}|$, the magnitude of which is different for different orientations of $\mathbf{H}$, due to the vectorial addition of $\mathbf{M}$ and $\mathbf{H}$. Because the magnitude of M and H as well as their orientations are known, $|\mathbf{H} + \mathbf{M}|$ and thus also $\rho_\perp(B)$, can be calculated. Taken together, the interplay of the two terms on the right side of Eq. 3.1 results in the qualitatively different shape of ρ_{long} for different orientations of the magnetic field (Fig. 3.2).

The ρ_{long} and ρ_{trans} calculated from the SDM model are shown as full lines in Figs. 3.1(a,b) and 3.3. For all orientations ϕ_H of the external magnetic field, the SDM model quantitatively describes the longitudinal resistance observed in experiment. In particular, both the strongly varying magnitude and shape of

the switches observed in ρ_{long} are precisely reproduced in the calculations. This demonstrates that Eqs. 3.1 and 3.2 yield a fully quantitative description of the low-field AMR of $Ga_{1-x}Mn_xAs$ for all orientations ϕ_H of the external magnetic field.

The agreement between the SDM model and the experiment can be tested even further by analyzing magnetoresistance measurements in which the direction of the magnetic field sweep is reversed after the first, but before the second magnetization switch. In this case, for small values of H, $\mathbf{M}$ points along one easy axis in the up sweep and along the other in the down sweep. As a consequence, the magnetoresistance traces for the up and the down sweep are different, as illustrated in Fig. 3.4(a). Again, an excellent agreement between the SDM model and experiment is found, with no adjustable parameters. This agreement confirms our hypothesis that $\rho_\perp(B) \propto -|\mathbf{B}|$, since around $H = 0$, the magnetoresistance only originates from a change in the vectorial sum $\mu_0 (\mathbf{H} + \mathbf{M})$.

3.5 Microscopic origin of negative magnetoresistance

We now briefly discuss the microscopic origin of the experimentally observed B-dependence of $\rho_\perp$ (as well as of $\rho_\parallel$, since $\rho_\perp - \rho_\parallel = \text{const.}$). Recent investigations of the resistance temperature dependence[11] have demonstrated the importance of magneto-impurity scattering in $Ga_{1-x}Mn_xAs$. The magneto-impurity scattering model[12, 13] predicts that the spin-dependent scattering at magnetic impurities can result in a negative magnetoresistance of the form $\rho(B) = a - bB + cB^{3/2}$. We find that this functional dependence correctly describes our experimental data not only in the linear regime that we have discussed here extensively, but also for higher field values, where a non-linear dependence is experimentally visible (see Fig. 3.4(b)). Whereas other intrinsic magnetoresistance mechanisms[8,14-17] cannot be ruled out at this stage, our findings provide further support for the relevance of magneto-impurity scattering in $Ga_{1-x}Mn_xAs$. In this regard, it is useful to emphasize that the quantitative understanding of anisotropic magnetoresistance reached in our work makes it possible to separate the magnetization-related AMR from the intrinsic magnetoresistance ($\rho_\parallel, \rho_\perp$), thus enabling a detailed study of the latter.

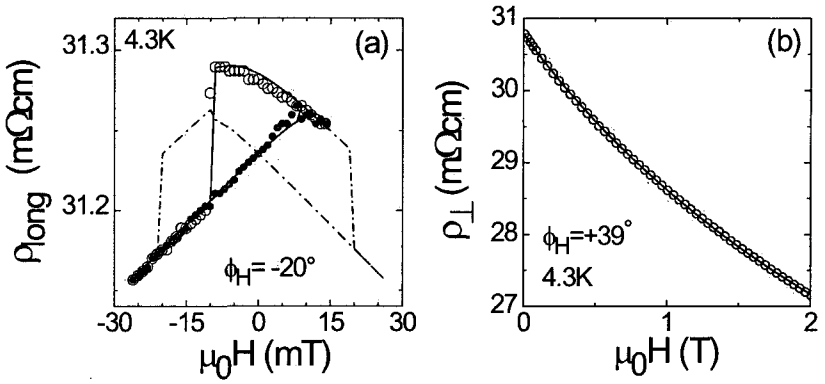

Figure 3.4: (a) Longitudinal magnetoresistance measured ramping up (full circles) and down (open circles) the magnetic field, reverting the sweep direction at 15 mT, i.e., in between the two switches of the magnetization orientation. The full line is calculated theoretically using Eq. 3.1 of the SDM model, without any adjustable parameters (all parameters are fixed by the previous analysis). The dash-dotted line illustrates the magnetoresistance obtained if the field sweep direction is reversed after the second switch of the magnetization orientation (see also Fig. 3.1(a)). (b) The magnetic field dependence of $\rho_\perp$ measured experimentally (open symbols) is reproduced by the magneto-impurity scattering model prosed by Nagaev (full line) over a broad range of magnetic fields.

3.6 Conclusions

In summary, we have investigated experimentally the longitudinal and transverse magnetoresistance in a single ferromagnetic domain of $Ga_{1-x}Mn_xAs$ and performed a comprehensive theoretical analysis of the experimental results. We find that, by taking into account the intrinsic dependence of the resistivity on the magnetic induction, excellent quantitative agreement between experiments and theory is obtained. Our results provide the first detailed and fully quantitative validation of the theory for magnetotransport through a single ferromagnetic domain. In addition, our analysis indicates the relevance of magneto-impurity scattering in $Ga_{1-x}Mn_xAs$.

Bibliography

[1] T. R. McGuire and R. I. Potter, IEEE Trans. Magn. **MAG-11**, 1018 (1975).

[2] J. -P. Jan, in *Solid State Physics*, edited by F. Seitz and D. Turnbull (Academic Press, New York, 1957), vol. 5, pp. 1-96.

[3] H. X. Tang, R. K. Kawakami, D. D. Awschalom and M. L. Roukes, Phys. Rev. Lett. **90**, 107201 (2003).

[4] U. Welp, V. K. Vlasko-Vlasov, X. Liu, J. K. Furdyna, and T. Wojtowicz, Phys. Rev. Lett. **90**, 167206 (2003).

[5] K. Hamaya, T. Taniyama, Y. Kitamoto, R. Moriya, and H. Munekata, J. Appl. Phys. **94**, 7657 (2003).

[6] R. P. Cowburn, S. J. Gray, and J. A. C. Bland, Phys. Rev. Lett. **79**, 4018 (1997).

[7] H. X. Tang, S. Masmanidis, R. K. Kawakami, D. D. Awschalom, and M. L. Roukes, Nature **431**, 52 (2004).

[8] A. Van Esch, L. Van Bockstal, J. De Boeck, G. Ver- banck, A. van Steenbergen, P. Wellmann, B. Grietens, R. Bogaerts, F. Herlach, and G. Borghs, Phys. Rev. B **56**, 13103 (1997).

[9] P. A. Korzhavyi, I. A. Abrikosov, E. A. Smirnova, L. Bergqvist, P. Mohn, R. Mathieu, P. Svedlindh, J. Sad- owski, E. I. Isaev, Y. K. Vekilov, et al., Phys. Rev. Lett. **88**, 187202 (2002).

[10] K. Y. Wang, K. W. Edmonds, R. P. Campion, B. L. Gal- lagher, N. R. S. Farley, C. T. Foxon, M. Sawicki, P. Bo- guslawski, and T. Dietl, J. Appl. Phys. **95**, 6512 (2004).

[11] S. U.Yuldashev, Hyunsik Im, V. S. Yalishev, C. S. Park, T. W. Kang, S. Lee, Y. Sasaki, X. Liu, and J. K. Furdyna, Appl. Phys. Lett. **82**, 1206 (2003).

[12] E. L. Nagaev, Physics Reports **346**, 387 (2001).

[13] E. L. Nagaev, Phys. Rev. B **58**, 816 (1998).

[14] F. Matsukura, M. Sawicki, T. Dietl, D. Chiba, and H. Ohno, Physica E **21**, 1032 (2004).

[15] I. T. Yoon, T. W. Wand, K. H. Kim, and D. J. Kim, J. Appl. Phys. **95**, 3607 (2004).

[16] T. Dietl, F. Matsukura, H. Ohno, J. Cibert, and D. Fer- rand, in NATO Science Series II: Mathematics, Physics and Chemistry, edited by I. D. Vagner, P. Wyder, and T. Maniv (Springer, Berlin, 2003), vol. 106, p. 197.

[17] F. Matsukura, H. Ohno, A. Shen, and Y. Sugawara, Phys. Rev. B **57**, R2037 (1998).

Chapter 4

Correlation effects in the density of states of annealed GaMnAs

The results presented in this Chapter have been published as S. Russo, T.M. Klapwijk,W. Schoch and W. Limmer, *Phys. Rev. B* **75**, 033308 (2007).

4.1 Introduction

We report on an experimental study of low temperature tunnelling in hybrid NbTiN/GaMnAs structures. The conductance measurements display a $\sqrt{V}$ dependence, consistent with the opening of a correlation gap (Δ_C) in the density of states of $Ga_{1-x}Mn_xAs$. Our experiment shows that low temperature annealing is a direct empirical tool that modifies the correlation gap and thus the electron-electron interaction. Consistent with previous results on boron-doped silicon we find, as a function of voltage, a transition across the phase boundary delimiting the direct and exchange correlation regime.

4.2 Phase transition in electron-correlated materials

The new class of ferromagnetic semiconductors $Ga_{1-x}Mn_xAs$ is known[1] to display a metal-insulator transition (MIT) as function of Mn doping. In conventional doped semiconductors the MIT, which occurs as a function of carrier density, is widely studied and considered to be a prime example of a quantum phase transitions. It is understood that the spatial localization of charge carriers, which drives the MIT, reduces the ability of the system to screen charges, leading to a prominent role of the electron-electron interactions. The experimental trace of the Coulomb interactions between the electrons is the depletion of the single-particle Density of States (DOS) $N(E)$ at the Fermi energy [2-9]. For a dirty three dimensional system it is found that $N(E) \sim \sqrt{E}$ in the metallic regime[3, 4], whereas $N(E) \sim E^2$ in the insulating regime[2], recently observed in different localized systems[5-7], including magnetically doped materials[8].

Recently, using conductance measurements across the metal-insulator-transition Lee[9] constructed the phase diagram shown in Fig. 4.1a. At low enough temperatures, 10mK, the energy is controlled by the voltage at which the differential conductance is measured. For low energies, *i.e.* very close to the Fermi energy where the theory for the MIT is valid the system is a Coulomb gap insulator below the critical density and a correlated metal above the critical density. For higher energies a mixed state develops around the critical density, in which the density of states on both sides of the transition have a common functional dependence on energies masking the existence of a critical density. The "pure" state at low densities is the regime where exchange correlations describe the Coulomb interactions, whereas above the critical density the direct Coulomb interactions rule. At low energies the DOS is clearly distinct for metallic and insulating sam-

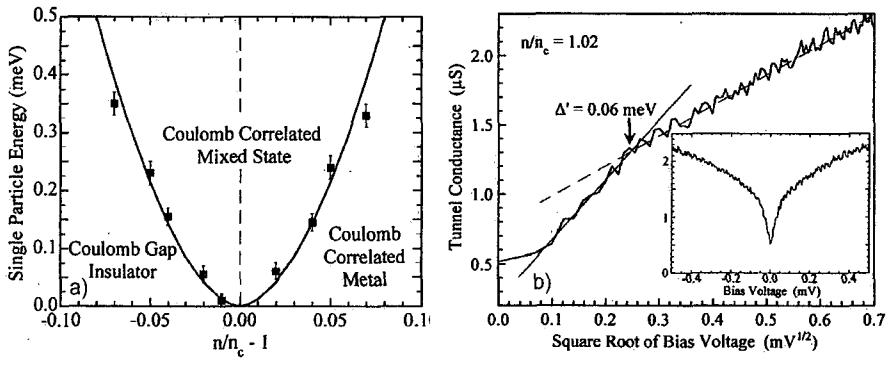

Figure 4.1: a) Phase-diagram proposed by Lee [9] to indicate the electron-correlated regimes at low energies and high energies as a function of carrier density. b) In the inset conductance *versus* voltage bias for our NbTiN/GaMnAs devices. Gray gradient in the background highlights the transition across the phase boundary delimiting direct and exchange correlation regime. At low bias the superconducting gap of the contact material causes a deviation.

ples and the system is in the "pure" state. At high energies the insulating and metallic states are indistinguishable from DOS-measurements.

The new material system GaMnAs is for low Mn doping an insulator and the resistivity diverges for $T \rightarrow 0$, indicating localization effects. In the metallic regime this (III,V)Mn is characterized by a decreasing resistivity which eventually saturates for $T \rightarrow 0$, although these resistivity values remain relatively high ($\sim 10^{-3}$ Ωcm, see Fig. 4.5(c)). Thus GaMnAs is a dirty metal where disorder plays a rather strong role. These strong electron-electron interaction effects the DOS of GaMnAs[10] and might lead to the observation of the phase boundary cross-over from direct to exchange correlation at much higher temperatures than for Si:B.

Here we report the observation of the correlation gap in GaMnAs as measured with a tunnel contact between GaMnAs and the superconductor NbTiN. At the interface we have a Schottky barrier, which at low temperatures acts as a tunnel contact, allowing a direct measurement of the density of states. Superconducting leads are chosen, on top of unpatterned GaMnAs (inset Fig. 4.2), to ensure that the tunnel junction resistances are at least an order of magnitude larger than the sample resistance. The T-shape is chosen to minimize the effect of parallel conductance paths. With these samples we study systematically the evolution of the correlation energy (Δ_C) on the annealing time. We find experimentally that Δ_C decreases monotonously with annealing. This behavior suggests that with

annealing the surface of the GaMnAs is driven away from the metallic towards the insulating state. Furthermore, measurements at bias voltage higher than Δ_C lead to the observation of a cross-over from the *direct* correlation regime to the *mixed* state behavior (as in Fig. 4.1b), consistent with previous results obtained on Si:B[9].

4.3 Superconductor-GaMnAs interface

The $Ga_{1-x}Mn_xAs$ samples (Mn-content of 4.4%) are grown on (001) semi-insulating GaAs substrates by low temperature molecular-beam epitaxy (MBE) at 230°C. The GaMnAs epilayer (thickness of 40 nm, $T_C = 64K$) is patterned to hold two independent devices: a Hall bar and the T-shaped tunnel-contacts. The Hall bar (200×50 μm^2, see inset of Fig. 4.3a) allows the characterization of the magnetic properties of GaMnAs. Electron Beam Lithography (EBL), Ar RF sputter cleaning and reactive sputtering are used to define the top NbTiN (thickness = 30 nm, superconducting transition temperature $T_C^S = 15$ K and superconducting gap $\Delta_S = 2mV$). The contacts on the GaMnAs have a separation of 100 nm and a total area of 0.5×1 μm^2 (see Inset of Fig. 4.2). The tunnel-devices are used to measure the differential resistance.
In the standard tunneling model [11], the tunneling conductance $G(V,T) = \partial I/\partial V$ is the product of the density of states in the interacting material, $N_F(E)$, with the density of states of the superconductor, $N_S(E)$, convoluted with the Fermi-distribution (see Eq. 2.9). In view of the relevant energies we can ignore the thermal smearing. $N_S(E)$ is given by the standard BCS density of states as usually modified by a broadening parameter Γ[12]: $N_S(E) = N(0)Re[\frac{(E-i\Gamma)}{(\sqrt{(E-i\Gamma)^2-\Delta_S{}^2})}]$. The GaMnAs is described as dirty 3D metal system[3, 4], thus $N_F(E) = N(0)(1+\sqrt{(E)/(\Delta_C)})$. Δ_C is the correlation gap which represents the strength of the electron-electron interaction in the ferromagnetic semiconductor. In this tunneling description there are two free parameters, Γ and Δ_C, while the other parameters are known independently.

For temperatures above the T_C the conductance displays a parabolic dependence on bias voltage[10] (see Fig. 4.2). At lower temperatures deviations from the parabolic behavior occur (see inset in Fig. 4.2) which reflect, as we will show, the correlation gap. We focus now on the 2-probe conductance through the SFS device for $T > T_C$, Fig. 4.2. It is apparent that G clearly displays a parabolic dependence on bias voltage, which demonstrates that tunnelling is taking place, as described by Brinkman, Dynes and Rowell (BDR)[13] . The measured con-

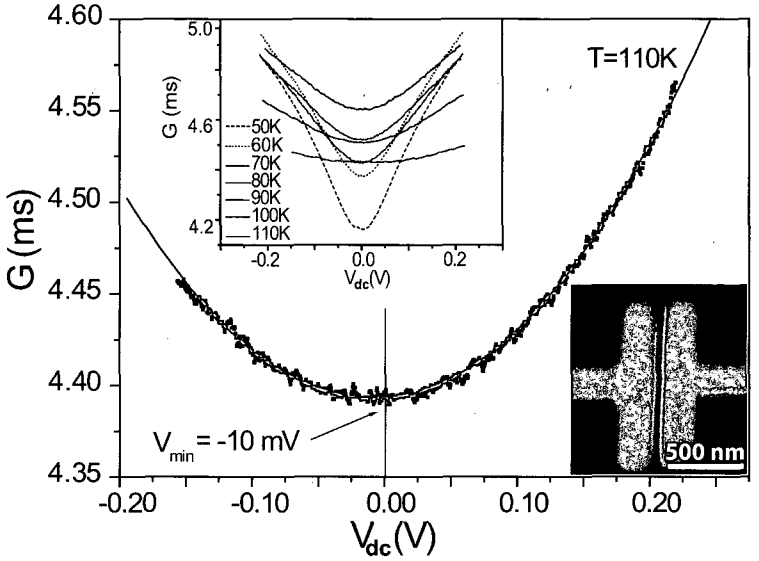

Figure 4.2: Central inset: measurements at different temperatures of G *versus* V after annealing a device for 120 min and having a T_C of 96K. Lower inset: a micrograph of one of the nano-fabricated SFS samples. The main figure shows a conductance measurement at T=110K. The full line is a best fit to the BDR model[13], used to determine the barrier height.

ductance for $T > T_C$ shows a slightly asymmetric shape and the occurrence of a minimum at a finite voltage bias ($V_{min} = -10mV$). These two features in the measurements are typical for the tunnel conductance in metal-insulator-metal junctions with different barrier heights at the interfaces.
In applying the BDR model to our data to estimate the barrier height at the SF interface, we assume that the conduction in the GaMnAs is mainly due to the heavy holes with an effective mass of $0.462m_0$ [14]. In addition we assume a thickness of the barrier at SF of 10Å[15]. From fitting the curve of $G(V)$ to the BDR model, continuous line in Fig. 4.2, we find that the mean barrier height is $\overline{\varphi} = 0.33V$. Furthermore the bias voltage at which the minimum conductance occurs ($V_{min} = -10mV$) gives a difference in barrier heights at the SF interface of $\Delta\varphi = 16mV$. Finally, we emphasize that the measured resistance of the two tunnel contacts in series is much higher than the resistance of the GaMnAs in between. These facts lead us to conclude that it is reasonable to assume that the measured conductance is a tunnel conductance.

4.4 Role of annealing on the ferromagnetic properties of GaMnAs

Previous experiments have demonstrated that low temperature post growth annealing offers the possibility to change the ferromagnetic properties of GaMnAs[17]. Our samples are annealed in the same way, but performed on fully processed structure with the NbTiN on top of the GaMnAs. This leaves the interface unexposed to air. We do not observe any change in the critical current of the NbTiN, which excludes possible degradation of the superconductor. The annealing is performed at 200°C on a hot plate in air [18] for a sequence of annealing times up to 180 min. In Fig. 4.3 we present measurements of the sheet resistance *versus* temperature performed on the Hall bar for different annealing times. The resistance displays a non monotonous dependence on temperature. It reaches a maximum at the Curie temperature[1] and eventually decreases, for $T < T_C$, as expected for metallic samples.
From the graph of T_C *versus* annealing time (Fig. 4.3b) it is apparent that T_C increases[19]. It remains basically unchanged for further annealing to 180min. which is consistent with more extensive work presented by Stanciu *et al.*[16]. This enhancement of T_C has been usually traced back to a removal of compensating defects, and thus, to an increase of the hole concentration[17, 20]. In fact channeling Rutherford backscattering[17] and Auger[20] experiments have shown that annealing at low temperature causes a migration of Mn interstitial defects towards the surface of GaMnAs. The fact that bulk ferromagnetic properties improve with low temperature annealing is also evident from the room temperature resistivity (ρ_{RT}), see Fig. 4.3c. ρ_{RT} decreases monotonously with annealing time, confirming that a reduction of defects and an increase of charge density takes place in GaMnAs[18].

4.5 The correlation gap in the DOS of GaMnAs

The 2-probe tunnel conductance measured at 4.2K is shown in Fig. 4.5a. The measurements are normalized to the conductance value at 0.015V (arbitrarily chosen) and shifted for clarity. For $V < \Delta_{NbTiN}$ the superconducting state of the leads dominate the data. However for $V > \Delta_{NbTiN}$ correlation effects

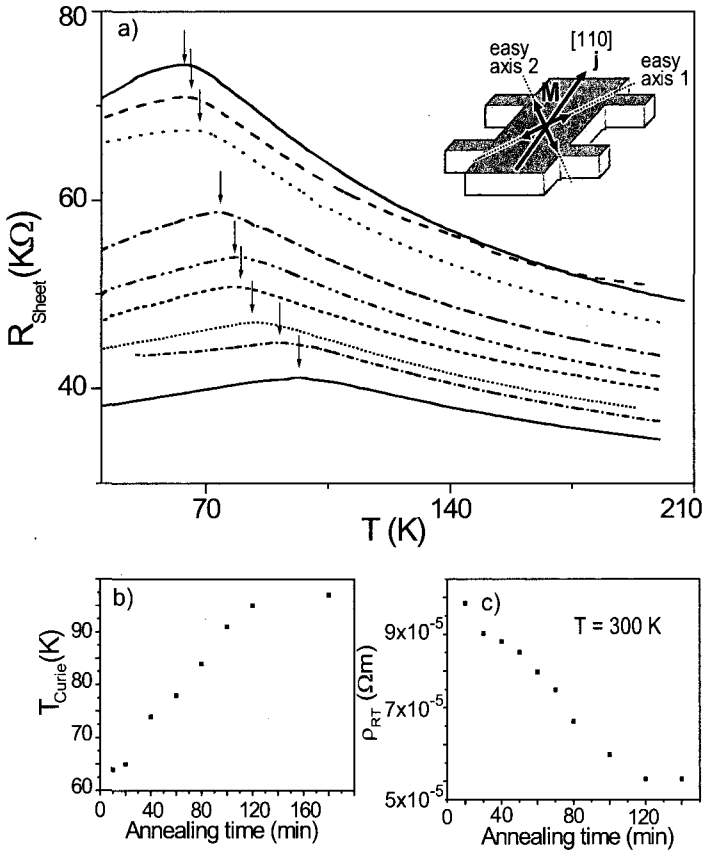

Figure 4.3: a) Plot of the sheet resistance versus temperature for a GaMnAs Hall bar device, e.g. inset. Different curves are for different annealing times, from top to bottom: 0, 10, 20, 40, 60, 80, 100, 120, and 180 min. T_C is highlighted by the arrows. b) The T_C increases linearly with annealing time up to 120 min. and it remains unchanged for further annealing to 180min. c) The room temperature resistivity decreases as function of annealing time.

play the major role in transport and the measured conductance displays a non-linear character with the expected $\sqrt{V}$ dependence on the bias voltage. This $\sqrt{V}$ behavior indicates that the GaMnAs acts as a three dimensional dirty metal, with correlation effects parameterized with correlation gap Δ_C. We find experimentally that the non linear character of the conductance curves is progressively reduced as a function of increased annealing time. The continuous lines in Fig.

4.5a are the best fit to the tunneling model. Standard non-linear fitting is used with the parameters Δ_C and Γ, and minimization of the χ^2 merit function is carried out according to the Levenberg-Marquardt method. Good agreement between theory and experiments is found, and for each different annealing time the corresponding value of Δ_C is extracted (see Fig. 4.5b); the values found for Γ are 1 ± 0.2mV.

We observe that the interaction parameter in the as grown sample is $\Delta_C = 278$

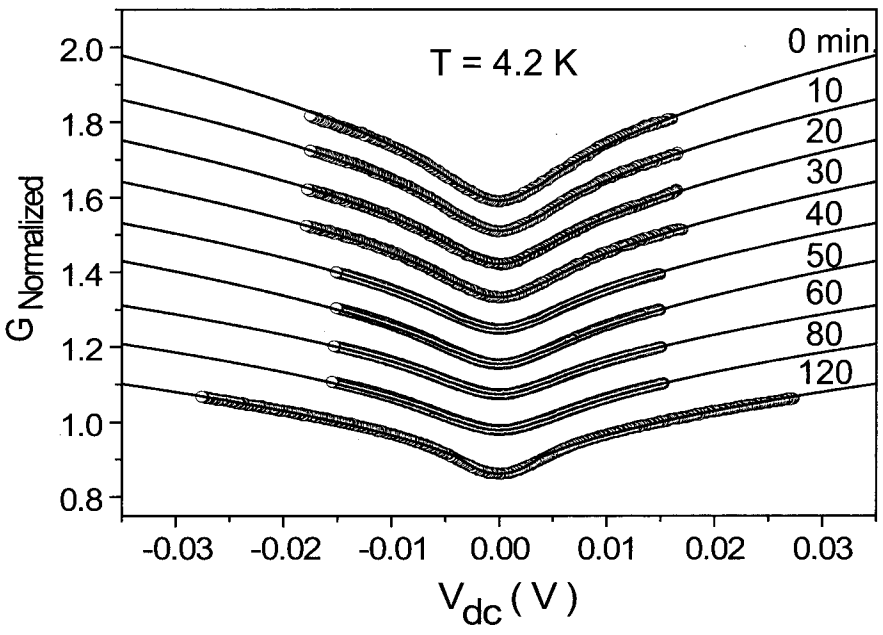

Figure 4.4: 2-Probe tunnel conductance measurements for different low-temperature annealing times (shown for each graph). For increasing annealing time the non linear character of the curves at high bias is reduced. The solid lines are fits, leading to the correlation gap Δ_C.

mV[21] and it reduces to a smallest value of 59mV by annealing the sample for 120 minutes, see Fig. 4.5b. As shown in Fig. 4.3 annealing leads to an increase in T_C (from 64K to 97K) and a decrease in ρ_{RT} by 48 %, which suggests an improvement in the quality of material. However, the tunneling measurements lead to the conclusion that the correlation gap becomes smaller indicative of a system which is driven from the metallic regime to a more insulating regime. This behavior is consistent with the fact that with increasing annealing time a

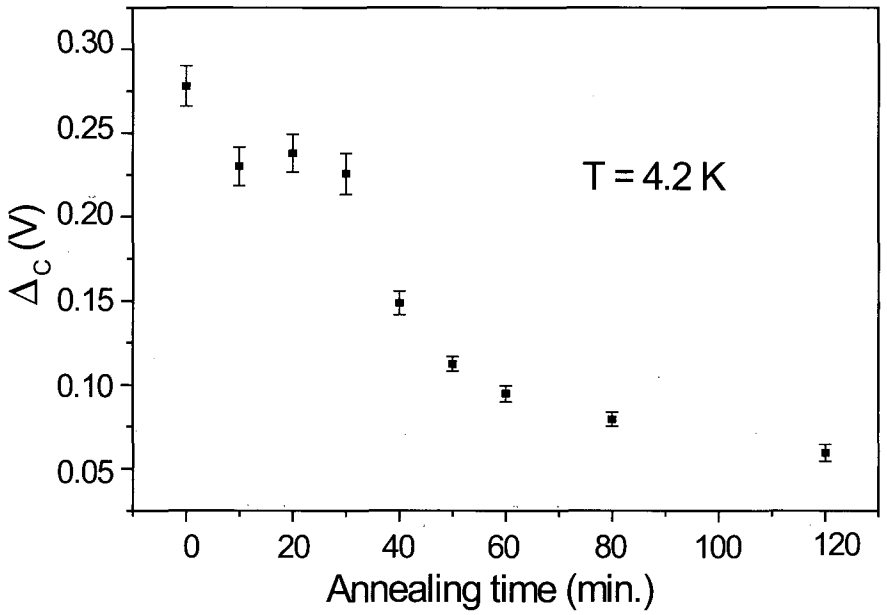

Figure 4.5: Δ_C resulting from the fit of 2-Probe tunnel conductance measurements for different low-temperature annealing times. It appears that Δ_C decreases monotonously with annealing time.

larger number of compensating defects reaches the surface, causing an increase in resistivity and a reduction of the correlation energy. Thus low temperature annealing, while improving the ferromagnetic properties of the bulk material (see Fig. 4.2), drives the surface of GaMnAs from the metallic towards the insulating state.

We now turn to the tunnel conductance measurements at higher bias voltage, higher than the correlation gap ($V_{bias} > \Delta_C$, e.g. inset Fig. 4.6). We focus on a sample annealed for 120 minutes and $\Delta_C = 59$mV. From Fig. 4.1b it is apparent that $G \sim \sqrt{V}$ over the entire bias range but with two different slopes, one at low energy and a less steep one at higher energy. The cross-over between these two regimes occurs at the bias corresponding to the correlation gap. Similar results have been presented by Lee[9], although at much lower energies. Adopting the interpretation of Ref.[9] we conclude that at low energies the GaMnAs is properly described as a dirty metal where correlation effects are manifested in a minimum in the DOS at the Fermi Energy. However, at high energies the $\sqrt{V}$ dependence stems from a mixture of direct and exchange correlations. At

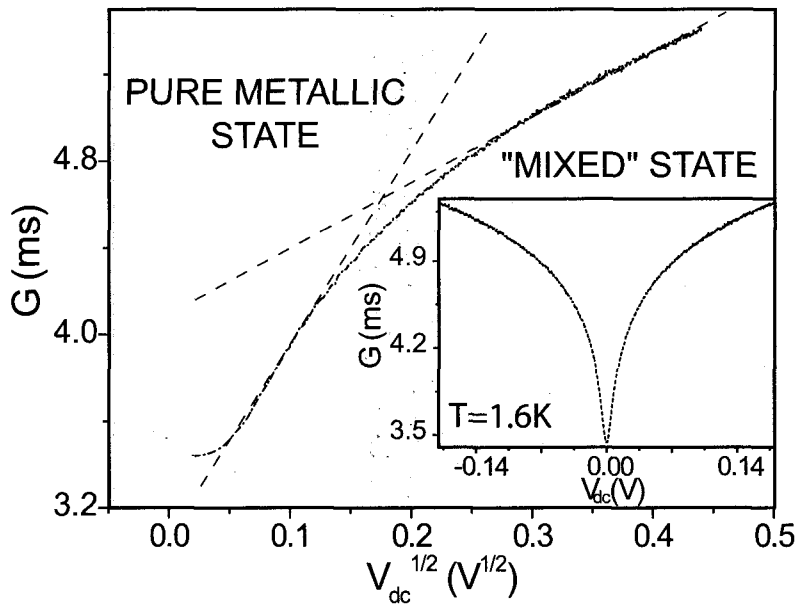

Figure 4.6: In the inset conductance *versus* voltage bias for our NbTiN/GaMnAs devices. Gray gradient in the background highlights the transition across the phase boundary delimiting direct and exchange correlation regime. At low bias the superconducting gap of the contact material causes a deviation.

high energies GaMnAs displays a cross-over to the *mixed* state. The fact that the energy scale of the correlation gap in GaMnAs is much higher than in Si:B allowed the observation of this cross-over at modest temperatures.

4.6 Conclusions

In conclusion, we have studied correlation effects in the density of states of GaMnAs. Low temperature post-processing annealing is found to modify the electron-electron correlation in GaMnAs. Our experiments suggest that annealing acts in opposite ways on the bulk compared to the surface of GaMnAs: while improving the ferromagnetic properties of the bulk it drives the surface from the metallic state towards the insulating state. Hence, we find that annealing is a good external parameter which can be used to monitor continuously the evolution of the correlation gap when approaching the MIT at the surface of GaMnAs. Inter-

estingly the tunnel conductance measurements display a cross-over from a low energy regime to a high energy regime allowing to track the phase boundary separating the pure metallic behavior from the *mixed* state, as found previously in Si:B by Lee[9].

Bibliography

[1] F. Matsukura, H. Ohno, A. Shen and Y. Sugawara, Phys. Rev. B **57**, 2037(R) (1998).

[2] A.L. Efros and B.I.Shklovskii, J. Phys. C **8**, L49 (1975).

[3] B.L. Altshuler adn A.G. Aronov, Solid State Commun. **30**, 115 (1979).

[4] W.L. McMillan, Phys. Rev. Lett. **24**, 2739 (1981).

[5] J.G. Massey and M. Lee, Phys. Rev. Lett. **50**,4266 (1995).

[6] H.B. Chan, P.I. Glicofridis, R.c. Ashoori adn M.R. Melloch, Phys. Rev. Lett. **79** 2867 (1997).

[7] E. Bielejec, J. Ruan and W. Wu, Phys. Rev. Lett. **87**, 036801 (2001).

[8] W. Teizer, F. Hellman and R.C.Dynes, Phys. Rv. Lett. **85**, 848 (2000). L. Bokacheva,W. Teizer, F. Hellman, and R. C. Dynes, Phys. Rev. B **69**, 235111 (2004).

[9] M. Lee, Phys. Rev. Lett. **93**, 256401 (2004).

[10] S.H. Chun, S.J. Potashnik, K.C. Ku, P.Schiffer and N. Samarth, Phys. Rev. B **66** 100408(R) (2002).

[11] See, for example, E.L. Wolf, *Principles of Electron Tunneling Spectroscopy* (Oxford Univ. Press, Oxford, 1985).

[12] R.C. Dynes, V. Narayanamurti and J.P. Garno, Phyis. Rev. Lett. **41**, 1509 (1978).

[13] W.F. Brinkman, R.C. Dynes and J.M. Rowell, Phys. Rev. B, **41** 1915 (1970).

[14] T. Dietl, H. Ohno and F. Matsukura, Phys. Rev. B **63** 195205 (2001).

[15] W. Mönch, Semiconductor Surface and Interfaces, Spinger (2001).

[16] V. Stanciu, O. Wilhelmsson, U. Bexell, M. Adell, J. Sadowski, J. Kanski, P. Warnicke, and P. Svendlidh, Phys. Rev. B **72**, 125324 (2005).

[17] K.M. Yu, W. Walukiewicz, T. Wojtowicz, I. Kuryliszyn, X. Liu, Y. Sasaki and J.K. Furdyna, Phys. Rev. B **65**, 201303(R) (2002).

[18] This particular annealing temperature was chosen because it results in a pronounced increase of T_C on our materials: see W. Limmer, A. Koeder, S. Frank, M. Glunk, W. Schoch, V. Avrutin, K. Zuern, R. Sauer and A. Waag, Physica E **21**, 970-974 (2004).

[19] S. J. Potashnik, K.C. Ku, S.H. Chun, J.J. Berry, N. Samarth and P. Schiffer, Appl. Phys. Lett. **79**, 1495 (2001). K.W. Edmonds, K. Y. Wang, R.P. Campion, A.C. Neumann, N.R.S. Farely, B.L. Gallagher and C.T. Foxon, Appl. Phys. Lett. **81** 4991 (2002).

[20] K.W. Edmonds, P. Boguslawski, K. Y. Wang, R.P. Campion, S.N. Novikov, N.R.S. Farley, B.L. Gallagher, Phys. Rev. Lett. **92**, 037201 (2004).

[21] Similar values of correlation energy where observed in Al granular films with resistivities comparable to our *GaMnAs* film: see G. Hertel, D.J. Bishop, E.G. Spencer, J.M. Rowell and R.C. Dynes, Phys. Rev. Lett. **50**, 743 (1983).

Chapter 5

Experimental evidence of non-local Andreev reflection

The results presented in this Chapter have been published as S. Russo, M. Kroug, T.M. Klapwijk and A.F. Morpurgo, *Phys. Rev. Lett.* **95**, 027002 (2005) and S. Russo, M. Kroug, T. M. Klapwijk, and A. F. Morpurgo AIP Conf. Proc. **850**, 877 (2006).

5.1 Introduction

In this chapter we report transport experiments providing clear evidence for the occurrence of crossed Andreev reflection (or non-local Andreev reflection) and elastic cotunneling through superconducting layers of thickness comparable to the superconducting coherence length. The probability of the two processes is energy dependent, with elastic cotunneling dominating at low energy and non-local Andreev reflection at higher energies. The energy scale of the crossover is found to be the Thouless energy of the superconductor, which indicates the phase coherence of the processes. This results are relevant for the realization of recently proposed entangler devices.

5.2 Experiment

One way to investigate the occurrence of non-local AR relies on the following idea. Two normal metal electrodes are connected via two tunnel barriers (junctions J1 and J2) to one common superconducting electrode. If the separation of J1 and J2 is comparable to the superconducting coherence length ξ, an electron injected at energy $E < \Delta$ from the normal electrode of J1 can propagate as an evanescent wave through the superconductor and pair with an electron in the normal electrode of J2[3]. This process results in a hole "reflected" into the second electrode, i.e. non-local AR. As holes have the opposite charge of electrons, holes undergoing non-local AR generate a voltage difference across J2 that has a sign opposite to that observed when the superconductor is in the normal state ($T > T_c^S$). Therefore, in principle, the detection of non-local AR is straightforward: J1 is used to inject current into the superconductor and J2 is used as a voltage probe to detect a voltage of the correct sign.
In practice, the situation is complicated by the occurrence of a second process competing with non-local AR: electrons injected from J1 can be transmitted into J2 without being converted into holes. This process is known as elastic cotunneling (EC)[4-11], and contributes to generate a voltage across J2 that has the same sign as that observed when the superconductor is in the normal state. Thus, the sign of the voltage measured across J2 depends on whether EC or non-local AR occurs with larger probability. The voltage measured at J2 may also vanish, if cotunneling and non-local AR occur with exactly the same probability for all energies of the injected electrons. As some recent calculations predict[4-11] that this could in fact happen, it is not possible to anticipate which signal -if any- will be measured experimentally. For instance, in a recent experiment in which two ferromagnetic leads were used as normal electrodes, only the sign corresponding

Chapter 5

Experimental evidence of non-local Andreev reflection

The results presented in this Chapter have been published as S. Russo, M. Kroug, T.M. Klapwijk and A.F. Morpurgo, *Phys. Rev. Lett.* **95**, 027002 (2005) and S. Russo, M. Kroug, T. M. Klapwijk, and A. F. Morpurgo AIP Conf. Proc. **850**, 877 (2006).

5.1 Introduction

In this chapter we report transport experiments providing clear evidence for the occurrence of crossed Andreev reflection (or non-local Andreev reflection) and elastic cotunneling through superconducting layers of thickness comparable to the superconducting coherence length. The probability of the two processes is energy dependent, with elastic cotunneling dominating at low energy and non-local Andreev reflection at higher energies. The energy scale of the crossover is found to be the Thouless energy of the superconductor, which indicates the phase coherence of the processes. This results are relevant for the realization of recently proposed entangler devices.

5.2 Experiment

One way to investigate the occurrence of non-local AR relies on the following idea. Two normal metal electrodes are connected via two tunnel barriers (junctions J1 and J2) to one common superconducting electrode. If the separation of J1 and J2 is comparable to the superconducting coherence length ξ, an electron injected at energy $E < \Delta$ from the normal electrode of J1 can propagate as an evanescent wave through the superconductor and pair with an electron in the normal electrode of J2[3]. This process results in a hole "reflected" into the second electrode, i.e. non-local AR. As holes have the opposite charge of electrons, holes undergoing non-local AR generate a voltage difference across J2 that has a sign opposite to that observed when the superconductor is in the normal state ($T > T_c^S$). Therefore, in principle, the detection of non-local AR is straightforward: J1 is used to inject current into the superconductor and J2 is used as a voltage probe to detect a voltage of the correct sign.
In practice, the situation is complicated by the occurrence of a second process competing with non-local AR: electrons injected from J1 can be transmitted into J2 without being converted into holes. This process is known as elastic cotunneling (EC)[4-11], and contributes to generate a voltage across J2 that has the same sign as that observed when the superconductor is in the normal state. Thus, the sign of the voltage measured across J2 depends on whether EC or non-local AR occurs with larger probability. The voltage measured at J2 may also vanish, if cotunneling and non-local AR occur with exactly the same probability for all energies of the injected electrons. As some recent calculations predict[4-11] that this could in fact happen, it is not possible to anticipate which signal -if any- will be measured experimentally. For instance, in a recent experiment in which two ferromagnetic leads were used as normal electrodes, only the sign corresponding

to EC has been observed[12].

In this chapter we report a clear experimental evidence for both non-local AR

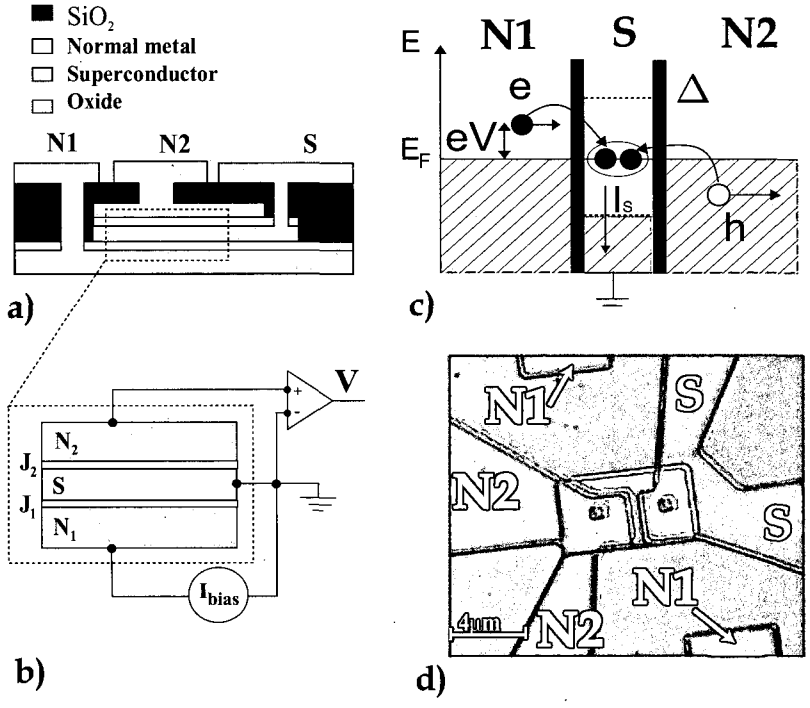

Figure 5.1: a) Schematic cross-section of our sample (not to scale). Two normal electrodes (N1 and N2) are connected to a superconducting layer (S) via two tunnel barriers (J1 and J2), whose separation d is defined by the thickness of the superconducting layer. The concept of the measurement configuration is shown in b): current is injected through J1 and the non-local voltage is measured across J2. c) illustrates the non-local AR process: an incoming electron from N1 is transmitted as a hole into N2 while a Cooper pair condenses in S. d) Optical microscope image of one of our samples (top view). The rectangle in the center is where J1 and J2 are located; N1, N2 and S label the electrical contacts to the respective metallic layers.

and elastic cotunneling using the experimental strategy just outlined. We find that the magnitude and the sign of the measured non-local voltage depend on the bias across the injecting junction. At low bias, the observed sign is the same as when the superconductor is in the normal state, indicating that EC dominates. At higher bias the sign of the voltage is reversed, which strongly suggests the oc-

currence of non-local AR. The energy scale on which the sign-reversal takes place is comparable to the Thouless energy of the superconducting layer[16], indicating that the sub-gap microscopic processes of conduction, non-local AR and EC, are phase-coherent.

A schematic representation of the devices used in our experiments is shown in

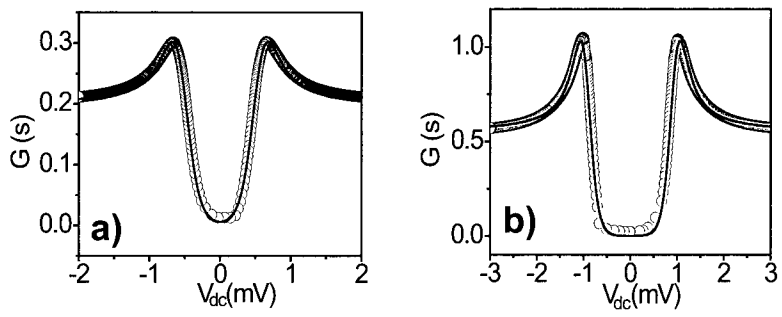

Figure 5.2: a) and b) show the tunnelling characteristics of junctions, measured in two devices with $d = 15$ and 50 nm respectively. The solid line is a fit based on the BCS density of states and shows that good agreement is found with $\Delta = 0.9$ and 1.45mV for the two different thicknesses of the Nb layer[19]. The suppression of the gap in the $d = 15$ nm sample is typical of these thin superconducting films[18].

Fig. 5.1a. The structure is implemented in a Nb/Al multilayer sputtered on a thermally oxidized Si substrate using conventional Nb/Al technology[17]. The multilayer consists of two normal metal layers (N1 and N2, 50nm Al layers) connected via two tunnel barriers to one common superconductor (S). Junction J1 is obtained by *in-situ* oxidation of the N1 layer and subsequent deposition of Nb. Next, a thin ($\sim$ 5 nm) Al layer is sputtered on top of the Nb and oxidized *in-situ*. Finally the top Al layer (N2) is deposited to form junction J2.

The fabrication process used to pattern the multilayer relies on conventional photolithography combined with chlorine-based reactive ion etching. The junctions area is approximately $4 \times 8\ \mu m^2$. Independent electrical connections to the three layers are formed by deposition of a 200 nm thick Al/Nb layer on a SiO_2 mask followed by dry etching. We have checked the quality of the tunnel junctions by fitting the differential conductance with the usual BCS theory and found that the tunnelling characteristics of junctions J1 and J2 do not show any substantial difference, see Fig.5.2. This indicates that the superconducting properties of the Nb/Al layer (S) are uniform across its thickness.

In our devices the separation between the two tunnel barriers is determined by

the thickness of the S layer, which can be controlled on the nanometer scale. This is crucial, since the separation of the tunnel barrier has to be comparable to the superconducting coherence length in S, $\xi \simeq \sqrt{\xi_0 l_e} = 10 - 15$ nm [18] (where $l_e = 3D/v_f \simeq 2$ nm is the elastic mean free path, the diffusion constant $D = 1.6\ cm^2/s$ and $\xi_0 = \hbar v_F/\pi\Delta$). An optical microscope image of one of our devices is shown in Fig.5.1d.

5.3 Direct measure of non-local Andreev reflection

All the measurements were performed at $T = 1.6$ K or higher, with the aluminum electrodes N1 and N2 in the normal state ($T_C^{Al} \simeq 1.2$ K). The measurements scheme employed to address the occurrence of non-local Andreev reflection in the experiment is shown in Fig.5.1b). A current I is fed through one of the junctions (e.g., J1) while the non-local voltage V^{nl} is measured across the other junction (J2), the superconductor is maintained at ground. The current bias has a *dc* component and an *ac* modulation with an amplitude of 1μA at 19.3Hz, and a lock-in technique is used to measure the *ac* component of the non-local signal. This corresponds to measuring the contribution given to the non-local voltage by only those electrons which have an energy $E = eV_{dc}$, where V_{dc} is the *dc* voltage across J1.

Fig. 5.3 shows the V_{ac}^{nl} measured at 1.6 K as a function of V_{dc}, for a sample in which the superconducting layer is 15 nm thick, approximately equal to ξ. A non-local voltage is clearly visible, which reverses its sign at $V_{dc} = 270\mu$V and eventually vanishes at $V_{dc} \simeq 700\ \mu$V, thus on a bias range much smaller than the superconducting gap (0.9 meV, see Fig. 5.4b). The figure also shows the (much larger) non-local signal measured at $T = 22.5$ K $> T_c^S$.

To investigate if the signal originates from evanescent waves propagating below the superconducting gap, we have measured the non-local voltage in samples with different thickness d of the superconducting layer. Fig. 5.4 compares the data measured in three samples where $d = 15$, 50, and 200 nm, respectively. For the 50 nm sample, a non-local signal reversing sign with increasing *dc* bias is still visible at a bias range much smaller than the superconducting gap. However, the magnitude of the signal is approximately 20 times smaller than for the sample with $d = 15$ nm. For the sample with a 200 nm thick superconducting layer, no non-local signal is observed. These observations indicate that V_{ac}^{nl} is very rapidly suppressed with increasing the thickness of the superconductor, as expected for

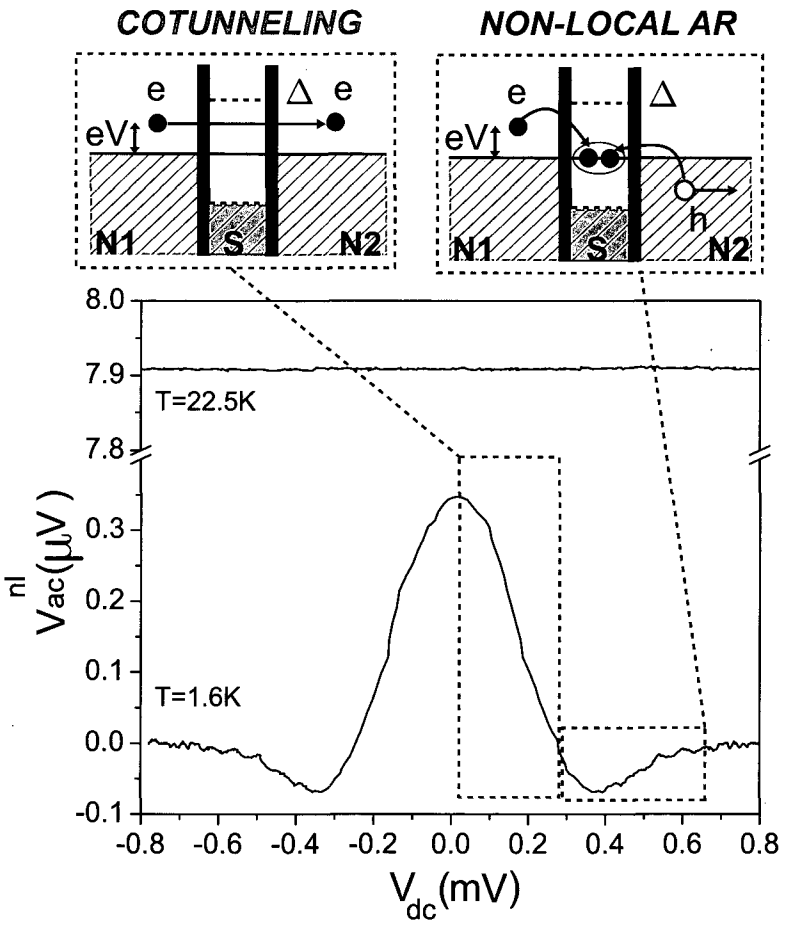

Figure 5.3: The non-local voltage V_{ac}^{nl} measured across J2, on a device with a $d = 15$ nm thickness of the superconducting layer, for two different temperatures. The upper curve is measured at $T = 22.5$ K -well above T_c^S- and shows a bias-independent non-local voltage due to electrons. At $1.6K$ (below T_c^S), the non-local voltage is much smaller and depends on the bias V_{dc} across J1. At low bias, $V_{ac}^{n}l$ has the same sign measured in the normal state, indicating that elastic cotunnelling dominates. At higher bias, the sign of $V_{ac}^{n}l$ is reversed, which indicates the occurrence of non-local AR.

evanescent waves.

The comparison of different samples additionally shows that the energy scale on which the non-local signal reverses its sign (and eventually disappears) becomes

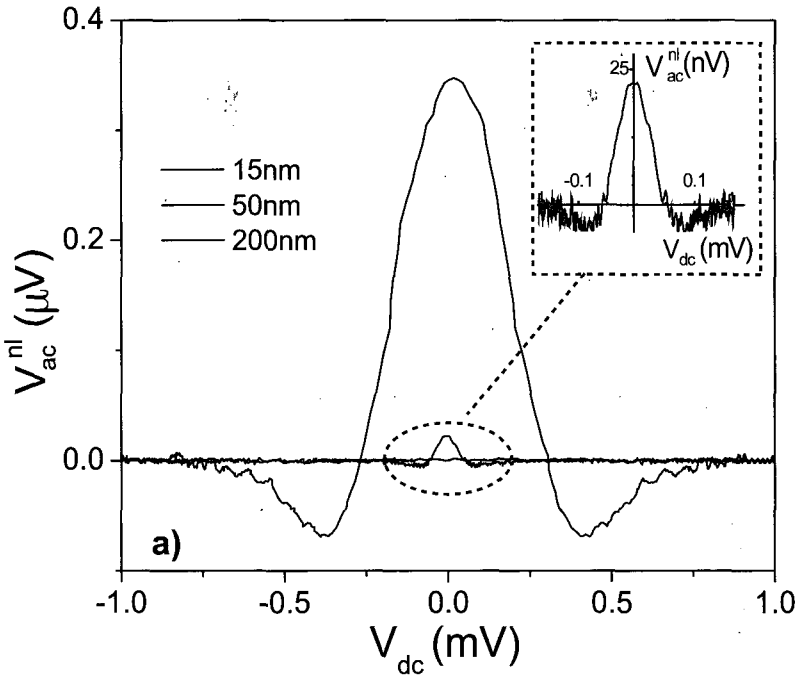

Figure 5.4: (a) Non-local voltage V_{ac}^{nl} measured at $T = 1.6$ K on three samples with different thickness of the superconducting layer ($d = 15,\ 50,\ 200$ nm, with a normal state resistance of 4.8, 1.7, and 0.9 Ω respectively). Panels

smaller for a larger separation of the tunnel barriers. For the $d = 15$ nm sample the zero crossing energy is $\simeq 300\ \mu$eV and for the $d = 50$ nm it is $\simeq 50\ \mu$eV (see Fig. 5.4). These values correspond well to the Thouless energy $E_T = \hbar D/d^2$ of the superconducting layers, equal to $E_T \simeq 450\ \mu$V and to $E_T \simeq 45\ \mu$V for the $d = 15$ nm and the $d = 50$ respectively. The fact that the Thouless energy determines the behavior of V_{ac}^{nl}, indicates that the signal originates from quantum-mechanically phase coherent processes. This is to be expected, since the transit time τ_{tr} of electrons injected from J1 and transmitted into J2 -as electrons or holes- is $\tau_{tr} \simeq d^2/D \simeq 1 - 10$ ps, much smaller than the inelastic electron-phonon ($\tau_{ph} \simeq 1$ ns at 1 K in Nb) and electron-electron ($\tau_{ee} \simeq 0.1$ ns) interaction times[20].

Finding that E_T is the relevant energy scale in our measurements also gives an indication that non-equilibrium effects[21] in the superconductor do not play a relevant role. In fact, these effects depend on the quasiparticle injection rate

and relaxation times, whose energy dependence is not strongly influenced by phase coherent propagation in the superconductor (and thus by E_T). Note also that non-equilibrium effect normally become more relevant at higher bias voltage (when the amount of injected charge is larger), whereas the amplitude of the signal V_{ac}^{nl} is maximum at $V_{dc} = 0$ V and vanishes for V_{dc} well below the gap. The absence of non-equilibrium is consistent with the low transparency of our tunnel barriers ($T \approx 10^{-5}$) and with the fact that at low V_{dc} quasiparticles are injected well below the superconducting gap. Contrary to quasiparticles occupying states above Δ, which may have very long relaxation times, quasiparticles with $E < \Delta$ decay very rapidly on the scale of h/Δ. These considerations are important because complex non-equilibrium effects might be invoked as an explanation for the appearance of the signal V_{ac}^{nl}.

We conclude that the measured non-local voltage V_{ac}^{nl} is due to phase coherent elastic cotunneling and non-local AR. EC is predominant at low bias whereas non-local AR dominates at higher bias, where the sign of V_{ac}^{nl} is negative. That the effect is large and present in all samples (approximately 10 samples with d=15nm and 50nm have been studied) demonstrates that the sign reverse in the non-local voltage is not just a sample-specific effect, as has been observed in InAs/Nb structures[22].

5.4 Temperature and Magnetic field dependence

The measured temperature and magnetic field dependence of V_{ac}^{nl} (see Fig. 5.5) seems to be consistent with this interpretation. V_{ac}^{nl} increases with lowering T similarly to what one would expect from the convolution of a thermally smeared Fermi distribution with an energy dependent transmission probability (and excluding the possibility that the signal is due to quasiparticle propagating above the gap). The signal is suppressed by an in-plane magnetic field of $B \simeq 0.5$ T, which is much smaller than the critical field (higher than 6 T[24]). We believe that this is because the field can penetrate in the superconductor (the magnetic penetration length in Nb is larger than d) and affect quantum interference by breaking time reversal symmetry. Note, however, that at 0.5 T the magnetic flux enclosed by typical electron-hole trajectories traversing the superconductors is only approximately $0.1 \times \phi_0$, so that the specific mechanism responsible for time reversal symmetry breaking remains to be understood in detail.

It is unclear which theoretical model is most suitable for the detailed analysis of our data. Our observation of a non-local signal shows that the cancellation

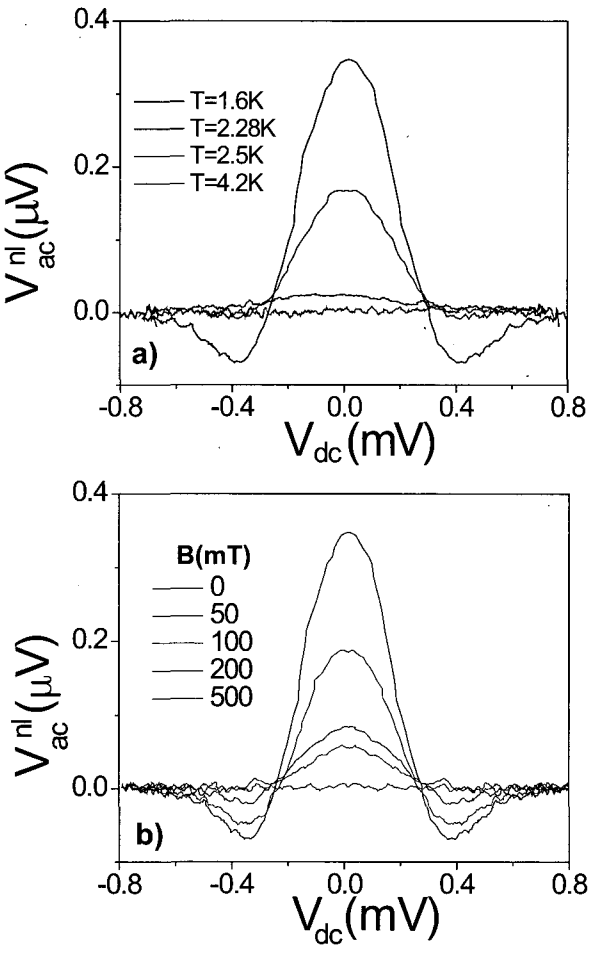

Figure 5.5: (a) Temperature and (b) magnetic field dependence of the non-local voltage V_{ac}^{nl} measured as a function of V_{dc}, on a sample with $d = 15$ nm.

of the contribution to V_{ac}^{nl} due to non-local AR and EC does not occur in the samples investigated here. This cancellation was theoretically found in models that neglect the effect of Coulomb interaction[4], whereas calculations made for different systems in which interactions in the leads play a relevant role [5, 7, 9] did all predict the occurrence of visible effects. Since the effect of Coulomb interaction on electronic transport is visible in large-area tunnel junctions of size

comparable to ours[23], we believe that Coulomb interaction may also be relevant here. A quantitative interpretation of our experimental results will require the analysis of theoretical models more sophisticated than those considered until now, which may have to address aspects of our samples that have not been considered so far. Examples are a gradient in the phase of the superconducting order parameter, induced by the current injected into the superconductor, and a small sub-gap density of states induced by the presence of the normal electrodes. In a recent theoretical work by A.L. Yeyati *et al.*[25], it was shown that in a multilayer geometry, such as the one investigated in this experiment, electron interactions mediated by electromagnetic excitations lead to an imbalance between EC and non-local Andreev reflection which is in surprising accordance with the experimental results presented in this Chapter.

5.5 Conclusions

In conclusion, we have reported clear experimental evidence for the occurrence of non-local Andreev reflection and elastic cotunneling through a superconducting layer. The energy of the injected electrons determines which of the two processes occurs with higher probability: elastic cotunneling is the dominant process at low energy whereas non-local Andreev reflection dominates at higher energy. The crossover is found to occur on a scale determined by the Thouless energy of the superconductor which demonstrates the phase coherent nature of the processes. These results are relevant for recent theoretical proposals of quantum entangler devices that aim at injecting into two spatially separated normal metal leads the spin-entangled electrons forming a Cooper pair. In this context, the energy dependence of the probability for non-local Andreev reflection may provide a new way to control the output of these entanglers.

The authors acknowledge discussions with Y. V. Nazarov and P. Samuelsson. This work was financially supported by NWO/FOM and by NOVA. The work of AFM is part of the NWO Vernieuwingsimpuls 2000 program.

Bibliography

[1] A. F. Andreev, Sov. Phys. JETP **19**, 1228 (1964).

[2] J. M. Byers and M. E. Flatté, Phys. Rev. Lett., **74** 306-309 (1995).

[3] G. Deutscher and D. Feinberg, Appl. Phys. Lett., **76**, 487-489 (2000).

[4] G. Falci, D. Feinberg, and F. W. J. Hekking, Europhys. Lett., **54**, (2) 255-261 (2001).

[5] P. Recher, E. V. Sukhorukov and D. Loss, Phys. Rev. B, **63**, 165314 (2001).

[6] N. M. Chtchelkatchev *et al.*, Phys. Rev. B, **66**, 161320 (2002).

[7] C. Bena *et al.*, Phys. Rev. Lett., **89**, 037901 (2002).

[8] P. Samuelsson, E. V. Sukhorukov and M. Buttiker,Phys. Rev. Lett., **91**, 157002 (2003).

[9] P. Recher and D. Loss, Phys. Rev. Lett., **91**, 267003 (2003).

[10] E. Prada and F. Sols, Eur. Phys. J. B, **40**, 379-396 (2004).

[11] G. Bignon *et al.*, Europhys. Lett., **67**, 110-116 (2004).

[12] D. Beckmann, H. B. Weber, and H. v. Lohneysen, Phys. Rev. Lett., **93**, 197003 (2004).

[13] This is a central concept of all the theoretical work referred to above. For particularly detailed discussions see, e.g., Refs. 3,8, and 10.

[14] G. Burkard, D. Loss and E. V. Sukhorukov, Phys. Rev. B, **61**, 16303 (2000).

[15] For proposals of different solid-state entanglers not based on the use of a superconductor see e.g.: W. D. Oliver, F. Yamaguchi and Y. Yamamoto, Phys. Rev. Lett., **88**, 037901 (2002); C. W. J. Beenakker *et al.*, Phys. Rev. Lett. **91**, 147901 (2003); D. S. Saraga *et al.*, Phys. Rev. Lett. **90**, 166803 (2003).

[16] A priori it could be expected that the electron/hole dwell time through the whole NISIN structure should dominate the cross over from EC to CAR. However, experimentally we find that this cross over energy scales with the thickness of the superconducting layer with the same functional dependence that the Thouless energy has. This evidence supports the interpretation that the Thouless energy corresponds to the cross over energy from EC to CAR.

[17] M. Gurvitch, M.A. Washington and H. A. Huggins, Appl. Phys. Lett., **42**, 472-474 (1983).

[18] Electrical transport and superconducting properties of very thin Nb layers similar to those used in the experiments discussed here have been thoroughly investigated in our group, in the context of research on superconducting bolometers: D. Wilms Floet *et al.*, Appl. Phys. Lett., **73**, 2826 (1998).

[19] Y. V. Fominov and M. V. Feigel'man,Phys. Rev. B **63**, 094518 (2001).

[20] N. G. Ptitsina *et al.*, Phys. Rev. B, **56**, 10089 (1997).

[21] Nonequilibrium Superconductivity, edited by D. N. Langenberg and A. I. Larkin, North Holland, Amsterdam (1986).

[22] S. G. den Hartog *et al.*, Phys. Rev. Lett., **77**, 4954 (1996).

[23] F. Pierre *et al.*, Phys. Rev. Lett., **86**, 1590 (2001).

[24] The presence of superconductivity for B up to 6 T is visible in the tunneling characteristics of J1 and J2.

[25] A. L. Yeyati, F. S. Bergeret, A. Martín-Rodero and T. M. Klapwijk, arXiv:cond-mat/0612027.

Chapter 6

Adiabatic quantum pumping at the Josephson frequency

6.1 Introduction

We analyze theoretically adiabatic quantum pumping through a normal conductor that couples the normal regions of two superconductor/normal metal/superconductor Josephson junctions. By using the phases of the superconducting order parameter in the superconducting contacts as pumping parameters, we demonstrate that a non zero pumped charge can flow through the device. The device exploits the evolution of the superconducting phases due to the ac Josephson effect, and can therefore be operated at very high frequency, resulting in a pumped current as large as a few nanoAmperes. The experimental relevance of our calculations is discussed.

6.2 Theoretical description of adiabatic pumping at the Josephson frequency

In a mesoscopic conductor in which electrons move phase coherently, a direct current can flow in response to a slowly varying periodic perturbation and in the absence of any applied bias. This phenomenon, known as quantum pumping, was first noticed by Thouless[1], who analyzed theoretically the response of an electron system to a "travelling" periodic potential $U(x-vt)$. The occurrence of quantum pumping requires that the periodic perturbation consists of at least two independent oscillating parameters $X_1(t)$ and $X_2(t)$, and that the trajectory representing the perturbation in the parameter space (X_1, X_2) encloses a finite area[2, 3]. Indeed, the proposal of Thouless satisfies these requirements since even the simplest travelling periodic potential $U(x-vt) = U_0 \sin(x-vt)$ can be written as $U(x-vt) = X_1(t)\sin(\frac{2\pi x}{\lambda}) + X_2(t)\cos(\frac{2\pi x}{\lambda})$, with $X_{1,2}(t) = X_{1,2}\cos(\frac{2\pi t}{\tau} + \phi_{1,2})$. When the cyclic perturbation is slower than the electron dwell time in the conductor, adiabatic pumping occurs and the system remains in thermodynamic equilibrium. In this case, the pumped charge can be expressed as a function of the scattering matrix and of its derivatives with respect to the pumping parameters X_1 and X_2 [3].

Attempts to investigate experimentally adiabatic quantum pumping have been made using electrostatically defined quantum dots in GaAs-based heterostructures [4]. In such a system, pumping is induced by oscillating voltages applied to the gate electrodes defining the dot. Although signatures of pumping signals may have been observed, the experiments are hindered by rectification effects originating from parasitic coupling of the *ac* signal applied to the gates [5]. Many other

proposals of devices have been put forward in the literature, in which different physical quantities have been used as pumping parameters such as a time-varying magnetic field, the height of a tunnel barrier, etc.[6, 7, 8]. Often, however, these proposals do not consider the difficulties involved in the experimental realization.

Here we demonstrate theoretically the occurrence of pumping in a system of

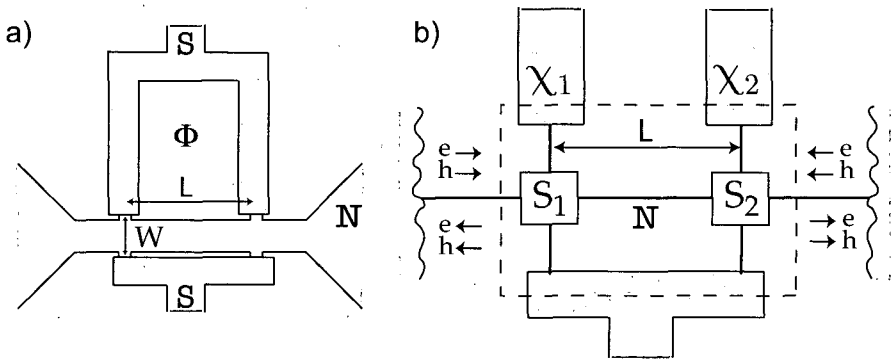

Figure 6.1: a) Layout of the proposed quantum pump, consisting of two SNS Josephson junctions in a SQUID geometry with a common normal region (The dark grey areas represent the superconductor electrodes and light grey the normal conductor). b) Diagrammatic representation of the scattering matrix of the device.

electrons and holes in a metallic conductor coupled to superconductors, where the pumping parameters are the phases of the superconducting order parameters in two different superconducting contacts. This system can operate at very high frequency without the need of feeding microwave radiation, simply by exploiting the evolution of the superconducting phases due to the *ac* Josephson effect. As a consequence, measurable pumped currents as large as a few nanoAmperes, can be expected, while avoiding spurious effects that affected previous experiments. Fig. 6.1a shows a schematic representation of the circuit that we propose. Two superconducting/normal metal/superconducting (SNS) Josephson junctions are connected in parallel via a superconducting ring, and their N regions are additionally coupled by a normal metal bridge. Andreev reflection [9] of electrons and holes takes place at each NS interface, resulting in a phase shift of the particle wavefunction which at the Fermi energy is given by $\pm\chi_{1,2}$, the phase of the superconductor order parameter at the two different superconducting contacts (the sign + is for reflection from hole to electron; the sign - for the reverse process). Hence, the total scattering matrix (S_{tot}) of the normal metal bridge connecting the left and right reservoirs depends on the quantities $X_1 = e^{i\chi_1}$ and $X_2 = e^{i\chi_2}$. We want to see if a direct current can flow in the normal metal bridge when X_1

and X_2 are used as pumping parameters.

The appealing aspect of such a device is the way in which the pumping parameters can be driven at high frequency, and their relative phase controlled. Specifically, the pumping parameters become time-dependent when a constant voltage V_{dc} is present across the SNS junctions (e.g., by biasing the junctions with a current higher than their critical current), since then $X_1(t)$ and $X_2(t) \propto e^{i\frac{2eV_{dc}}{\hbar}t}$ owing to the *ac* Josephson effect [10]. Similarly to what happens in superconducting quantum interference devices (SQUIDS), the phase difference φ between X_1 and X_2 can be easily controlled by applying a magnetic flux Φ to the superconducting loop, so that $\chi_2 = \chi_1 + \varphi$, with $\varphi = 2\pi\Phi/\Phi_0$ ($\Phi_0 = h/2e$).

To demonstrate the occurrence of pumping, we model the system in the simplest

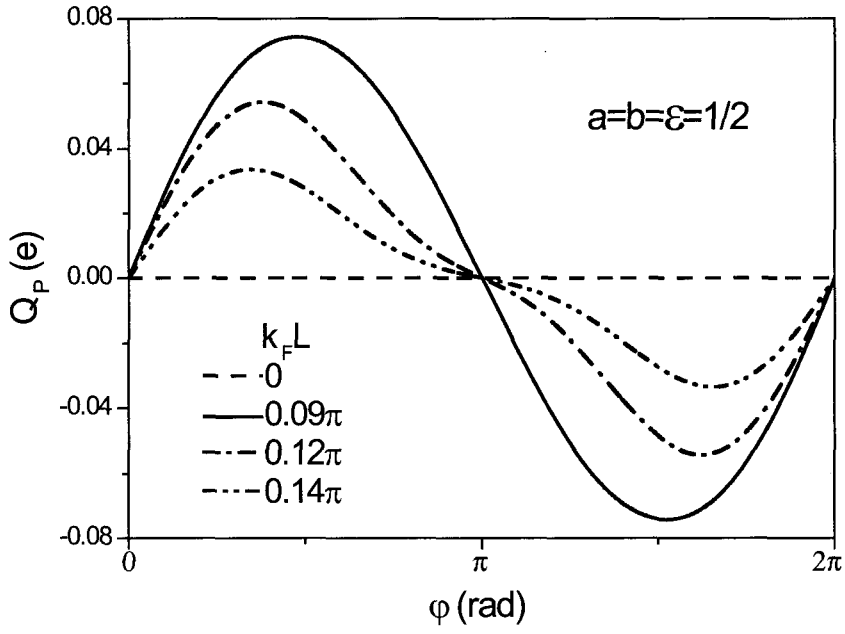

Figure 6.2: Pumped charge per cycle Q_P as a function of phase difference φ between the pumping parameters, for the case $a = b = \varepsilon = 1/2$ and different values of $k_F L$.

possible way. We confine ourselves to the case of a fully phase coherent system at $T = 0$ K. The normal conductor is taken to consist of one channel supporting ballistic motion, and the separation between the Josephson junctions L. The N/S interfaces are all supposed to be perfectly transparent, *i.e.* the probability

of Andreev reflection is unity.
The pumped current is equal to the charge pumped per cycle, multiplied by the pumping frequency. The calculation of the charge pumped per cycle follows the approach developed by Brouwer[3], modified to take into account the presence of the superconducting electrodes[8]. The relation between the charge $Q_{P,m}$ pumped in one of the two reservoirs (labelled by $m = 1, 2$) and the scattering matrix reads:

$$Q_{P,m} = e \int_0^\tau dt \left(\frac{dn_m}{dX_1} \frac{dX_1}{dt} + \frac{dn_m}{dX_2} \frac{dX_2}{dt} \right), \tag{6.1}$$

in which:

$$\frac{dn_m}{dX_{1,2}} = \frac{1}{2\pi} \sum_{i,j} \gamma_{ij} \mathrm{Im} \frac{\partial (S_{tot})_{ij}}{\partial X_{1,2}} (S_{tot})^*_{ij}, \tag{6.2}$$

where τ is the period of one pumping cycle ($\tau = \frac{2\pi}{\omega_J}$, with $\omega_J = \frac{2eV_{dc}}{\hbar}$). In Eq. 6.2, the sum over i extends to the electron and hole (e, h) channels in both leads. The sum over j is performed over the electron and hole channels only in the lead connected to the reservoir m for which the pumped charge is calculated. The function γ_{ij} is equal to $+1$ when the element $S_{i,j}$ of the scattering matrix corresponds to a process in which a current is pumped *from* lead m, $\gamma_{ij} = -1$ when a current is pumped *into* lead m. This difference in sign is due to the fact that electrons and holes contribute oppositely to the pumped charge. Since the electron and hole contributions to the pumped charge could exactly compensate each other, it is not obvious *a priori* whether a net charge can be pumped.
The problem of computing the pumped charge is then reduced to the calculation of the total scattering matrix S_{tot} of electrons and holes in the normal conductor bridge (see Fig. 6.1b), as a function of the parameters X_1 and X_2. The calculation is lengthy but conceptually straightforward (calculations were done using *Mathematica*$^{\mathrm{TM}}$). We consider a perfectly symmetric configuration with two identical SNS junctions, which are also identically coupled to the normal metal bridge. For each junction, the coupling is described by a "beam-splitter" [11], whose scattering matrix ($S_{1,2}$) is assumed to be energy independent (*i.e.*, it is the same for electrons and holes). We have chosen the simplest expression compatible with unitarity and time reversal symmetry. The expression reads:

$$S_{1,2} = \begin{pmatrix} a & \sqrt{\frac{\varepsilon}{2}} & b & \sqrt{\frac{\varepsilon}{2}} \\ \sqrt{\frac{\varepsilon}{2}} & -a & \sqrt{\frac{\varepsilon}{2}} & -b \\ b & \sqrt{\frac{\varepsilon}{2}} & a & \sqrt{\frac{\varepsilon}{2}} \\ \sqrt{\frac{\varepsilon}{2}} & -b & \sqrt{\frac{\varepsilon}{2}} & -a \end{pmatrix}, \tag{6.3}$$

where ϵ varies between 0 and 1/2 ($\epsilon/2$ is the probability for an incoming particle to be deflected towards one of the superconductors). The amplitudes for backscattering a and direct transmission b across the beam splitter satisfy the relations $a^2 + b^2 + \varepsilon = 1$ and $\varepsilon/2ab = 1$, imposed by unitarity. For every fixed value of ε two solutions, with $a > b$ and $b > a$, are possible and we considered both cases (for $\varepsilon = 1/2$ the two solutions coincide and $a = b = 1/2$).
Mixing of electrons and holes only occurs at the interface with the superconductors. Having assumed perfect transparency at the NS interfaces, the matrix describing Andreev reflection in the "vertical" branches of the circuit (see Fig.6.1) depends only on the phase χ of the superconducting order parameter. It reads:

$$S_{\mathrm{AR}} = \begin{pmatrix} 0 & r_{\mathrm{he}} \\ r_{\mathrm{eh}} & 0 \end{pmatrix} = \begin{pmatrix} 0 & -ie^{-i\chi} \\ -ie^{i\chi} & 0 \end{pmatrix}. \tag{6.4}$$

To calculate the total scattering matrix of the device we first calculate the scattering matrix associated to transport across only one SNS junction. We then consider the two SNS junction connected in series, *i.e.* we consider all the multiple reflection processes in the normal metal bridge, taking into account the corresponding dynamical phases acquired by electrons and holes. The result is the scattering matrix $S_{tot}(X_1, X_2)$ that mixes the electron and hole channels in reflection and transmission.

6.3 Discussion

Having determined S_{tot} we obtain the pumped charge from Eqs. 6.1 and 6.2. As shown in Fig. 6.2 we find that, unless $k_F L = n\pi$ (with n integer), the pumped charge is a non-zero, anti-symmetric, and 2π-periodic function of φ, as expected. The 2π periodicity in conjunction with the antisymmetry imply that the pumped charge has to vanish when $\varphi = \pm\pi$. This is the case since for $\varphi = \pi$ the trajectory in the space of the pumping parameters (X_1, X_2) does not enclose a finite area. In addition, the antisymmetry of Q_P with respect to φ also implies that the sign of the pumped current changes when reversing the sign of the relative phase of the two superconducting junctions. This results in the antisymmetry of the pumped current versus applied magnetic flux Φ (that determines the phase φ), and provides a distinctive feature that should facilitate the experimental identification of the phenomenon.
Fig. 6.3A, B, and C summarize the outcome of our calculations for the different cases $a > b$, $a = b$, and $a < b$. We first discuss the features of the results that

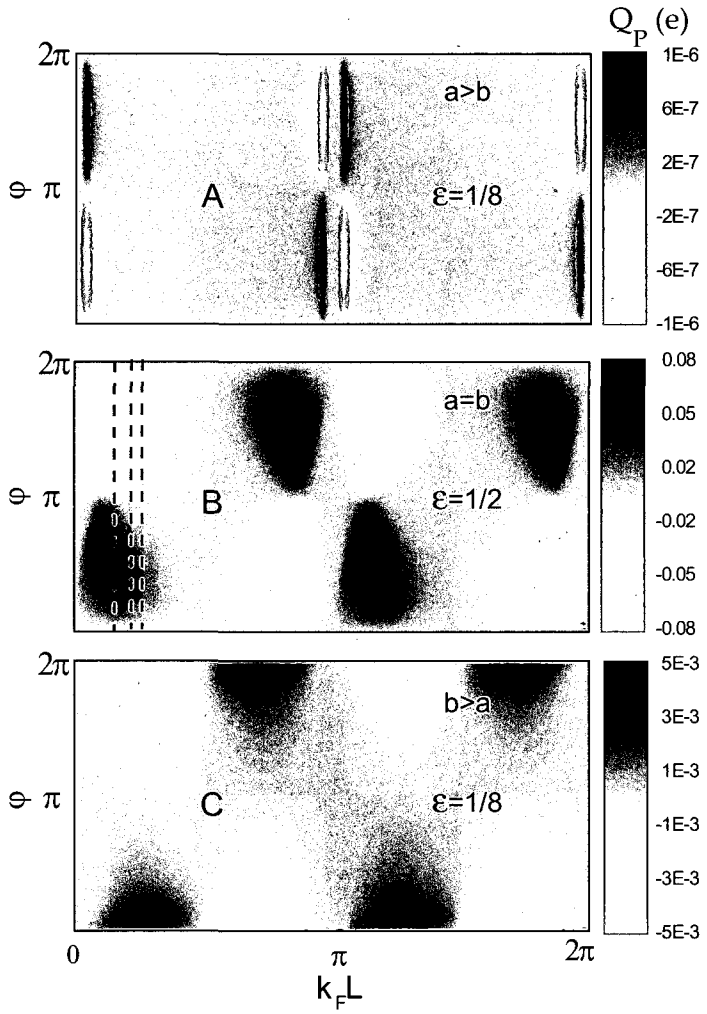

Figure 6.3: Color scale plots of Q_P as a function of $k_F L$ and φ for three distinct cases of amplitude scattering on the beam splitter: $\varepsilon = 1/8$ for $a > b$ (top), $a = b = \varepsilon = 1/2$ (center) and $\varepsilon = 1/8$ for $b > a$ (bottom). The dashed lines in the center panel correspond to the curves shown in Fig. 6.2.

are common to all three cases. We always find that the pumped charge does not depend on the separation W between the beam splitters and the superconducting leads (see Fig. 6.3). This is due to the phase conjugation [12] of electrons and

holes at the Fermi energy, since the dynamical phase acquired by an electron propagating from the beam splitter to the superconducting interface is exactly compensated by the phase acquired by the Andreev reflected hole. In all cases the dependence of Q_P on L is periodic for all values of φ and ε, with period given by $k_F L = \pi$ (k_F is the Fermi wave vector). This implies that the pumped charge is sensitive to the geometry of the device on the scale of the Fermi wavelength λ_F, indicating that charge pumping in the device considered here is a sample specific phenomenon. That this should be so is not obvious a priori : owing to phase conjugation, one may have expected the pumped charge to show a component independent of the precise geometry of the device [13].

The magnitude of the calculated pumped charge strongly depends on ε. The maximum pumped charge is approximately 0.1 electron per cycle, for $\varepsilon = 1/2$ ($a = b$). For small ε, the magnitude of Q_P decreases with decreasing ε (and eventually vanishes for $\varepsilon = 0$) both when $a > b$ and $b > a$. The dependence of Q_P on φ and $k_F L$, however, is different in the two cases.

When $a > b$ and for small values of ε (*i.e.* $a \sim 1$) the bridge connecting the two SNS junctions is only weakly coupled to the reservoirs, because backscattering at the beam-splitters is the dominant process (see Fig. 6.3A). In this regime, sharply defined resonances appear in the conductance of the system when $k_F L = n\pi$ (with n integer), due to the presence of quasi-bound states in the bridge connecting the two SNS junctions. When $k_F L = n\pi$ the energy of a quasi-bound state aligns with the Fermi levels in the reservoirs. Interestingly, the pumped charge is also significantly different from zero only when $k_F L$ is close to being a multiple of π. This suggests a close link between pumping and the presence of resonances due to quasi-bound states in the system, as already noted by others in different contexts[7]. This link is further supported by observing that increasing ε from 0 to 1/2 -corresponding to increasing the broadening of the quasi-bound states- results in a broader range of values of L for which charge pumping is observed (Fig. 6.3B).

In the case $b > a$, the behavior of the pumped charge for small values of ε is qualitatively different (see Fig. 6.3C). In this regime, the dominant process at the beam splitters is direct transmission. Therefore electrons and holes have only a small probability to be deflected from the normal bridge to the N/S interfaces. However, if they are deflected, they perform many Andreev reflections in one of the SNS junctions before they can escape again to the normal metal bridge. As a consequence, along the dominant trajectories responsible for pumping, electrons and holes have a large probability to acquire a phase $e^{iN\chi}$ (with different, and even large, integer values of N), rather than simply $e^{i\chi}$. This causes the phase dependence of the pumping signal to be richer in harmonics and, consequently,

to exhibit very strong deviations from a simple sine dependence, as seen from Fig. 6.3C.

6.4 Experimental relevance

Having established the occurrence of adiabatic quantum pumping, we briefly discuss some of the advantages of the proposed device. The use of the *ac* Josephson effect to generate the time dependence of the pumping parameters (the superconducting phases in our case) should allow operation at frequencies of several hundreds GHz. In fact, with superconductors such as Nb, NbN, or NbTiN, values for the superconducting gap Δ corresponding to frequencies in excess of 1 THz are possible, so that our superconducting pump can operate at a few hundreds GHz when the voltages applied across the SNS junctions is still sufficiently lower than Δ. At a Josephson frequency of 100 GHz, the pumped current can exceed 1 nA, which is easily measurable. Note that, since the pumping parameters are coupled to the electron-hole wave functions via Andreev reflection, the coupling will remain good at these high frequencies. In addition, the fact that no external microwave signals need to be fed into the circuit to drive the pumping parameters implies that only a negligible high-frequency power will be irradiated, thereby minimizing the possibility of rectification effects known to cause problems in other systems[5]. For the practical realization of the proposed superconducting pump we suggest the use of a ballistic InAs-based two-dimensional electron gas as normal conductor. Present technology enables the reduction of the number of conducting channels to ≈ 10 [14], which is important since the predicted effect is of the order of one channel. The use of InAs also enables the realization of the needed highly transparent contacts to superconductors [15]. Furthermore, in ballistic devices in which the distance between the two SNS junction is $L \simeq 1\mu$m, the typical propagation time in the device will be of the order of L/v_F 10^{-12} s ($v_F \simeq 10^6$ m/s is typically realized in InAs heterostructures). This is ten times faster than the period of an *ac* pumping signal oscillating at 100 GHz, ensuring that the dwell time of electrons is much shorter than the period of the ac pumping signal, as it is needed for the device to operate in the adiabatic regime.

We gratefully acknowledge M. Blauboer, Y.V. Nazarov, Y. Tokura and P.W. Brouwer for useful discussions. This research is financially supported by the Dutch Foundation for Fundamental Research (FOM) and NWO (Vernieuwingsimpuls 2000).

Bibliography

[1] D. J. Thouless, Phys. Rev. B**27**, 6083 (1983).

[2] F. Zhou, B. Spivak and B. L. Altshuler, Phys. Rev. Lett. **82**, 608 (1999).

[3] P. W. Brouwer, Phys. Rev. B **58**, 10135(R) (1998).

[4] M. Switkes, C. M. Marcus, K. Campman, A. C. Gossard, Science **283** 1905 (1999).

[5] P. W. Brouwer, Phys. Rev. B **63** 121303(R) (2001); L. DiCarlo and C. Marcus and J. S. Harris, Jr., Phys. Rev. Lett. **91**, 246804 (2003).

[6] N. B. Kopnin, A. S. Mel'nikov and V. M. Vinokur Phys. Rev. Lett. **96**, 146802 (2006); M. Moskalets and M. Büttiker, Phys. Rev. B **64**, 201305(R) (2001); J. E. Avron, A. Elgart, G. M. Graf, and L. Sadun, Phys. Rev. B **62**, 10618(R) (2000); C. Benjamin, Europ. Phys. J. B **52**, 403 (2006); M. Governale *et al.*, Phys. Rev. Lett. **95**, 256801 (2005).

[7] Y. Wei, J. Wang and H. Guo, Phys. Rev. B *62*, 9947 (2000); O. Entin-Wohlman and A. Aharony, Phys. Rev. B **66**, 035329 (2002).

[8] J. Wang *et al.*, Appl. Phys. Lett. **79**, 3977 (2001); M. Blaauboer, Phys. Rev. B **65**, 235318 (2002); F. Taddei, M. Governale and R. Fazio, Phys. Rev. B **70**, 052510 (2004).

[9] A. F. Andreev, Sov. Phys. JETP **19**, 1228 (1964).

[10] K. K. Likharev, *Dynamics of Josephson Junctions and Circuits*, New York, Gordon and Breach (1986).

[11] M. Büttiker, IBM J. Res. Dev. **32**, 63 (1988).

[12] H. Takayanagi and B. J. van Wees in *Mesoscopic Electron Transport* (NATO Science Series E: Applied Sciences **345** 469-501), Eds. L. L. Sohn, G. Schön and L. P. Kouwenhoven, Dordrecht, Kluwer Academic (1997).

[13] An "ensemble averaged" component of pumped current has been found previously by Zhou (F. Zhou, Int. Jour. Mod. Phys. B **15**, 117 (2001)), who had to assume electron-hole asymmetry on the scale of the superconducting gap. Since this asymmetry is usually small, we expect that in real devices the sample specific effect that we calculate here is much larger in amplitude than the one discussed by Zhou.

[14] A. F. Morpurgo, B. J. van Wees, T. M. Klapwijk and G. Borghs Appl. Phys. Lett. **70**, 1435 (1997).

[15] J. P. Heida, B. J. van Wees, T. M. Klapwijk and G. Borghs Phys. Rev. B **57**, 5618(R) (1998).

Chapter 7

Reproducible Low Contact Resistance in Rubrene Single-Crystal Field-Effect Transistors with Nickel Source and Drain Electrodes

The results presented in this Chapter have been published as I. N. Hulea, S. Russo, A. Molinari and A. F. Morpurgo *Appl. Phys. Lett.* **88**, 113512 (2006)

7.1 Introduction

We have investigated the contact resistance of rubrene single-crystal field-effect transistors (FETs) with Nickel electrodes by performing scaling experiments on devices with channel length ranging from 200 nm up to 300 μm. We find that the contact resistance can be as low as 100 Ωcm with narrowly spread fluctuations. For comparison, we have also performed scaling experiments on similar Gold-contacted devices, and found that the reproducibility of FETs with Nickel electrodes is largely superior. These results indicate that Nickel is a very promising electrode material for the reproducible fabrication of low resistance contacts in organic FETs.

7.2 Experiment

The possibility to downscale organic field-effect transistors (FETs) is currently hindered by the high contact resistance present at the interface between the metal electrodes and the organic semiconductor [1]. One of the main experimental problems in the study and optimization of the contact resistance originates from the observed irreproducibility. In spite of the large effort put in the investigation of contact effects [1-6], the reason for both the high values and the irreproducibility of the contact resistance are not currently understood. Many different phenomena are likely to play an important role, including the presence of grain boundaries at the metal/organic interfaces, the interface fabrication process (e.g., metal diffusion into the organic semiconductors and extrinsic damage introduced during the device assembly process), fluctuations in the work function of the metal electrodes, etc. Currently, the problem seems to be particularly severe for oligomer-based devices. Whereas for FETs based on a number of different polymers it has been found that the contact resistance scales linearly with the carrier mobility [7], for transistors based on oligomers a very broad range of contact resistance values have been measured on identically prepared devices, and no systematic behavior has been observed [6].

To address the issue of contact resistance in oligomer transistors, we have recently started the investigation of organic single-crystal FETs with different metal contacts. Single-crystal devices are particularly advantageous for this purpose because their electrical characteristics exhibit an excellent level of reproducibility from sample to sample [8]. This is crucial for a reliable comparison of FETs with different channel length, i.e. to perform scaling experiments from which the value of the contact resistance can be extracted.

Here we focus on rubrene single-crystal FETs with Nickel electrodes. Nickel

was chosen because, although it oxidizes in air, its native oxide is conductive and has a work-function of 5.0 eV [9], ideally suited to inject carriers into the highest occupied molecular orbital of many molecular semiconductors. By performing a conventional scaling analysis [6, 7, 10] of the electrical characteristics of these devices we extract the value of the contact resistance. We find values of R_C as low as 100 Ωcm, i.e. 50 times smaller than in the best oligomer FET reported to date [6]. The spread in values in the contact resistance measured on transistors fabricated on the same crystal is small (less than a factor of 2); devices fabricated on different crystals exhibit a somewhat large spread, ranging from 100 Ωcm to 1.5 kΩcm (and typically between 200 Ωcm and 1 kΩcm), but still considerably smaller than what has been observed so far in oligomer FETs. For comparison, we have also investigated a number of single-crystal FETs contacted with gold electrodes, the material commonly used for the fabrication of contacts in organic transistors, and found a considerably lower reproducibility level. This indicates that Nickel is a very promising material for the fabrication of contacts for organic transistors, even though the surface of the electrodes oxidizes. We note that Nickel is also advantageous as compared to gold because it is more mechanically robust, which should minimize the possibility of (electro)migration into organic materials during device operation, and cheaper.

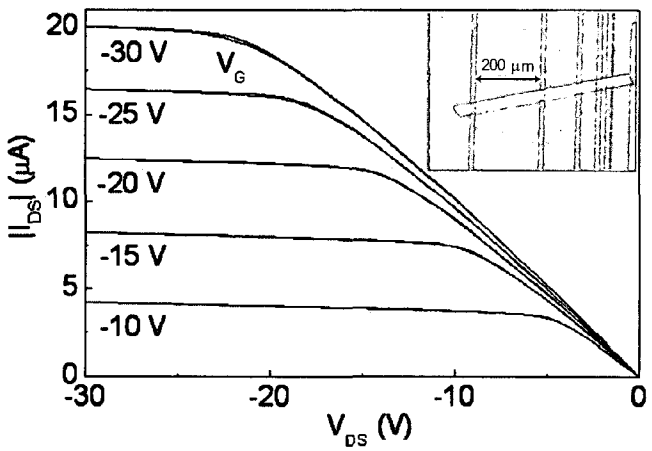

Figure 7.1: Typical transistor characteristics measured on a rubrene single-crystal FET with Ni source-drain electrodes. The inset shows a top view of one of the devices used in our investigation (for this device the crystal width W is 35 μm).

The FET fabrication is based on electrostatic bonding of rubrene single crystals to a doped silicon substrate (acting as a gate) covered with a 200 nm- thick

thermally grown SiO_2, with prefabricated source and drain contacts (see Ref.[11] for details). The contacts are prepared by conventional optical or e-beam lithography, nickel electron-beam evaporation (20 nm), and lift-off. The rubrene crystals are separately grown by means of a vapor phase transport technique [12]; they are millimeters long and their width and thickness are respectively of the order of 100 μm and 1 μm. The device layout (see Fig.7.1) is such that FETs with different channel lengths are fabricated on the same single crystal. Many different samples were studied with channel length ranging from 200 nm to 300 μm. Prior to the crystal adhesion, an oxygen plasma treatment is performed to remove residues of resists possibly still present on the SiO_2 surface. Although the exposure of the electrodes to oxygen plasma contributes to the oxidation of the Nickel surface, it does not preclude the realization of reproducible, low-resistance electrodes.

In the linear regime of transistor operation the total device resistance $R_T(L)$ can be written as [6, 7, 10]:

$$R_T(L) = R_{ch}(L) + R_C, \tag{7.1}$$

Here

$$R_{ch} = \frac{L}{WC_i(V_G - V_{TH})}\frac{1}{\mu} \tag{7.2}$$

is the channel resistance and R_C a length independent contact resistance, C_i is the capacitance of the insulating layer per unit area, V_G and V_{TH} are the gate and the threshold voltage, W is the channel width, and μ the hole mobility. The contact resistance is obtained by extrapolating the experimental data to zero channel length. The slope of the R_T-vs-L curves also permits to extract the carrier mobility. The comparison of the mobility value obtained from this slope with the one obtained from the usual formula for the linear regime of the individual FETs

$$\mu = \frac{L}{WC_iV_{DS}}\frac{\partial I_{DS}}{\partial V_G} \tag{7.3}$$

is used as a consistency check of our analysis.

7.3 Electrical characteristics of Rubrene FETs with Ni and Au contacts

Fig. 7.1 shows the electrical characteristics measured on one of the FETs that we have investigated and it is typical for all our Ni contacted devices. The data have

been measured with the FETs in high vacuum ($p < 10^{-6}$ mbar) and dark, using an Agilent E5270A or a HP 4192A parameter analyzer. Usually, no hysteresis is observed in the I_{DS} -V_{DS} plot at fixed gate voltage and in the I_{DS} -V_G at fixed source drain bias. The linearity of the I_{DS} -V_{DS} at low bias gives a first indication of a good contact quality.

The scaling of the total device resistance R_T versus device length L is shown in Fig. 7.2a for different values of the gate voltage V_G, with V_{DS} = -1 V, for a sample with channel length in the range 20 -200 μm. Clearly, R_T does scale linearly with L, implying that for a given device the contact resistance R_C is approximately the same irrespective of the channel length. The value of R_C is then given by the intercept at L=0. To compare the behavior of devices fabricated on different crystals we normalize the contact resistance to the channel width, i.e. we consider $R_C^* = R_C W$ [1, 6]. For all different samples (in total, approximately 50 individual FETs were measured) we find values of R_C^* in between 100 Ωcm and 1.5 kΩcm, and most typically in between 200 Ωcm and 1 kΩcm, at V_G= -30 V, usually only very weakly dependent on gate voltage.

We have also analyzed the spread in contact resistance values for FETs fabricated on the same crystal, by looking at devices with L ranging from 200 nm to a few microns. Because the rubrene crystals have a high mobility (2-6 cm^2/Vs), the contact resistance exceeds the channel resistance in devices whose channel length is less than approximately 5-10 μm. For these devices, the total resistance is essentially independent of channel length, as shown in Fig. 7.2c. These data also show that for FETs fabricated on the same crystal, the spread in contact resistance values is less than a factor of two. Thus, both for short and long channel devices, we conclude that the values of R_C^* in Nickel-contacted Rubrene single crystal FETs are up to 50 times smaller than the smallest contact resistance (5 kΩcm) reported to date for oligomer-based FETs [6], and that they exhibit a drastic improvement in reproducibility as compared devices studied in the past.

For devices with a channel length of 100 μm or longer, we have calculated the value of mobility from the FET characteristics using Eq. 7.3, as well as from the scaling analysis using Eq. 7.2. The comparison of the values obtained in these two different ways (see inset of Fig.7.3) exhibits a remarkable agreement. This agreement indicates the consistency of our analysis and gives full confidence on the quantitative values obtained for the contact resistance.

To understand if the low values and the reproducibility of the contact resistance are due to the use of Nickel electrodes, or if they are just a consequence of using high-quality organic single crystals for the device fabrication, we have performed a scaling analysis also for several gold-contacted single crystal FETs. In all of these gold-contacted devices the mobility obtained via Eq. 7.3 (for

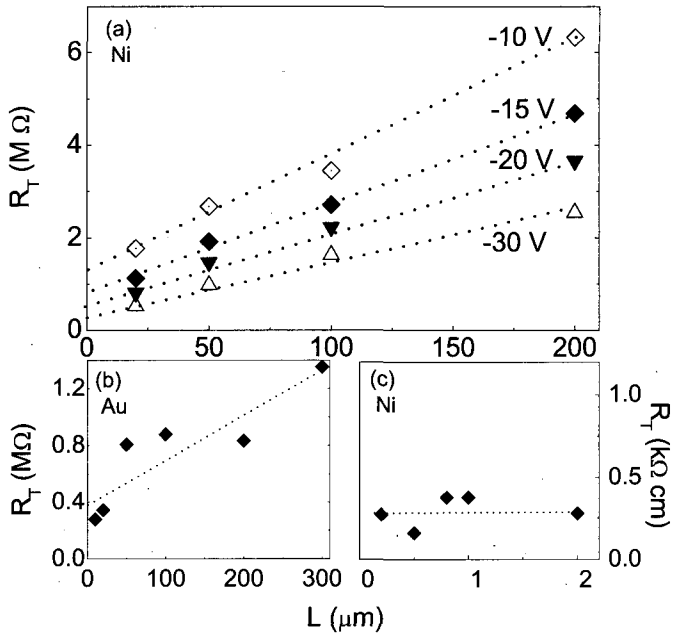

Figure 7.2: (a) Scaling of the device resistance for Nickel contacted devices as a function of channel length for different values of the gate voltages (W = 35 μm). The intercept at $L = 0$ gives the contact resistance. (b) Similar scaling curve for a gold-contacted FET: it is visible that the deviations from linear scaling are larger in this devices as compared to Nickel-contacted devices. In other gold-contacted FETs, the magnitude of the fluctuations was larger than for the sample whose data are shown here. (c) Normalized resistance measured on a Ni-contacted FETs fabricated on the same rubrene crystal. R_T does not depend on L because for $L < 2\mu$m the channel resistance is negligible with respect to the contact resistance. In all panels, the lines are a guide to the eye.

long channel devices, L > 100 μm) ranged from 2 to 6 cm^2/Vs, depending on the crystal [13]. This indicates that the crystal quality is the same for gold and Nickel-contacted FETs. However, we found that in FETs with gold electrodes the fluctuations in contact resistance are much larger and in most cases prevent the observation of a clear scaling between R_T and L, for channel lengths comparable to or smaller than 50-100 μm. This is illustrated in Fig. 7.2 b that shows the data for the gold-contacted devices which, among all devices measured, exhibited the best $R_T(L)$ scaling: as it is clear the fluctuations in measured resistance are much larger than for the Nickel-contacted devices (Fig. 7.2a and c). As a

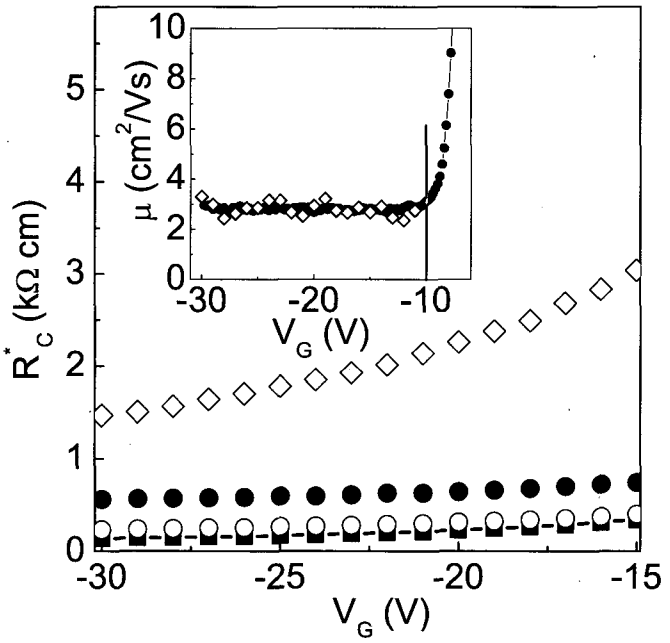

Figure 7.3: Gate voltage dependence of the normalized contact resistance R_C^* for four of the samples studied. The insert shows the gate voltage dependence of the mobility μ determined from Eq. 7.3 (full circles) and from scaling $R_T(L)$ using Eq. 7.2 (open diamonds). The vertical line denotes the beginning of the linear regime. For all the measurements V_{DS}= -1 V

consequence of poor scaling, the data on gold-contacted transistors do not allow a precise determination of R_C but only a rough estimate of the lower limit, 5 kΩcm, with a spread of several times this value (even for FETs fabricated on the same rubrene crystal).

7.4 Conclusions

From the above comparison, we conclude that Nickel does perform better than gold as electrode material and that the reproducibility in the contact resistance is not only due to the use of single-crystalline material for the FET fabrication. As gold has been used for contact fabrication in most of the organic FETs fabricated in the past also in virtue of its chemical inertness, the fact that Nickel does oxidize in air makes our findings particularly unexpected. Nevertheless, the low contact

resistance values can be explained in terms of the work function of oxidized Nickel that has been measured to be equal to 5.0 eV[6] -ideal for hole injection into organic semiconductors- and by the fact that non-stoichiometric NiO_x is a reasonably good conductor. In this regard, it is also worth noting that recently NiO_x contacts have shown promising results as hole injectors in organic light emitting diodes [14]. Why oxidized Nickel performs better than gold [15], which is a better conductor and has a comparable work function value, is less clear: for its technological relevance, this issue deserves additional investigations.

In conclusion, we have performed a scaling analysis of the electrical characteristics of rubrene single-crystal FETs to show that nickel can be used to fabricate source and drain electrodes with an unprecedented low contact resistance and excellent reproducibility. However, in order to use nickel contacts to inject spin polarized charges in the organic semiconductor it is necessary to implement tunnel barriers at the ferro-organic interfaces to overcome the problem of conductance mismatch (see Section 1.3).

Bibliography

[1] L. Burgi, T. J. Richards, R. H. Friend, and H. Sirringhaus, Journal of Applied Physics **94**, 6129 (2003).

[2] Y. L. Shen, A. R. Hosseini, M. H. Wong, G. G. Malliaras, Chemphyschem **5**, 16 (2004).

[3] P. V. Pesavento, R. J. Chesterfield, C. R. Newman, and C. D. Frisbie, Journal of Applied Physics **96**, 7312 (2004).

[4] R. A. Street and A. Salleo, Applied Physics Letters **81**, 2887 (2002).

[5] P. V. Necliudov, M. S. Shur, D. J. Grundlach, and T. N. Jackson, Solid-State Electronics **47**, 259 (2003).

[6] E. J. Meijer, G. H. Gelinck, E. van Veenendaal, B. -H. Huisman, D. M. de Leeuw, and T.M. Klapwijk, Applied Physics Letters **82**, 4576 (2003).

[7] B. H. Hamadani and D. Natelson, Applied Physics Letters **84**, 443 (2004).

[8] R. W. I. de Boer, M. E. Gerhenson, A. F. Morpurgo, and V. Podzorov, Physica Status Solidi A- Applied Research **201**, 1302 (2004).

[9] J. Olivier, B. Servet, M. Vergnolle, M. Mosca, and G. Garry, Synthetic Metals **122**, 87 (2001).

[10] G. B. Blanchet, C. R. Fincher, M. Lefenfeld, and J. A. Rogers, Applied Physics Letters **84**, 296 (2004).

[11] R. W. I. de Boer, T. M. Klapwijk, and A. F. Morpurgo, Applied Physics Letters **84**, 296 (2004).

[12] R. A. Laudise, C. Kloc, P. G. Simpkins, and T. Siegrist, Journal of Crystal Growth **187**, 449 (1998).

[13] A. F. Stassen, R. W. I. de Boer, N. N. Iosad, and A. F. Morpurgo, Applied Physics Letters **85**, 3899 (2004).

[14] I. M. Chan and C. Hong, Thin Solid Films **450**, 204 (2004).

[15] Note that very recently pentacene thin-film FETs with evaporated NiOx contacts have been claimed to have better performance than identically prepared devices with gold contacts. See J. Lee, D. K. Hwang, J. M. Choi, K. Lee, J. H. Kim, S. Im, J. H. Park and E. Kim, Applied Physics Letters **87**, 023504 (2005). In this work, however, the value of the contact resistance was not measured.

Appendix A

Tunnel junctions fabrication process

The samples investigated in Chapter 5 are based on a metallic multilayer structure N_1ISIN_2 which is prepared on an oxidized Silicon substrate. All the different layers in the structure are sputter-deposited in a single step, using a multi-target Nordiko 2000 system with a background pressure of $2 - 3 \cdot 10^{-7}$mbar. The precise sequence of the deposition process is as follows. A 50 nm thick Al film is deposited and oxidized *in-situ* (O_2 pressure: $2.3 \cdot 10^{-2}$mbar for 30 minutes resulting in a junction transparency of $T \sim 10^{-5}$), to form the tunnel barrier J1. Next, Nb layer is deposited as common junction electrode. Subsequently, a thin ($\sim$ 5 nm) Al layer is deposited on the Nb film and oxidized, to form the tunnel barrier J2. Finally, a 50 nm thick Al layer is deposited on top (Fig. 1a).

The separation between the two tunnel barriers (junctions J1 and J2) is determined by the Nb thickness plus the remaining thickness of the thin Al layer. We refer to this superconducting bilayer as S.

Fig. 1 illustrates the sequence of processing steps needed for the sample fabrication. First, the multilayer (Fig. 1a) is coated with photo-resist (Fig. 1b) and photolithography is used to define the junction area. Next, we remove the top Aluminum layer as well as the superconducting layer using a Chlorine-based reactive ion etching process (RIE, $Cl_2/N_2/BCl_3$ with ratio 5sccm/25sccm/10sccm at 15 μbar and 50 W power). At this point, before removing the photoresist, the sample is exposed to an oxygen plasma (O_2 pressure of 2 mbarr, voltage bias 100 V and 30 W power) and anodization process is performed in a saturated solution of oxalic acid in DI water. This results in the isotropic oxidation of a 10 nm of Aluminum, which is necessary in order to prevent short circuits at the junction edges. A second lithography step (Fig. 1d) and Cl_2 RIE is used to define the contact to the superconducting layer (Fig. 1e). Also in this case, before removing the photo-resist mask the sample is treated with oxygen plasma. A layer of 200 nm SiO_2 is sputtered on a lift-off photo-resist mask, leaving exposed only the contact area of each layer (Fig. 1f). A final photolithography/sputtering/lift-off

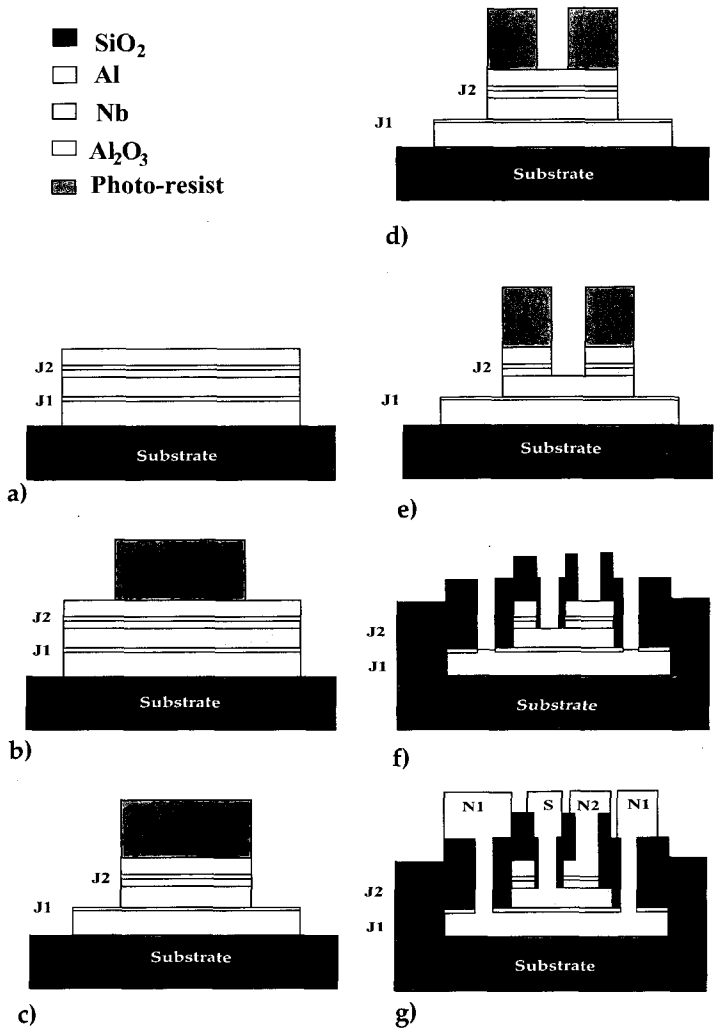

Figure 1: Cross section illustration of the different steps of the sample fabrication process described in the text. In the figures, the dimensions (thickness and lateral width) of the different features (not to scale) have been drawn to emphasize different relevant aspects of the devices.

step is used to form independent 300 nm Al/Nb contacts to each layer (Fig. 1g) of the structure.

Electrical characterization of the superconducting layers

The electrical transport and superconducting properties of very thin Nb layers similar to those used in the experiments discussed here have been thoroughly investigated in the group of Prof. dr. ir. T.M. Klapwijk, in the context of research on superconducting bolometers (Ref. [1]). For Nb layers approximately 10 nm thick, the transition temperature is suppressed as compared to the bulk value, and is typically between 5 and 6 K. The diffusion constant, determined from the temperature dependence of the critical magnetic field H_{c2} (Ref. [2]), is found to be $D = 1.6\ cm^2/s$. The (electron) elastic mean free path l_e is obtained from the relation $l_e = 3D/v_f \simeq 2$ nm, where the Fermi velocity $v_f = 2.8 \cdot 10^5 m/s$ was taken from Ref.[3].
The presence of the thin ($\simeq$ 5 nm) Al layer on top of the Nb does not substantially alter the properties of the superconducting layer. In particular, the tunneling characteristics of junctions J1 and J2 do not show any difference in the gap value as well as in the normal state resistance (R_n, measured when $T < T_c^S$ using a bias well above the superconducting gap) or sub-gap resistance ($R_{sub-gap}$). This indicates that the superconducting properties of the Nb/Al layer are uniform across its thickness (so that Nb/Al layer can be considered as a uniform superconductor).
In the table below are summarized the values of the superconducting gap (obtained from fitting the tunnelling characteristics using the BCS density of states), of R_n, of $R_{sub-gap}$, and of R_nA (defined as normal state resistance times junction area) measured on the devices with different thickness of the S layer. No significant deviation in the values of these parameters was observed for samples obtained from the same fabrication batch. However variations in the normal state resistance between different batch samples are normally present, due to non controllable fluctuations in the oxidation conditions.

$S\ thickness(nm)$	$R_n(\Omega)$	$R_{sub-gap}(\Omega)$	$\Delta(mV)$	$R_nA(\Omega\mu m^2)$
15	4.8	100	0.92	153.6
50	1.7	96	1.45	54.4
200	0.9	98	1.48	28.8

Bibliography

[1] D. W. Floet *et al.*, Appl. Phys. Lett. **73**, 2826 (1998).

[2] E. M. Gershenson *et al.*, Sov. Phys. JETP **70**, 505 (1990).

[3] N. G. Ptitsina *et al.*, Phys. Rev. B **56**, 10089 (1997).

Summary

of the Ph.D. Thesis

"Crossed Andreev reflection and electron transport in ferromagnetic hybrid structures"

by Saverio Russo

The properties of electronic transport at interfaces between different materials -*e.g.* heterointerfaces- are intensively studied for both technological and fundamental interest. The understanding of the electron injection processes in these hybrid devices is a fertile research field, in particular for that branch of electronics which tries predominantly to identify new ways to process, transmit and store information by taking advantage of the quantum wave nature of carriers, their charge and magnetic moment -*i.e. spin-electronics*. Random access memory (MRAM) represents an example of such a hybrid device which, by taking advantage of quantum tunneling of charge carriers between ferromagnetic contacts separated by an insulator, ensures high speed operation with a low power consumption. Furthermore, the development of new material systems -*e.g.* ferromagnetic semiconductors, organic semiconductors, etc.. - can lead to an impressively rich variety of electronic transport and injection processes in hybrid devices. Even relatively well known heterointerfaces -*e.g.* superconductor/normal metal- can reserve extremely interesting transport mechanisms when engineered in a particular layout device.

Some of these issues have been experimentally or theoretically addressed in this thesis, by investigating the transport in three different kinds of heterointerfaces: superconductor, ferromagnetic semiconductor and organic semiconductor based hybrid structures. A brief and general introduction to heterointerfaces and transport in the three different kinds of hybrid devices is presented in *Chapter 1*. In *Chapter 2* we present the fundamental theoretical concepts necessary to understand the transport mechanisms through the heterointerfaces studied in the forthcoming chapters. Furthermore, in this Chapter we have included the charac-

terization measurements on actual devices to study new transport mechanisms. *Chapter 3* reports on the understanding of transport and magnetic properties of a new class of magnetic semiconductors: GaMnAs. This is a necessary step for determining the relevance of this magnetic semiconductor for spin electronic devices. We pattern the GaMnAs substrate in Hall-bar geometry with a particular orientation of the channel of conduction with respect to the easy axes of magnetization, and we present a systematic investigation of the longitudinal and transverse magnetoresistance of a GaMnAs single ferromagnetic domain. We show that a fully quantitative description of the experimental data can be obtained with a single domain model when taking into account the intrinsic dependence of the resistivity on the magnetic induction. At the end of this Chapter we discuss briefly the microscopic origin of the experimentally observed B-dependence of the transversal magnetoresistance in relation to the magneto-impurity scattering model. The quantitative understanding of anisotropic magnetoresistance reached in our work makes it possible to separate the magnetization-related from the intrinsic magnetoresistance (longitudinal and transversal), thus enabling a detailed study of the latter.

The capability to exploit the potentials offered by GaMnAs in transport processes depends on the understanding of material properties such as the density of states. This is the subject covered in the experiments presented in *Chapter 4*. In order to gain insight into the intrinsic physical properties of this ferromagnetic semiconductor we study transport in superconductor (NbTiN)/GaMnAs hybrid structures. In particular, we find experimentally a tunnel barrier at the interface between GaMnAs and NbTiN. The tunnel differential conductance at low temperature displays a $\sqrt{V}$ dependence, consistent with the opening of a correlation gap in the density of states of GaMnAs. We show that low temperature annealing, by removing the interstitial Mn defects, acts on the electron-electron interaction leading to a modification of the correlation gap. Hence, low temperature annealing is an empirical external knob which acts on the intrinsic material properties and affects transport mechanisms in GaMnAs based hybrid devices.

In *Chapter 5* we continue to use superconducting materials. We study transport mechanisms in a normal metal-insulator-superconductor multilayer structure. We demonstrate experimentally that it is possible to inject electrons from two spatially separated normal metal leads into the superconductor in which the electrons form a Cooper pair. As the electrons forming a Cooper pair are in a quantum mechanical entangled state, our device can offer the possibility to access fundamental properties of quantum mechanics in solid state physics. We demonstrate that non-local Andreev reflection and its competing effect, elastic cotunneling, depend strongly on the thickness of the superconducting layer, and

in particular their amplitude is exponentially suppressed when the thickness of the superconductor exceeds the superconducting coherence length. We find that the probability of the two processes is energy dependent, with elastic cotunneling dominating at low energy and non-local Andreev reflection at higher energies. The energy scale of the crossover is a very characteristic feature which serves as a test for theoretical interpretations.

In *Chapter 6* we present a theoretical study of adiabatic quantum pumping in a normal metal conductor coupling the normal regions of two SNS Josephson junctions. The pumping parameters are the phases of the superconducting order parameter in the different superconducting contacts. Within a ballistic model and using a scattering matrix approach, we demonstrate that a non zero pumped charge can flow through the device. Since the proposed adiabatic pump exploits the evolution of the superconducting phases due to the ac Josephson effect, this system can be operated at very high frequency resulting in a pumped current as large as a nanoAmperes per channel of conduction. Finally, we discuss the experimental relevance of our calculations.

In the last Chapter, *Chapter 7*, we present a systematic study of the contact resistance of rubrene single-crystal field-effect transistors (FETs) with Nickel electrodes by performing scaling experiments on devices with channel length ranging from 200 nm up to 300 μm. We find that the contact resistance can be as low as 100 Ωcm with narrowly spread fluctuations. These results indicate that nickel is a very promising electrode material for the reproducible fabrication of low resistance contacts in organic FETs.

Samenvatting

van het proefschrift

"Crossed Andreev reflection and electron transport in ferromagnetic hybrid structures"

door Saverio Russo

De eigenschappen van elektronisch transport door grensvlakken tussen verschillende materialen (hetero-grensvlakken) worden intensief bestudeerd vanuit technologische en fundamentele belangstelling. Het begrip van elektron-injectie processen in deze hybride schakelingen is een vruchtbaar onderzoeksveld, in het bijzonder voor het subveld de spin-elektronica. In dit veld probeert men voornamelijk wegen te identificeren om informatie te verwerken, versturen, en op te slaan, door de quantum-eigenschappen van ladingsdragers zoals hun golf-karakter, lading, en magnetisch moment, uit te buiten. Zogenoemd Random access memory (MRAM) is een voorbeeld van zo'n hybride schakeling. Deze schakeling buit de quantum-tunneling van ladingsdragers tussen ferromagnetische contacten gescheiden door een isolator uit, en zorgt zo voor een snelle werking met een laag vermogensverbruik. Bovendien kan de ontwikkeling van nieuwe materiaal-systemen - zoals ferromagnetische halfgeleiders, organische halfgeleiders etc. - leiden tot een indrukwekkend grote variëteit van elektronische transport- en injectie-processen in hybride schakelingen. Zelfs relatief goed begrepen hetero-grensvlakken - bijvoorbeeld supergeleider/normaal metaal - kunnen zeer interessante transport mechanismen laten zien als ze toegepast worden in schakelingen met bepaalde specifieke configuraties.

Sommige van deze zaken zijn experimenteel of theoretisch behandeld in dit proefschrift, door het transport in drie verschillende soorten hetero-grensvlakken te onderzoeken: supergeleider, ferromagnetische halfgeleider, en organische halfgeleider gebaseerde hybride structuren. In *Hoofdstuk 1* wordt een korte en algemene introductie in hetero-grensvlakken en transport in deze drie verschillende soorten hybride schakelingen gegeven. In *Hoofdstuk 2* behandelen we de fundamente-

le theoretische concepten die nodig zijn om de transport mechanismen door de hetero-grensvlakken die bestudeerd worden in de volgende hoofdstukken, te begrijpen. Bovendien zijn in dit Hoofdstuk de karakterisatie-metingen aan feitelijke schakelingen die zullen worden gebruikt om nieuwe transport mechanismen te bestuderen opgenomen.

Hoofdstuk 3 doet verslag van ons begrip van het transport en de magnetische eigenschappen van een nieuwe soort magnetische halfgeleiders: GaMnAs. Deze stap is noodzakelijk om de relevantie van deze magnetische halfgeleider voor spin-elektronische schakelingen te bepalen. We vormen het GaMnAs substraat in een zogenoemde Hall-bar geometrie met een specifieke oriëntatie van het geleidingskanaal ten opzichte van de makkelijke magnetisatie-assen, en we presenteren een systematisch onderzoek van de longitudinale en transversale magnetoweerstand van een enkel ferromagnetisch domein. We laten zien dat een volledig kwantitatieve beschrijving van de experimentele data verkregen kan worden met een enkel-domein model, als we rekening houden met de intrinsieke afhankelijkheid van de weerstand van de magnetisatie. Aan het eind van dit Hoofdstuk bediscussiëren we kort de microscopische oorzaak van de experimenteel waargenomen B-afhankelijkheid van de transversale magnetoweerstand in relatie tot de verstrooiings door magnetische onzuiverheden. Het kwantitatieve begrip van de anisotrope magnetoweerstand dat we bereikt hebben in ons werk, maakt het mogelijk om de magnetisatie-gerelateerde van de intrinsieke magnetoweerstand (longitudinaal en transversaal) te scheiden, en daarme het laatste tot in detail te bestuderen.

Het vermogen om de mogelijkheden die door GaMnAs in transport processen geboden worden, uit te buiten, hangt af van het begrip van de materiaal-eigenschappen zoals de toestandsdichtheid. Dit is het onderwerp dat behandeld wordt in de experimenten die gepresenteerd worden in Hoofdstuk 4. Om inzicht te verkrijgen in de intrinsieke natuurkundige eigenschappen van deze ferromagnetische halfgeleider, bestuderen we transport in supergeleider (NbTiN)/GaMnAs hybride structuren. In het bijzonder ontdekken we dat er zich een tunnel-barriëre aan het grensvlak tussen GaMnAs en NbTiN bevindt. De differentiële tunnel-geleiding bij lage temperatuur laat een $\sqrt{V}$ afhankelijkheid zien, consistent met de opening van een correlatie-band in de toestandsdichtheid van GaMnAs. We laten zien dat een lage temperatuur warmtebehandeling invloed heeft op de elektron-elektron interactie door interstitiële Mn defecten te verwijderen hetgeen leidt tot een wijziging in de correlatie-band. Hieruit volgt dat een lage temperatuur warmtebehandeling een externe knop is die de intrinsieke materiaal-eigenschappen, en daarmee de transport mechanismen in GaMnAs-gebaseerde hybride schakelingen beinvloedt.

In *Hoofdstuk 5* gaan we door met het gebruiken van supergeleidende materi-

alen. We bestuderen transport mechanismen in een normaal metaal-isolator-supergeleider multilaag structuur. We demonstreren experimenteel dat het mogelijk is om elektronen vanuit twee ruimtelijk gescheiden normaal-metalen contacten te injecteren in de supergeleider, alwaar ze een Cooper-paar zullen vormen. Omdat elektronen die een Cooper-paar vormen in een quantum-mechanische verstrengelde toestand zijn, kan onze schakeling de mogelijkheid bieden fundamentele eigenschappen van de quantum-mechanica bereikbaar te maken binnen vaste stof natuurkunde. We laten zien dat niet-lokale Andreev reflectie en het concurrerende effect, elastische co-tunneling, sterk afhangen van de dikte van de supergeleidende laag, en in het bijzonder dat hun amplitude exponentieel wordt gedempt als de dikte van de supergeleider groter is dan de supergeleidende coherentie lengte. We zien dat de kans dat de twee processen plaatsvinden afhankelijk is van de energie, waarbij elastische co-tunneling domineert bij lage energie en niet-lokale Andreev reflectie bij hogere energieën. De energie-schaal van de overgang is een zeer karakteristiek kenmerk dat dient als een test voor theoretische interpretaties.

In *Hoofdstuk 6* presenteren we een theoretische studie van adiabatisch quantum pompen in een normaal metalen geleider die de normale gebieden van twee SNS Josephson schakelingen koppelt. De pomp-parameters zijn de fasen van de supergeleidende orde-parameter in de verschillende supergeleidende contacten. Binnen een ballistisch model en gebruik makend van een verstrooiingsmatrix-benadering laten we zien dat een eindige gepompte lading kan stromen door de schakeling. Omdat de voorgestelde adiabatische pomp gebruik maakt van de evolutie van de supergeleidende fasen door het wisselstroom-Josephson effect, kan dit systeem werken bij een heel hoge frequentie, hetgeen resulteert in een gepompte stroom die nano-Ampères per geleidingskanaal kan bedragen. Tenslotte bediscussiëren we de experimentele relevantie van onze berekeningen.

In het laatste Hoofdstuk, *Hoofdstuk 7*, presenteren we een systematische studie van de contact-weerstand van rubreen *één*-kristallen in veld-effect transistoren (FETs) met nikkel elektroden, door schalingsexperimenten op schakelingen met een karakteristieke lengte van 200 nm tot 300 μm uit te voeren. We ontdekken dat de contactweerstand zo laag als 100 Ωcm kan zijn, met een kleine spreiding in afwijkingen. Deze resultaten wijzen erop dat nikkel een erg veelbelovend elektrode materiaal is voor het reproduceerbaar fabriceren van lage weerstand contacten in organische FETs.

Curriculum Vitae

Saverio Russo

14-11-1978	Born in Canosa di Puglia, Italy
1992-1997	High school at "Liceo scientifico Aldo Moro", Margherita di Savoia, Italy
1997-2002	M.Sc degree in Physics *cum laude*, Universitá di Pisa, Italy Subject: *Nanofabrication and magnetotransport in Quantum Point Contacts InAs/AlSb* Supervisors: Prof. dr. Ing. F. Beltram
2003-2005	M.Sc. degree in Materials Engineering *cum laude*, Catholic University of Leuven, Belgium Subject: *Interaction between colloids at electrolyte-electrolyte interface* Supervisors: Prof. dr. J. Fransaer
2003-2007	Ph.D. research at the Kavli Institute of Nanoscience, Delft University of Technology, The Netherlands Subject: *Crossed Andreev reflection and electron transport in ferromagnetic hybrid structures* Promotor: Prof. Dr. ir. T. M. Klapwijk Co-promotor: Dr. A. F. Morpurgo

List of publications

1. *Adiabatic quantum pumping at the Josephson frequency*
   S. Russo, J. Tobiska, T. M. Klapwijk and A. F. Morpurgo (Submitted to Physical Review Letters, see also: cond-mat/07042590).

2. *Bias-dependent Contact Resistance in Rubrene Single-Crystal Field-Effect Transistors*
   A. Molinari, I. Gutierrez, I. N. Hulea, S. Russo and A. F. Morpurgo (To appear in Applied Physics Letters, see also: cond-mat/0703029).

3. *Correlation effects in the density of states of annealed Ga1-xMnxAs*
   S. Russo, T. M. Klapwijk, W. Schoch and W. Limmer, Physical Review B **75**, 033308 (2007).

4. *Reproducible low contact resistance in rubrene single-crystal field-effect transistors with nickel electrodes*
   I. N. Hulea, S. Russo, A. Molinari and A. F. Morpurgo, Applied Physics Letters **88**, 113512 (2006).

5. *Observation of Non-local Andreev reflection in Normal metal/Superconductor structures*
   S. Russo, M. Kroug, T. M. Klapwijk and A. F. Morpurgo, AIP Conference Proceedings **850**, 877 (2006).

6. *Magnetotransport through a single Ferromagnetic domain of (Ga,Mn)As*
   S. Russo, S. T. B. Goennenwein, A. F. Morpurgo, T. M. Klapwijk, W. Van Roy and J. De Boeck, AIP Conference Proceedings **850**, 1275 (2006)

7. *Experimental observation of non-local bias dependent Andreev reflection*
   S. Russo, M. Kroug, T. M. Klapwijk and A. F. Morpurgo, Physical Review Letters **95**, 027002 (2005).

8. *Quantitative study of magnetotransport through a single (Ga,Mn)As ferromagnetic domain*
   S. T. B. Goennenwein, S. Russo, A. F. Morpurgo, T. M. Klapwijk, W. Van Roy and J. De Boeck, Physical Review B **71**, 193306 (2005).

Acknowledgements

The research presented in this PhD thesis would not have been possible without the contribution of several people with whom I have been working or collaborating during the last four years of my scientific research. It is my pleasure to take this opportunity to thank all the people who were directly or indirectly involved and supported me in my work.

First of all I would like to thank my promotor Prof. Teun Klapwijk. You are a very special person for me. Many Professors excuse their lack of contact with their students with the fact that they are busy persons. I know that you certainly are a busy person, but I very much appreciate that you could always find a spot to meet and have a discussion. I thank you sincerely also for having the sensibility to stimulate the personal scientific initiative, which in practice translates into a certain degree of freedom to work on my own ideas. Our interaction was definitively very constructive also for what concerns my personal character. Indeed, you have been shaping my juvenile temper, and on this regard I thank you for teaching me how to handle with calm difficult situations.

My deep gratitude goes also to my supervisor Alberto Morpurgo. I really admire your determination in science which is like an adrenaline injection for all of us working with you. Many many thanks for the patience in teaching me the measurements techniques. I appreciated very much the various stimulus you gave me in several occasions and the several interesting scientific and non scientific discussions, which often sounded like fights for the others, but... we are both italians and for us an emotionless dialog is not a real dialog. I really enjoyed the evenings spend together eating pizza and chatting about physics, I found them very instructive and inspiring. Alberto, lasciamelo dire in Italiano che suona meglio, ho tanta stima di te e ti auguro un futuro brillante. Grazie di tutto.

Especially I would like to thank Prof. Dr. Yuli V. Nazarov and Prof. Dr. Gerrit E. W. Bauer for useful discussions. Thanks to Dr. Miriam Blaauboer for the sincere interest in my results on adiabatic pumping.

I would like to thank my best friends, which almost all of them belonged to

the theory group in Delft. Many thanks for nice scientific chats go to Oleg... who is a pure source of energy, enough to lighten an entire city, concentrated into a tiny human body! We really had nice time together. You even made me skate on ice, what an experience. Then Jens, the most quiet and mild guy of the theory group. We shared several passions from physics to photography and birdwatching. Those photo-dinner to your place are something that I will always carry with me. Dear Jens, our constructive exchange led also to one chapter of this thesis. Thanks for all the physics discussions late in the night, it is a pleasure to work with you. Then Wouter, always very patient to drink a thee with me and chat about my various concerns on how to proceed in research projects. *Dulcis in fundo* Antonio. Together we spent really a lot of time chatting about physics. You really made me wonder how different can be the approach to science for a theorist and an experimentalist. Many thanks go to: Omar the restless word-generator, Xuhui who despite the scratch I did on his rented track is always very friendly with me, Henry for the biking tours, Gabriele for the very good Italian coffee, Anna, Sijmen, Fabian and Jeroen.

I'm also very grateful to Paul, my college and friend. You tried in all the ways to let me appreciate all various different aspects of the Dutch mentality and society, in return you accepted to get to know the Italian attitude to life. One thing I still regrate: I could not teach you that the use of a knife on the table is only to cut meet and bread but not spaghetti! Thanks also very much for all the outdoor excursions, in particular the one to Oostvaardersplassen together with your father. By the way... who will ever forget how good is the honey that your father produces! Thanks also to Anne for the wonderful dinners we had together, and for the warm thee she provided when biking into freezing weather all together!

A very special thank goes to Monica. You have been constantly stimulating me all over the PhD with continuous discussions. You are really a precious college and friend. Your motivation and attitude at work has been an example for me. In particular I had really a lot of fun attending the master in Material engineering in Belgium with you. In all these years we had many good occasions to test our determination and sincere thirst for knowledge. Thanks.

I like to thank Iulian Hulea for catching my stimulus to work together on organic single crystals. Our curiosity developed into several promising projects. I'm also deeply indebted to Sebastian. You showed me how should a scientist focus his efforts in the lab in other to finalize his research for a publication. I would like to thank also Matthias Kroug for the help in the clean room. I really appreciated the cooperation with you. How can I forget my officemates Ruurd and Denis? Thanks Denis for being always very patient during all the phone calls

I had with Jens in Japan while working on adiabatic pumping, and thanks Ruurd for introducing me to Mickey Mouse. A very special thank goes also to Gao. I know that meeting the Italian culture it was a shock for you. Such a rude culture compared to Chinese, after all I hope you enjoyed it a little bit... at least you are now plenty of anecdotes for the family! Further, my work could not be possible without the perfect synergy between PhD students and technicians of our group. Thus my gratitude goes to all of them: Tony, Niels, Ron, Ben and Jan. And... what about the secretaries? Oh boy, very special and precious part of our group, hartelijk bedankt Maria Roodenburg-van Dijk and Monique Vernhout.

I would like to thank all the people which directly or indirectly had something to do with my formation period in Delft: Chris Lodewijk, Rami Bari (the voice noise generator!), Gabri Lansbergen (Blondy thanks for all the thee cups we had together late in the night in the department), Herman Selier, Hon Tin Man, Frank Meyer (the incredibly nice human soul), Ruth de Boer, Diedrick Rep, Sven Rogge, Jaap Caro, Add Verbrugge, Merlijn Hajenius (thanks for helping me in rescuing Monica in DIMES that famous night), Edgar, Benoit, Jeroen, Hangxing, Tarun, Nathan and Nacho.

Big part of my research was entirely relying on the clean room facility of DIMES. Thus many sincere thanks go to all the technicians of the Nanofacility. They are really wonderful people, always ready to help and find a solution to your problems: Emil van der Drift, Roel Mattern, Anja van Langen and Arnold van Run. I'm particularly grateful to Marc Zuidam (for me Marco Polo) and Marco Borsato (alias Marco van der Krogt, code name Marcolino) for their assistance in the clean room in various moments. Thanks Marco Borsato and Anda for all the evenings spent together. I'm still regrating that we did not succeed to let Anda appreciate the beauty of bird watching and bird photography.

Now I will switch to Italian to thank the person who made me fall in love with physics, my secondary school Professor of Physics. Si caro Prof. LoNigro siete proprio voi. Qui nel testo venite dopo tutta la lunga lista degli accademici, ma in realtá il primo e piú sincero ringraziamento é rivolto a voi. Grazie al vostro entusiasmo e alla vostra creativitá nell'insegnare la fisica siete riuscito a stuzzicare la mia fantasia e a farmi innamorare della fisica. Insegnanti come voi costituiscono la ricchezza delle scuole Italiane, ed io sono stato fortunato ad essere stato vostro alunno. Grazie di tutto.

A questo punto voglio ringraziare la mia famiglia. Cosa sarei senza di voi? La gioia di vivere e di amare dei miei genitori é la polvere magica che molti scrittori hanno descritto nelle fiabe per bambini. Grazie non solo per il supporto morale in questi anni di PhD, ma soprattutto per l'educazione che mi avete dato. Grazie anche alle mie sorelle e a Savino mio fratello, tre persone semplici ma di

grandissima ricchezza interiore. Questo successo lo devo certamente anche a voi.

Finally, it is nearly impossible to remember all the people who helped me to accomplish this result, and I apologize to anyone that I have unintentionally overlooked. Thank you all.

Saverio Russo

Delft, 5 May 2007

Casimir PhD Series 2007-06
ISBN 978-90-8593-030-3